

QUANTITATIVE NO MEASUREMENTS IN A DIESEL ENGINE

Quantitative NO measurements in a diesel engine

Kasper Verbiezen

Thesis Radboud University Nijmegen — Illustrated

With references — With summary in Dutch

ISBN-10 90-9021435-6

ISBN-13 978-90-9021435-1

NUR 926

Subject headings: combustion diagnostics / diesel engine / nitric oxide / laser spectroscopy
/ imaging

Copyright © Kasper Verbiezen (2006).

QUANTITATIVE NO MEASUREMENTS IN A DIESEL ENGINE

EEN WETENSCHAPPELIJKE PROEVE OP HET GEBIED VAN DE
NATUURWETENSCHAPPEN, WISKUNDE EN INFORMATICA

PROEFSCHRIFT

TER VERKRIJGING VAN DE GRAAD VAN DOCTOR
AAN DE RADBOUD UNIVERSITEIT NIJMEGEN,
OP GEZAG VAN DE RECTOR MAGNIFICUS PROF. DR. C.W.P.M.BLOM,
VOLGENS BESLUIT VAN HET COLLEGE VAN DECANEN
IN HET OPENBAAR TE VERDEDIGEN
OP DONDERDAG 8 FEBRUARI 2007,
OM 10.30 UUR PRECIES

DOOR

KASPER VERBIEZEN

GEBOREN OP 13 MAART 1978
TE NIJMEGEN

PROMOTORES : PROF. DR. J.J. TER MEULEN

PROF. DR. W.L. MEERTS

COPROMOTOR : DR. N.J. DAM

MANUSCRIPTCOMMISSIE : DR. F.J.M. HARREN

PROF. DR. R.S.G. BAERT
TECHNISCHE UNIVERSITEIT EINDHOVEN

PROF. DR. C. SCHULZ
UNIVERSITÄT DUISBURG-ESSEN, DUITSLAND



Radboud University Nijmegen



This research was financially supported by the Dutch Technology Foundation STW (project EWE.5125).

Table of contents

1	Introduction	1
1.1	Motivation	1
1.2	A brief introduction to diesel engines	4
1.3	A brief introduction to laser spectroscopy in combustion engines	15
1.4	Outline of this thesis	19
2	The research engine	21
2.1	Introduction	21
2.2	Optical access	21
2.3	Engine characteristics	25
2.4	The common-rail fuel injection system	27
2.5	Exhaust NO concentration measurements	38
3	NO LIF in more detail	41
3.1	Introduction	41
3.2	Processes involved and their p,T dependence	43
3.3	NO LIF excitation-detection schemes	47
3.4	Calibration	53
4	Absorption of NO LIF by hot O₂ and CO₂	55
4.1	Introduction	55
4.2	O ₂ absorption spectra	55
4.3	Experiment	57
4.4	Results and discussion	59
5	Attenuation corrections for in-cylinder NO LIF measurements	61
5.1	Introduction	62

TABLE OF CONTENTS

5.2	Laser diagnostics	63
5.3	Experiment	68
5.4	Results and discussion	71
5.5	Discussion: complete attenuation correction requires combination of techniques	80
5.6	Discussion: comparison of excitation-detection schemes for NO LIF	82
5.7	Summary and conclusions	85
6	Quantitative NO-LIF measurements in a heavy-duty diesel engine	89
6.1	Introduction	90
6.2	NO LIF signal dependence	90
6.3	Experiment	91
6.4	Data processing	94
6.5	Results and discussion	100
6.6	Conclusions	103
7	In-cylinder NO concentrations in relation to injection timing	105
7.1	Introduction	106
7.2	Experiment	107
7.3	Results and discussion	115
7.4	Summary and conclusions	124
8	Summary and outlook	129
8.1	Summary	129
8.2	Outlook	131
	References	136
	Samenvatting	151
	Dankwoord	155
	Curriculum vitae	159
	Publications	161

Chapter 1

Introduction

1.1 Motivation

A large fraction of global traffic is powered by diesel engines. Economic and powerful power sources, diesel engines are especially used in heavy-duty transportation, such as trucks, trains, and ships. Additionally, diesel-powered passenger cars have become increasingly popular in recent years, and even diesel sports cars emerge on the market. In fact, Audi were the worlds first car manufacturer to compete in (and win!) the 24 Heures du Mans with a diesel-engined sports car in 2006.

Due to their better fuel economy, diesel-powered cars usually generate less CO₂ (carbon dioxide) per unit power than vehicles running on gasoline. Unfortunately, diesel engines produce higher levels of soot and oxides of nitrogen (NO_x, consisting of nitric oxide, NO, and nitrogen dioxide, NO₂). Soot particles (especially the smaller ones) are dangerous to human health as they may penetrate deeply into the lungs. They are believed to be carcinogenic, especially when aromatic fuel compounds are adsorbed onto their surface. In the atmosphere, NO oxidises to form NO₂, which in turn may react into nitric acid (HNO₃). Together with SO₂ emissions, nitric acid is a major contributor to acid rain, causing damage to ecosystems and soil. Additionally, high NO₂ concentrations in cities may lead to smog formation. Figure 1.1 shows that the southern part of the Netherlands is one of the regions with the highest tropospheric NO₂ density of Europe (together with the Po region in Italy and some major cities). Other major sources of NO₂ can be found along the east coast of the United States, in China, and in South Africa.

Road traffic, and especially diesel-powered transportation, is a major source of

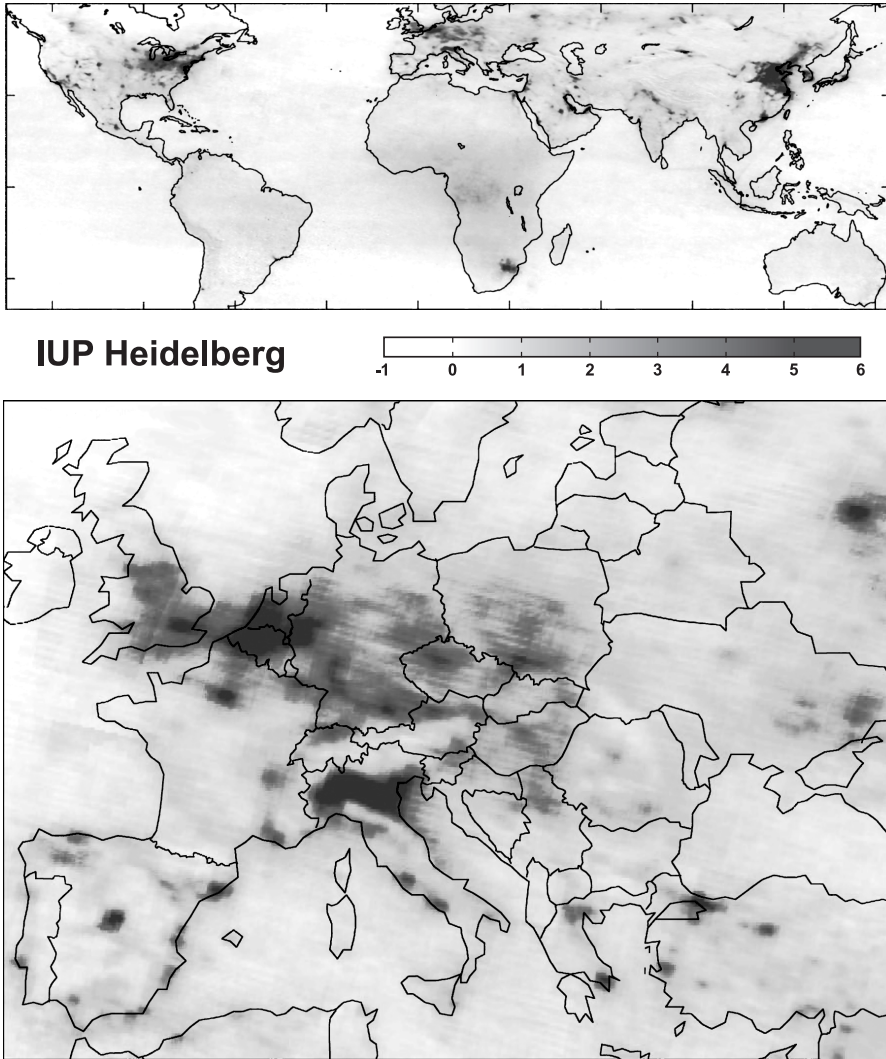


Figure 1.1: Global (top) and European (bottom) vertical column density of NO₂ in the earth's troposphere. Values are in 10¹⁵ molecules/cm², and represent the average over the period January 2003 – June 2004. The measurements were performed by the SCIAMACHY instrument (SCanning Imaging Absorption spectrometer for Atmospheric Cartography) on board of ENVISAT (the European ENVIRONMENTAL research SATellite). Images adapted from Beirle,¹ with permission. Daily NO₂ densities in the Netherlands can also be found on the KNMI website (www.knmi.nl/omi/publ-nl/nieuws/index.html), based on measurements by another satellite-based instrument, called OMI (Ozone Monitoring Instrument).

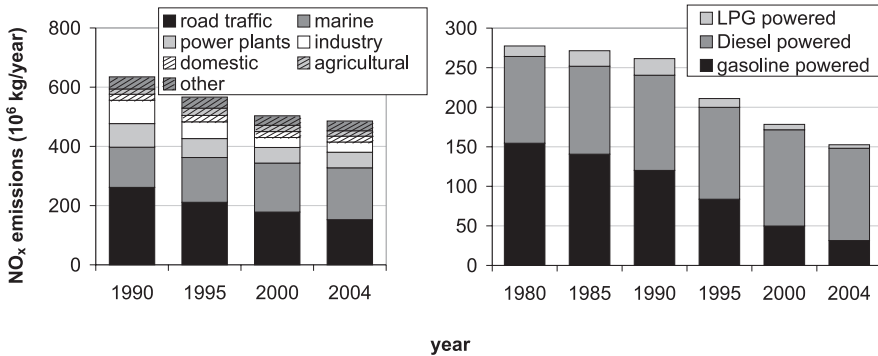


Figure 1.2: Yearly NO_x production in the Netherlands. Left: total NO_x emissions; right: road traffic emissions. Source: Centraal Bureau voor Statistiek (CBS), NL.

NO_x. Figure 1.2 shows that road traffic contributes for roughly one third to the yearly produced NO_x in the Netherlands. It also shows that the fraction due to diesel engines is still increasing. This is not only the case in the Netherlands.

Worldwide, legislation on pollutant emissions is becoming increasingly stringent in order to constrain NO_x emissions. This includes the automotive industry, pushing car manufacturers and engine designers to the limits of the present technology. The demand for cleaner engines invokes extensive research, focussing on both catalytic exhaust gas after-treatment and optimisation of the combustion itself. The latter requires a thorough understanding of the underlying processes, and research focusses on the development of numerical models that can handle both complex chemistry and fluid dynamics. Such models are indispensable tools for the efficient assessment of new engine designs or even new combustion concepts. Additionally, much effort is put into the development of experimental techniques for validation of these models, by quantitative determination of important combustion parameters (e.g. species concentrations, temperature, size of fuel droplets and particulate matter). Laser-based techniques have often proven extremely useful in combustion diagnostics for their high temporal and spatial resolution, and species selectivity, and most importantly because of their minimal intrusion in the combustion process.

The work presented here aims at the development of laser diagnostic techniques for quantitative, in-cylinder concentration measurements of nitric oxide in a heavy-duty diesel engine. Although the laser-induced fluorescence technique is popular for NO visualisation in both diesel engines²⁻⁸ and gasoline engines,⁹⁻¹⁵ the strong attenuation of both the laser beam and the fluorescence during their traversal of the combustion chamber is often not properly corrected for. Through the develop-

ment of additional (laser) techniques, a detailed analysis of all attenuation effects is now possible, allowing for the first time fully corrected NO LIF measurements in a heavy-duty diesel engine. This thesis will be further outlined in Section 1.4. First, the reader will be introduced to internal combustion engines (Section 1.2) and to spectroscopic techniques popular in engine research (Section 1.3).

1.2 A brief introduction to diesel engines

The development of internal combustion engines traces back to 1876, when Nicolaus Otto proposed an engine cycle consisting of four piston strokes. This idea forms the basis of today's gasoline engine (also known as Otto, petrol, or spark-ignition (SI) engine). In the four strokes of an Otto engine, a fresh air-fuel mixture is led into the cylinder during the intake stroke, and compressed (compression stroke). During the power, or expansion, stroke, the mixture is ignited by a spark, and the expanding hot combustion gases perform mechanical work on the piston. Finally, the combustion products are pushed out of the cylinder during the exhaust stroke.

The work delivered to the piston, and thus the (thermal) efficiency, increases with increasing compression (or expansion) ratio ϵ (i.e. the ratio of the maximum to the minimum cylinder volume). In Otto engines the compression ratio is limited by "knock": auto-ignition of the fuel-air mixture caused by too high pressure and/or temperature prior to the spark. This effect does not only decrease the efficiency but it may also damage the engine. The limitation in compression ratio was successfully addressed by Rudolf Diesel, by (1) using heavier fuels with longer ignition delays than gasoline, and (2) injecting the fuel directly into the combustion chamber, allowing control of the moment of auto-ignition by adjusting the injection timing. Because the fuel-air mixture auto-ignites due to the high pressure and temperature that are reached at the end of the compression stroke, diesel engines are also known as compression-ignition (CI) engines. Due to their higher compression ratios, diesel engines are thermodynamically more efficient than Otto engines. A schematic representation of a four-stroke diesel engine cycle is presented in Fig. 1.3.

The two extreme positions of the piston are indicated in Fig. 1.3 as TDC (Top-Dead-Centre) and BDC (Bottom-Dead-Centre); the positions in between are usually expressed in terms of the corresponding angle of the crank shaft, i.e. in crank angle degrees ($^{\circ}$ CA). One full rotation of the crankshaft thus corresponds to 360° CA. It is common practice to choose the origin at TDC prior to the power stroke, so that crank angles are expressed in $^{\circ}$ aTDC (after TDC).

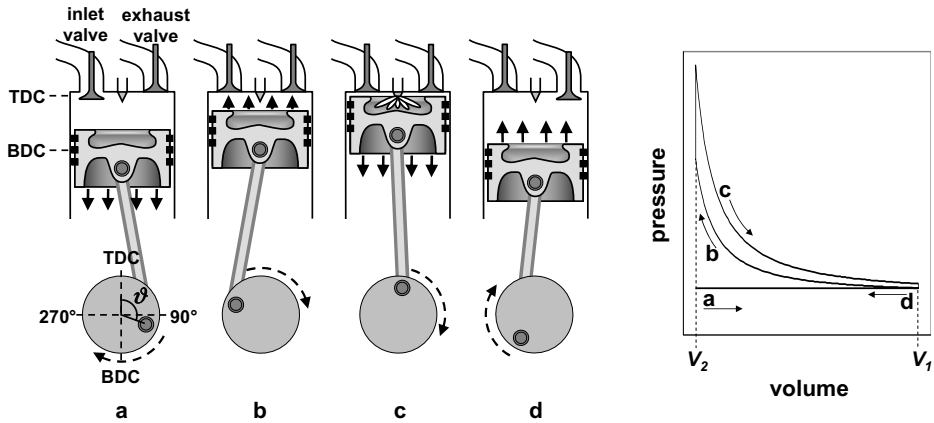


Figure 1.3: Schematic representation of a four-stroke engine (left) and the corresponding p-V diagram (right). (a) inlet stroke; (b) compression stroke; (c) combustion stroke; (d) exhaust stroke. In the p-V diagram, the combustion is approximated to take place at constant volume V_2 , and the compression and expansion strokes are assumed adiabatic. For this simplified example, the efficiency can be shown to be $\eta = 1 - \varepsilon^{1-\gamma}$, with $\varepsilon = V_1/V_2$ and $\gamma = c_p/c_v$ the ratio of the specific heats.

1.2.1 A conceptual model of diesel combustion

Diesel combustion is a complex process; the fuel already consisting of hundreds of hydrocarbon species, it leads to even more chemical reactions that are strongly influenced by the degree of fuel-air mixing (and thus the breakup behaviour of the liquid fuel spray) and the turbulent environment during combustion. Diesel spray development has been, and still is, extensively studied^{16–19} both in reactive (air) and in non-reactive (N_2) environments, and both in high-pressure, high-temperature cells and in optical engines. As a result, diesel spray characteristics such as jet penetration and vaporisation are now reasonably well understood for a wide range of fuel injection pressures, injector nozzle diameters, and ambient air conditions.

Dec and coworkers conducted many optical and laser-based diagnostics in a heavy-duty diesel engine, focussing on natural flame luminosity measurements for spray visualisation^{20,21} and autoignition imaging,^{22,23} soot measurements by means of laser-induced incandescence (LII)^{20–22,24} and laser light scattering,^{20–22} fuel vapour imaging using Rayleigh scattering,²⁵ OH radical imaging by laser-induced fluorescence (LIF),²⁶ and NO imaging using LIF,⁴ using both regular diesel and a low-sooting variant (to minimise obscuration) as fuel.

All these studies were performed in the same research engine, and were combined

with engine characteristics such as fuel injection timing, cylinder pressure, and heat release rate to formulate a conceptual model of diesel spray combustion.²⁷ The model of Dec is the first to describe diesel combustion as a two-stage process, consisting of a fuel-rich premixed flame during which all the fuel first undergoes partial oxidation, and a diffusion flame (or mixing-controlled flame) during which the remaining products are burnt. This picture is in contrast to the “classical” view of a pure fuel-air diffusion flame.^{28,29} Two years later, Flynn et al. extended Dec’s conceptual model,³⁰ combining it with a chemical kinetic modelling study of n-heptane combustion and empirical validation.

The two-stage character of diesel combustion can be nicely illustrated by the heat release rate (i.e. the rate at which the chemical energy of the fuel is released by the combustion process). The heat release rate, $dQ/d\vartheta$ can be calculated from the cylinder pressure trace assuming ideal gas behaviour and adiabatic compression and expansion:²⁹

$$\frac{dQ}{d\vartheta} = \frac{\gamma}{\gamma - 1} p \frac{dV}{d\vartheta} + \frac{1}{\gamma - 1} V \frac{dp}{d\vartheta}, \quad (1.1)$$

with p and V the cylinder pressure and volume, respectively. Figure 1.4 shows a cylinder pressure curve that is typical for a direct-injection diesel engine, as well as the corresponding heat release rate. Dec’s conceptual model²⁷ is summarised below, supplemented with calculations from Flynn et al..³⁰ Fig. 1.5 shows a schematic representation of a reacting diesel spray at about 5° aSol*.

0.0 – 4.5° aSol As liquid diesel fuel is injected into the combustion chamber, the spray breaks up and entrains some of the surrounding hot air (approximately 800–900 K). As a consequence, the fuel temperature rises and some of the fuel evaporates. The heat that is extracted from the air by fuel evaporation is reflected in the negative heat release rate at this stage (Fig. 1.4). For the engine under study, the fuel spray was completely evaporated after 20–25 mm from the injector. Due to the mixing with the entrained air, a rich fuel-air mixture (equivalence ratio[†] $\Phi \approx 2-4$) forms a sheath around the sides and leading edge of the fuel jet.

3.0 – 5.0° aSol The jet reaches a temperature of about 750 K, and auto-ignition takes place throughout the premixed, fuel-rich zone. In this zone, the larger fuel

*aSol = after start of injection. At 1200 rpm, 1° CA corresponds to 139 μ s.

[†]The equivalence ratio is the ratio of the actual fuel-air ratio to the fuel-air ratio when just enough oxygen is available to fully oxidise all fuel. The latter conditions are also referred to as stoichiometric. Thus, if $\Phi > 1$, combustion is fuel-rich, whereas with $\Phi = 1$ it is stoichiometric.

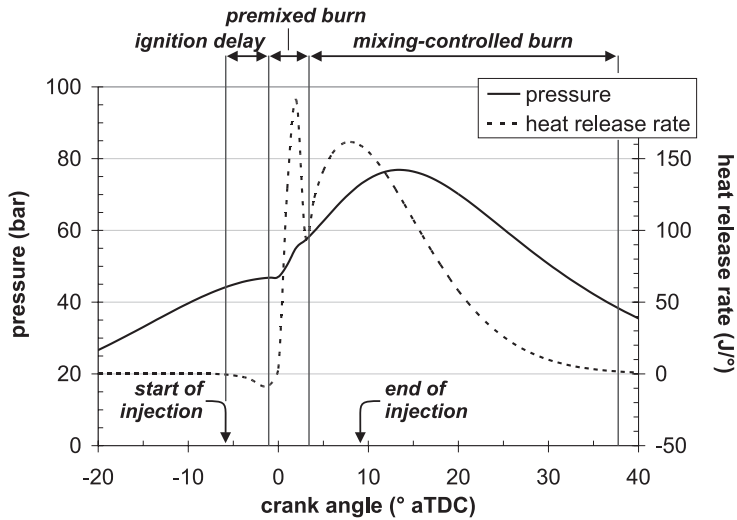


Figure 1.4: Typical cylinder pressure (solid line) and heat release rate (dashed line). Indicated are the start and end of fuel injection, the ignition delay, and the premixed and mixing-controlled burn phases.

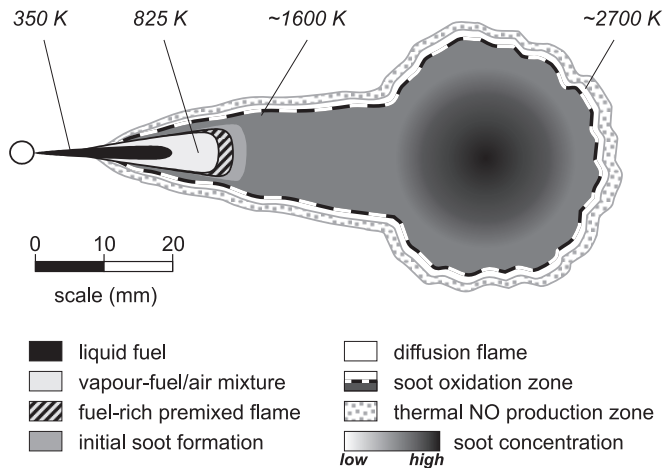


Figure 1.5: Schematic representation of the conceptual model by Dec,²⁷ extended with temperature data from Flynn et al..³⁰ The (single-hole) fuel injector is represented by a circle on the left. Reprinted with permission from SAE 970873 © 1997 SAE International.

compounds are broken into fragments like C_2H_2 , C_2H_4 , and C_3H_3 , and products such as CO , CO_2 , and H_2O . These small fuel fragments are known to form soot precursors such as polycyclic aromatic hydrocarbons (PAHs). Along with further entrainment of hot air, these oxidation reactions increase the temperature of the inside of the jet to over 800 K.

4.0 – 9.0° aSol The initially premixed fuel burns rapidly, giving rise to a short-lived, intense spike in the heat release rate (Fig. 1.4). The start of combustion is usually defined as the point when the heat release curve starts to increase. As long as fuel is injected, the rich fuel-air mixture continues to form around the fuel spray tip (although in lower quantities than the initial premixed burn), resulting in a standing premixed flame. By 5.0° aSol, large PAHs are observed in this area and the temperature is further raised to 1600-1700 K. The first soot particles have been observed at 6.0° aSol. There is no sign of NO in the premixed combustion.

~6° aSol Since the fuel-rich premixed flame does not contain sufficient oxygen to fully combust all the fuel, a diffusion flame forms around the cloud of partial oxidation products. Due to the heat from this flame, the liquid part of the fuel spray decreases by a few millimetres (2–3 mm according to Dec). The diffusion flame is a thin reaction layer, where the remaining (partially oxidised) fuel is converted into CO_2 and H_2O vapour and where the temperature is raised above 2500 K. At the inner part of the diffusion flame relatively small soot particles, formed in the premixed flame, can be found a couple of centimetres (27 mm) downstream from the injector and beyond. The soot concentration and particle size increases down the jet. At around 8.0° aSol, a head vortex forms at the leading edge of the jet, containing even larger soot particles. Soot oxidation takes place in the diffusion flame, being the only place where OH radicals (the main agents for soot destruction) are present in high concentrations. Oxidation by oxygen attack is another possible mechanism, and would also occur at the outer layer of the diffusion flame only, as the regions inside the flame contain no oxygen.

According to Dec, and Flynn et al., the temperatures and oxygen concentrations in the premixed flame are too low for thermal NO formation*, whereas equivalence ratios ($\Phi \approx 2-4$) are too high for the prompt mechanism. Instead, NO is expected to be formed at the outer, lean sides of the diffusion flame, in regions with sufficient oxygen at high enough temperatures for (thermal) NO formation. This was

*The "thermal" and "prompt" NO formation mechanisms will be discussed in Section 1.2.2.

confirmed by later NO LIF experiments by Dec and Canaan,⁴ showing the first detectable NO in the diffusion flame sheath.

9.0° aSol to end of injection After the end of the premixed burn spike, the combustion is primarily mixing-controlled. This mixing-controlled phase is visible as the second peak in the heat release rate in Fig. 1.4. This peak is broader than the premixed spike because the combustion speed is now limited by turbulent mixing rather than chemistry. The jet continues to grow, but without any other apparent changes in shape. Both the soot concentration and the particle size increase until the end of injection.

Dec's conceptual model does not describe the processes that take place after the end of combustion. According to Flynn et al.,³⁰ the diffusion flame may oxidise all soot particles it encounters. If this is the case, it is the quenching of this diffusion flame that causes soot emissions. Since thermal NO formation is a relatively slow process, the major part of NO formation is expected to take place in the later part of the mixing-controlled burn and even in the hot post-combustion gases. The lower temperatures are compensated by the longer time available for reaction and by the larger gas volumes that are involved. NO LIF measurements by Dec and Canaan showed that, in their engine, NO formation continues after the end of combustion, contributing for an estimated 33% to the total (engine-out) NO.⁴ In practice, post combustion NO formation might vary from engine to engine, being strongly influenced by the cooling rate of the combustion gases as they mix with cold residual air, and by the cooling rate due to the expansion of the cylinder volume.

1.2.2 Formation of nitric oxide

Thus far, four different mechanisms have been proposed for the formation of nitric oxide,³¹ including the direct oxidation of nitrogen (i.e. thermal NO), nitrogen oxidation via hydrocarbon radicals (i.e. prompt NO), the formation of nitric oxide via nitrous oxide, and oxidation of fuel-bound nitrogen.

Thermal NO formation The thermal mechanism for NO formation was proposed by Y.B. Zeldovich in 1946,³² and later extended by Lavoie et al.,³³ who added the third reaction. This mechanism is also known as the extended Zeldovich mechanism, and is the best known reaction pathway of NO formation. It is given by the three

reactions:



Reaction 1.2 has a relatively high activation energy (318 kJ/mol), and as a consequence this mechanism becomes significant only at higher temperatures ($T > 1800$ K, hence the name “thermal mechanism”). Furthermore, the thermal mechanism requires equivalence ratios close to stoichiometric ($0.8 \leq \Phi \leq 1.0$). Still, this mechanism is believed to be the major NO_x source in internal combustion engines, most NO being formed in the diffusion flame and in the post-flame regions.

Prompt NO formation In contrast to the thermal mechanism, prompt NO formation mechanism (also called Fennimore mechanism after C.P. Fennimore³⁴) occurs in fuel-rich flames (more precisely, $0.9 \leq \Phi \leq 1.8$). The name “prompt” originates from the fact that NO is formed so rapidly that it appears in or near the flame front. Although the exact reactions underlying this mechanism are not yet fully known, the process involves a hydrocarbon radical (presumably CH) that reacts with N_2 to form hydrocyanic acid (HCN):



Via many steps the HCN is oxidised into N atoms, subsequently reacting into NO by reactions such as 1.3 or 1.4. In a recent study, Moskaleva and Lin³⁵ demonstrated that the reaction in Eq. 1.5 is in fact spin-forbidden, and that the reaction $CH + N_2 \rightleftharpoons NCN + H$ is more likely to occur. In that case, prompt NO is formed through oxidation of NCN by O, O_2 , or OH.

NO formation via N_2O This mechanism was postulated by Wolfrum in 1972.³⁶ If a third molecule M is present, O and N_2 may react into nitrous oxide, N_2O (in contrast to reaction 1.2), which subsequently yields NO after oxygen atom attack:



As this mechanism has a relatively low activation energy (76 kJ/mol), and as it is based on a three-body reaction, it may become important at relatively low temperatures and high pressures. Therefore, the N_2O mechanism is usually negligible,

except for lean, low-temperature combustion, when the prompt and thermal NO formation mechanisms become less significant.

NO formation from fuel-bound nitrogen This formation mechanism is an important contributor for fossil fuels with a relatively high nitrogen content, such as coal (0.5–2% by mass). Nitrogen is typically bound in aromatic ring structures, but these are converted into smaller fragments by thermal decomposition prior to combustion. These fragments include a.o. NH_3 , NH_2 , NH , HCN , and CN , and they are usually rapidly oxidised to NO through various reactions. This mechanism is most efficient for lean and stoichiometric combustion, and is only weakly dependent on temperature.

Reaction of NO into NO_2 As was already mentioned in Section 1.1, the engine-out NO reacts into NO_2 :



Since the forward reaction is exothermic, the equilibrium shifts to the left at high (combustion) temperatures; however, as the exhaust gases cool down, all NO is converted into NO_2 . Since NO is meta-stable, this conversion is a relatively slow process. Based on the values reported by Tsukuhara et al.,³⁷ and taking a typical exhaust temperature of 473 K and an initial NO concentration of 500 ppm, 50% of the NO has reacted into NO_2 in 35 minutes. At room temperature, the half-time is just below seven minutes. Note that the reaction speed is also linearly proportional to the NO concentration.

1.2.3 Controlling pollutant emissions

Pollutants (mainly NO_x and soot) emanating from diesel engines can be reduced by a number of techniques, that can be subdivided in two categories: modification of the combustion process and aftertreatment. Of course, combinations may even further reduce emission levels. Although modification of the combustion process can be very effective, the reduction of NO_x generally leads to higher soot emissions and vice versa. The reason for this is that *oxidation* of soot and (thermal) *formation* of NO both increase with increasing temperature. This trade-off between soot oxidation and NO_x formation is a common challenge in engine design. It is depicted in Fig. 1.6. A number of emission reduction strategies are listed below.

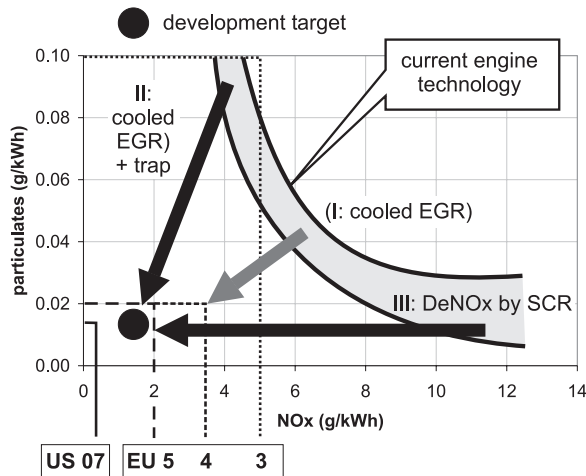


Figure 1.6: The tradeoff between emissions of soot particulates and NO_x , indicated by the grey area. The arrows indicate the various strategies to push the trade-off curve further towards the origin (the current development target, Euro V, is due for 2008). The European and US emission legislation are also indicated by dashed, dotted, and solid lines. Reprinted with permission from SAE 2001-01-0186 © 2001 SAE International.

Modifying the combustion process

Exhaust gas recirculation Effective NO_x reductions (up to 50% or more^{29,38,39}) can be realised with exhaust gas recirculation (EGR), without a significant sacrifice in fuel economy. With EGR, a fraction (5–30%) of the exhaust gases is recirculated back into the cylinders, resulting in lower flame temperatures (despite the recirculated hot exhaust gases): as EGR dilutes the fresh intake air with gases like N_2 , CO_2 , and H_2O , the resulting lower air-fuel ratio slows down the combustion, leading to lower temperatures and thus less thermal NO_x formation. Furthermore, combustion temperatures are additionally decreased by the higher heat capacity of the cylinder charge (especially CO_2 and H_2O). Although EGR reduces the soot formation rate, it unfortunately also decreases soot oxidation. Yet, the *net* soot production as a function of EGR rate does not seem to follow a clear trend, as both increased^{29,39} and decreased³⁸ engine-out soot levels have been observed. EGR can also be achieved by earlier closing of the exhaust valve, thus keeping some of the exhaust gas in the cylinder (“internal EGR”). With external EGR, however, higher EGR rates can be realised by cooling the recirculated exhaust gas before it is led back to the air intake manifold (“cooled EGR”).

Homogeneous charge compression ignition (HCCI) HCCI, or premixed charge compression ignition (PCCI), is a relatively new combustion concept that combines the benefits from gasoline and diesel engines. A key feature is the preparation of a homogeneous, lean fuel-air mixture (like in a gasoline engine) that auto-ignites (like in a diesel engine). Due to the homogeneity, auto-ignition can (at least in principle) occur at many locations, and the fuel combusts in a uniform manner. A homogeneous fuel-air mixture (i.e. charge) is created by injecting the fuel very early, guaranteeing a long time for efficient mixing before the start of combustion. In order to avoid too early autoignition, the relatively high compression ratio typical for diesel engines has to be lowered to allow operation in HCCI mode. Alternatively, the mixture can be diluted with exhaust gas recirculation, which also decreases the burning rates. Without EGR, the homogeneous mixture would burn all at once, which can lead to excessive noise and even damage.

In a diesel engine, soot is formed due to the presence of fuel rich regions, whereas NO is formed in stoichiometric, high-temperature regions. With HCCI, the entire combustion volume is fuel-lean (due to the premixing) and at relatively low temperature (due to dilution and to the lower compression ratio), and consequently the formation of both NO_x and soot is potentially reduced.

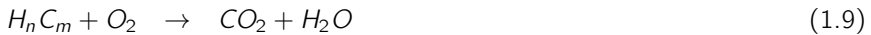
Due to its lean character, HCCI is limited to low engine loads. This implies that a practical HCCI engine should be able to switch from HCCI to "normal" operation. It also limits the applicability of HCCI for heavy-duty engines. Another drawback of HCCI is that small non-uniformities in the mixture fraction could lead to inhomogeneous combustion: slightly too rich regions cause to rapid combustion, similar to knock, whereas too lean regions may lead to incomplete combustion, or no combustion at all. The latter is reflected in the relatively high emission of unburned hydrocarbons and carbon monoxide (CO), and a slightly reduced fuel economy as compared to regular diesel engines.

Injection rate shaping With the current electronically controlled (common-rail) fuel injection systems it is possible to arrange multiple (short) injections per cycle. By optimising the fuel injection rate, both soot and NO_x emission can be reduced simultaneously.⁴⁰ By lowering the combustion rate, peak temperatures and thus NO_x formation are reduced. Besides, split injections have the advantage of improving fuel-air mixing and soot oxidation rates. Although exact numbers strongly vary with engine load and injection timing, simultaneous reduction in soot (50%) and NO_x (30%) have been observed in a heavy-duty engine for triple injections at 25% load.⁴⁰ Injection rate shaping has been combined with EGR for even further reduction.^{41,42}

Low-sooting fuels Soot emissions can be greatly reduced when using alternative fuels, especially those with oxygen enrichment. These fuels can be used “pure” or in a blend with regular diesel. In general, NO_x emissions are either not affected or slightly reduced. Typical oxygenated fuels such as methylal (CH₃-O-CH₂-O-CH₃, also known as dimethoxymethane, DMM),^{43,44} butylal (C₄H₉-O-CH₂-O-C₄H₉),⁴⁵ and dimethyl-ether (CH₃-O-CH₃)⁴³ have been studied in heavy-duty diesel engines or under diesel-like conditions. Up to 35% (by mass) reduced PM emission have been observed with 30% methylal in diesel.

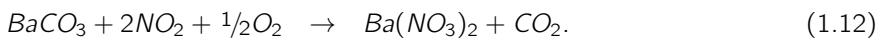
Aftertreatment

Gasoline engines, operating under slightly fuel rich conditions, can be equipped with a so-called three-way catalyst to remove the emissions of unburnt hydrocarbons, CO, and NO from the exhaust gas. These species are converted by the following reactions:

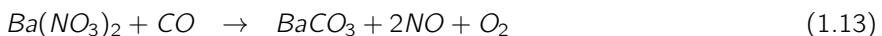


Unfortunately, reaction 1.11 does not take place under lean conditions (i.e. excess O₂), which makes it unsuitable for diesel engines. Two alternatives for NO removal are discussed here: NO_x absorbers and Selective Catalytic Reduction.

Storage catalysts In this class, also known as lean NO_x traps, NO is rapidly oxidised to NO₂, which is then stored as a nitrate, with barium carbonate as a storage material:

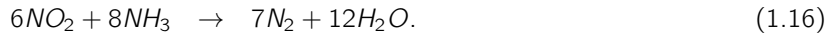


Efficiencies of 50-90% can be reached, but these catalysts need to be regenerated regularly. This is achieved either by a small fuel injection into the exhaust or by an additional late injection into the cylinders, creating a fuel rich atmosphere that allows the reaction of NO to N₂:



The regeneration of storage catalysts comes at the expense of fuel economy.

Selective catalytic reduction (SCR) SCR⁴⁶ is based on the reduction of NO and NO₂ by NH₃:



It is called selective because reaction 1.15 is preferred above oxidation of NH₃ by O₂. Instead of the poisonous NH₃, aqueous urea can be used, which dissociates into NH₃ and CO₂ when it is injected into the hot exhaust stream. Since these reactions only take place at temperatures above 430 K, research is focused on improving the low temperature performance of SCR.⁴⁷ NO_x emission reductions of 70-90% have been realised for heavy-duty diesel engines.⁴⁸ This allows tuning the engine to good fuel economy and low particulate emission (see Fig. 1.6). As a disadvantage, SCR requires a urea/NH₃ distribution system and an additional storage tank.

Diesel Particulate Filters (DPF) Both solid and liquid particulate matter (PM) can be removed from the exhaust by particulate filters. These consist of porous ceramics or metal wire meshes. DPFs are regenerated by heating the system to ~800 K while providing sufficient O₂ in the exhaust gas. With the use of catalytic coatings, the required temperature may be lowered by 200 K. Although generally high trapping efficiencies are achieved (70-90% by mass), this is not the case for ultrafine particles. The latter are believed to be the most dangerous size of PM as they may penetrate deeply into the lungs.

1.3 A brief introduction to laser spectroscopy in combustion engines

Laser diagnostics are widely employed in combustion research because of their low intrusiveness, high spatial and temporal resolution, high species selectivity, and their robustness against the harsh combustion environment. Various laser techniques exist to measure species concentrations and temperature. Below, the most popular techniques in combustion research are briefly introduced, mainly based on the extensive reviews by Eckbreth⁴⁹ and Demtröder.⁵⁰ The laser-induced fluorescence technique, used for NO measurement, will be described in more detail in Chapter 3.

Laser-induced fluorescence (LIF) Fluorescence is the spontaneous emission of radiation by molecules in an (electronically) excited state. By emitting the radiation,

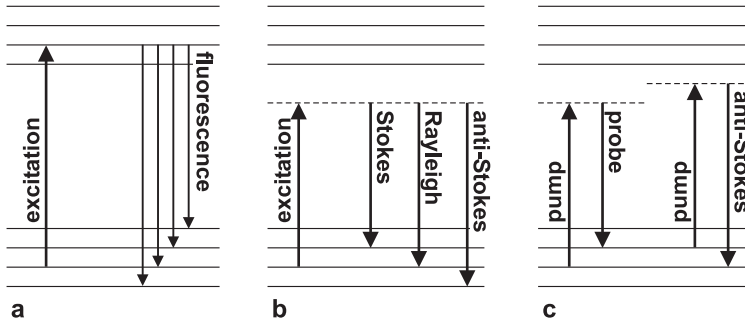


Figure 1.7: Different interactions between light (indicated as arrows) and molecules (energy levels indicated as horizontal lines). (a) Laser-induced fluorescence; (b) Rayleigh scattering and Raman scattering; (c) CARS.

they decay to a lower energy level. With *laser-induced fluorescence*, molecules are excited by absorbing one (or more) laser photon(s), see Fig. 1.7. The subsequent spontaneous fluorescence is detected and its intensity is a direct measure of the number of excited molecules. With LIF, the laser wavelength is tuned to match an absorption line of the species of interest. By monitoring the fluorescence in a particular, characteristic wavelength region while tuning the laser wavelength, one obtains an excitation spectrum. In stable flames, the temperature can be derived from the excitation spectrum, since the line intensities are proportional to the population of the corresponding energy levels, which in turn is described by a Boltzmann distribution. A prerequisite is that quenching (see the following paragraph) is the same for all involved excited energy levels.

LIF provides a high level of selectivity, since both the absorption (or excitation) spectrum and the fluorescence spectrum are characteristic “fingerprints” for each type of molecule. Compared to other techniques, LIF is very sensitive too, allowing the determination of minor species concentrations, even with two-dimensional planar imaging using a laser light “sheet”. Accurate, quantitative results can only be achieved by accounting for the various molecular energy transfer processes and quenching (i.e. radiationless decay). Quenching seriously affects the LIF intensity at elevated pressures. These processes are known only for popular combustion molecules such as OH, CH, and NO.

Due to its high sensitivity, LIF is widely used for in-cylinder measurements of NO in (diesel) engines.^{2,4,6} However, absorption by the cylinder contents often limits a quantitative interpretation. NO LIF is also a promising tool for thermometry.^{51,52}

Cavity ring-down spectroscopy (CRDS) Cavity ring-down spectroscopy is a very sensitive technique for studying minor species by means of absorption in e.g. flames. With CRDS, the object under study is placed between two highly reflective mirrors forming a cavity, and a (pulsed) laser beam is coupled into this cavity. In contrast to direct absorption, the laser beam passes the absorptive medium multiple times, which increases the absorption path length (and thus sensitivity) tremendously. After each round trip, a small fraction of the laser beam leaks out of the cavity, which is monitored by a photodetector. Without absorption, the decay of the detected light is caused only by the reflection losses of the cavity. When the laser is tuned to an absorption line of the species of interest, the decay time decreases. This can be directly related to the species density (provided its absorption cross section is known); further calibration is not needed (in contrast to LIF). With CRDS, also non-fluorescing molecules can be detected. Care must be taken that the effective path length is accurately known, and that the spatial distribution of the species along the laser path is accounted for. The latter can sometimes be monitored simultaneously, e.g. by LIF.

In diesel engines, laser beam extinction is too high to apply CRDS to in-cylinder measurements. CRDS measurement of NO and NO₂ in the exhaust have been reported.⁵³ *In-cylinder* NO column densities have been obtained from (single-pass) UV absorption spectra.⁵⁴

Rayleigh and Mie scattering Rayleigh scattering is the elastic scattering of light by molecules or small particles (in the Rayleigh regime $\lambda \gg d$, with λ and d the wavelength and particle diameter, respectively). The photon energy is in general non-resonant with the molecular energy levels; the intermediate state can be regarded as a virtual energy level (the dashed line in Fig. 1.7). As a consequence, Rayleigh scattering is not species selective, and can only be used for total density measurements. Light scattering off particles above the Rayleigh limit is called Mie scattering. Although it is much stronger than Rayleigh scattering, Mie scattering is less straightforward to interpret, primarily due to its complex dependence on the particles' shape.

Raman scattering Raman scattering is, like LIF, inelastic scattering of (laser) photons off molecules. As with Rayleigh scattering, it is a non-resonant process. The scattered photons may have either less (i.e. Stokes scattering) or more (anti-Stokes) energy than the incident photon, with an energy difference that is equal to a rotational, vibrational, or electronic energy quantum of the scattering molecule. This

makes Raman scattering a species selective process. Due to the short time scales, Raman scattering is quenching free. Unfortunately, its scattering cross section is very low (typically 10^3 times lower than the Rayleigh cross section), so measurements are restricted to majority species only. Since the laser wavelength is of minor importance, a powerful laser source is usually selected to compensate for the low efficiency. The Raman intensity increases with increasing pressure, which makes the technique applicable in engines. Furthermore, the Raman cross section can be dramatically enhanced if the virtual energy level is very close to one of the molecular energy levels (*near resonant Raman scattering*). In this case, however, the measurement may be no longer quenching free, if the nearby energy state is quenched.

In (diesel) engines, Raman spectroscopy has been applied for determination of major species,^{55,56} or e.g. the local fuel-air ratio.⁵⁷

Coherent anti-Stokes Raman scattering (CARS) CARS is a form of non-linear Raman spectroscopy, where two laser beams (pump, ν_1 , and probe ν_2) are crossed at an angle to form a third beam. Crossing of the beams is necessary to fulfill phase-matching conditions. Pump and probe laser wavelengths are chosen such that $\nu_1 - \nu_2$ coincides with a Raman-active vibration of the molecule of interest. The third beam has a frequency $\nu_3 = 2\nu_1 - \nu_2$, as is shown in Fig. 1.7c. Although CARS can be used for majority species detection only, it is primarily applied for temperature (point) measurements, with high accuracy (10–100 K).

Although generally restricted to temperature measurements in the compression stroke, CARS has been performed in engines.^{58–60}

Two-line atomic fluorescence (TLAF) TLAF is another technique for temperature measurement.⁶¹ Metal atoms (usually Indium is used for its applicability over a wide temperature range) are seeded into the combustion environment. As two time-delayed laser pulses probe two different energy levels on transitions with a common upper level, the temperature can be derived from the ratio of the ensuing fluorescence intensities. Operating in the visible wavelength range, TLAF is less prone to attenuation, which makes it a promising technique for measurements in diesel engines.

1.4 Outline of this thesis

NO_x emissions from diesel engines cause serious environmental and health-related problems. They can only be thoroughly addressed with the further optimisation of both the combustion process and the aftertreatment technology. A good understanding of the combustion process, especially the formation of nitric oxides, is therefore a prerequisite.

The work presented in this thesis focusses on the development of laser techniques to allow quantitative, in-cylinder NO LIF measurements in a diesel engine. In order to realise a quantitative interpretation of the fluorescence signal, one has to account for (1) the strong attenuation of both the laser beam and the fluorescence, and (2) the pressure and temperature dependent photophysics of NO. The second issue requires both a good spectroscopic model and knowledge of the local temperature and pressure. Whereas a number of spectroscopic models predicting the NO LIF pressure and temperature dependence have been developed over time,^{62–64} there are only few techniques for local temperature measurements in flames, most of which are not feasible in combustion engines due to the strong beam steering and attenuation effects. Moreover, attenuation effects are difficult to determine accurately, and as a consequence they are usually estimated, or assumed negligible.

This thesis presents a novel measurement strategy to measure local attenuation coefficients for both the laser beam and the induced fluorescence, for the first time allowing a complete attenuation correction of the NO LIF signal, and thus fully quantitative results. A technique to measure absorption of the NO fluorescence by O₂ and CO₂ is discussed in Chapter 4. It will be revisited in Chapter 5, where a variety of techniques will be discussed, each revealing a part of the attenuation involved in NO LIF experiments. It will be shown that a complete picture of the attenuation can only be obtained by comparing and combining different techniques. In addition, the temperature dependence of the O₂ and CO₂ absorption spectra will be shown a powerful tool to estimate local temperatures.

Chapter 6 deals with the various data processing steps, including the attenuation corrections from Chapter 5, necessary to arrive at quantitative NO measurements. In-cylinder concentration histories of NO are presented for two probe locations in the optical diesel engine with cam-driven fuel injection. For the measurements closest to one of the fuel sprays, NO is observed *before* local temperatures are sufficiently high for thermal NO formation, suggesting that other mechanisms, too, play a role in the (initial) formation of nitric oxide.

After mounting a common-rail fuel injection system to the measurement cylin-

der, similar LIF experiments have been performed as a function of fuel injection timing (Chapter 7). Since advancing the injection timing increases the premixed combustion fraction and the combustion temperature, it is of great interest to correlate these effects to the observed NO formation. The NO LIF experiments are interpreted within a framework of additional information from high-speed movies of the combustion and numerical simulations.

Although the LIF technique was already briefly explained in Section 1.3, various NO LIF strategies as well as its p, T dependence will be discussed in more detail in Chapter 3. The optical engine will be introduced in Chapter 2.

Chapter 2

The research engine

2.1 Introduction

In this chapter the research engine will be discussed in some detail, focussing on the modifications providing optical access to the measurement cylinder (Section 2.2) and presenting some characteristics such as cylinder pressure and apparent rate of heat release for this cylinder (Section 2.3). In Section 2.4, attention will be paid to the common-rail fuel injection system that was fitted later. With this system, injection timing and pressure for the measurement cylinder can be chosen at will, which is not possible with the original, cam-driven system. The possibility to vary the fuel injection timing while monitoring its effect on NO formation forms the basis of Chapter 7.

2.2 Optical access

The research engine is a six-cylinder, 11.6-litre heavy-duty engine (WS 1160 model series) from DAF Trucks (Eindhoven, the Netherlands). One of the cylinders of this engine was modified to provide optical access.⁶⁵ This will be called the measurement cylinder. It is equipped with a cylinder head according to the design of the combustion chamber of the (more modern) XF 95 engine model. It features a central, eight-hole fuel injector and two air intake valves. The fuel supply connection on the fuel injector was moved from the side of the injector to the top, allowing the injector to be rotated around its (vertical) axis. This way, the eight fuel sprays can be oriented in any desired direction. The regular XF 95 model has two exhaust valves

per cylinder, but for the research version one valve has been replaced by a 28-mm diameter quartz window ("top window") or a pressure transducer (AVL QHC32) in the top of the cylinder head. See also Fig. 2.1 for a cross section of the cylinder and Table 2.1 for its dimensions and typical operating conditions. Three more windows ("side windows") of $48 \times 23 \text{ mm}^2$ are placed in the sides of the head, two opposite to each other and one at 90° . The top of the side windows is flush with the cylinder head. Finally, a large $\varnothing 74 \times 49 \text{ mm}^2$ window ("piston window") is mounted in the piston. Instead of maintaining the "omega" shape of the original piston crown, the piston window has flat surfaces to prevent image distortion (although it would be possible to correct for this^{8,66}). All windows are made of high-purity synthetic fused silica (Suprasil 1, Heraeus Optics) to prevent degradation by the intense UV laser radiation. A slot ($17 \times 11 \text{ mm}^2$) machined in the piston crown allows observation of the combustion chamber through one of the side windows even at TDC. Because of this slot and the flat window surfaces the compression ratio is reduced from 16 to 15. This was partly compensated by increasing the intake air pressure so as to maintain a TDC pressure of around 42 bar, although this inevitably leads to pressures that are slightly too high later in the stroke. Still, the fuel injection, auto-ignition, and early combustion (all occurring within $\sim 10^\circ$ around TDC) take place at realistic pressures.

No lubricant oil is used inside the measurement cylinder, as it would absorb the ultraviolet laser and fluorescence radiation. Besides, lubricants may lead to additional soot formation. Overheating of the cylinder is prevented by skip-fired operation, with a duty cycle of typically 1:35. This way, measurement sessions of 30 minutes up to one hour can be realised. Problems of wear due to the lack of lubricants are addressed by using a rider ring and a piston ring of relatively soft materials such as bronze impregnated teflon, and polyamide filled with molybdenum sulfide and graphite, respectively. The piston ring is pushed outward radially by a steel expander ring. The piston and rider rings are replaced regularly; their condition determines the amount of blow-by (i.e. leakage) which can be monitored via the cylinder pressure.

In order to be able to mount a 45° mirror below the piston window, the measurement cylinder is actually built on top of the original cylinder, following the concept introduced by Bowditch in 1961.⁶⁷ The original piston was left in place but it was elongated by a 40-cm extension onto which the optical piston is bolted (see Fig. 2.1). The quartz piston window is mounted between the extension and the piston crown. To cope with the different thermal expansion rate of the aluminium crown, the window is fixed between rings made of relatively soft materials: graphite

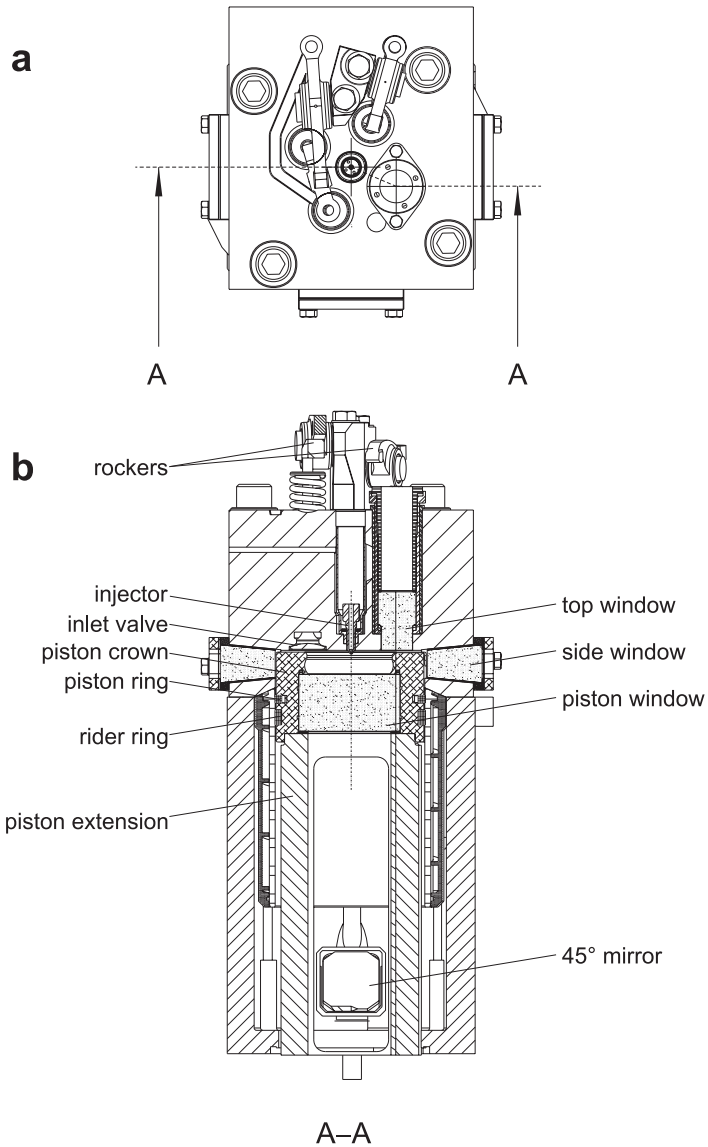


Figure 2.1: Top view (a) and vertical cut-through (b) of the measurement cylinder. Note that the cut is not in one plane, as is indicated by the line A–A in the top view.

sheets reinforced with steel foil,⁶⁸ and copper, respectively. The elongation of the cylinder also simplifies the mounting of side windows, and it improves the access for laser beams and detection equipment. The engine is kept in balance by increasing

Table 2.1: Specifications and operating conditions of the measurement cylinder.

geometry:	
bore	130 mm
stroke	146 mm
displacement	1.939 ℓ
compression ratio	15 (unmodified: 16)
swirl number	1.8
valve data:	
inlet opens	360° bTDC
inlet closes	170° bTDC
exhaust opens	130° aTDC
exhaust closes	360° aTDC
fuel injector (line pump):	
injector holder	Bosch 971 105094933 B432001277 MUB
injector tip	Bosch DLLA155PV3181706
∅ nozzle	0.230 mm
# holes	8
fuel injector (common-rail):	
injector holder	Bosch CR 12.8.1 B2 sample
injector tip	Bosch DLLZ160PV3370 685 569
∅ nozzle	0.128 mm
# holes	8
operating conditions:	
fuel injected	60 mg of low-sulphur diesel
boost pressure	1.4 bar (absolute)
engine speed	1430 rpm

the weight of the two pistons adjacent to the measurement cylinder. No fuel is injected into these cylinders, so that the entire engine is driven by the three remaining cylinders.

The operation conditions of the measurement cylinder can be controlled independently from the other cylinders. For the original fuel injection system, i.e. a cam-driven line pump system, the amount of fuel injected into the measurement cylinder is governed by a separate control rack that can switch rapidly to allow skip-fired operation. Unlike the *amount* of fuel injected, the injection *timing* and

pressure cannot be changed as they depend on the cam phase and shape. Furthermore, the intake air for the measurement cylinder can be heated and pressurised independently. Typical conditions are 40°C and 1.4 bar absolute to simulate turbocharging. The other working cylinders are normally aspirated. Before each engine run, the measurement cylinder is warmed up to 60°C by heating the cooling water. During the measurements, the cooling water temperature is allowed to increase by no more than 10°C. The engine speed (1430 rpm) is stabilised by an eddy-current brake (Schenck W450). All engine conditions, including the load for the “normal” cylinders, are monitored and controlled from a single integrated control unit.

In order to synchronise the measurement equipment to the motion of the measurement cylinder, the crank shaft is equipped with an optical angle encoder, providing a trigger pulse at any desired crank angle (in steps of 0.1°), and two additional pulses for every full rotation of the crank shaft and cam shaft, respectively.

2.3 Engine characteristics

Most of the operation conditions of the measurement cylinder are given in Table 2.1; they correspond roughly to what would be 25% load in an unmodified engine. For all experiments, low-sulphur city diesel has been used. Additional information is contained in the cylinder pressure trace. The cylinder pressure under the conditions of Table 2.1 is shown in Fig. 2.2a. The start of combustion, at around 3° aTDC, gives rise to a second pressure increase: due to the sudden temperature rise, the pressure increases even though the cylinder volume is expanding. This can be seen more clearly in the apparent rate of heat release²⁹ that can be calculated from the cylinder pressure according to Eq. 1.1. Although heat losses and blow-by are not accounted for in this analysis, the heat release rate (HRR) still provides important information on the start and end of combustion, and the combustion mode (e.g. the burning rate, and premixed and mixing-controlled fractions). The heat release rate, derived from the cylinder pressure, is shown in Fig. 2.2b. By comparing Figs. 2.2 and 1.4, it becomes clear that at 25% load a major fraction of the heat release is due to premixed combustion; the broad mixing-controlled feature is only weakly present between 10° and 20° aTDC. Previous measurements have shown increasing mixing-controlled combustion at 50% and 75% load,⁶⁵ as would be expected. The *average* gas temperature can be obtained by integrating the HRR:

$$T(\vartheta) = T_0 + \frac{1}{m c_v} \int_{\vartheta_0}^{\vartheta} \left[\frac{dQ(\vartheta')}{d\vartheta'} - p(\vartheta') \frac{dV(\vartheta')}{d\vartheta'} \right] d\vartheta', \quad (2.1)$$

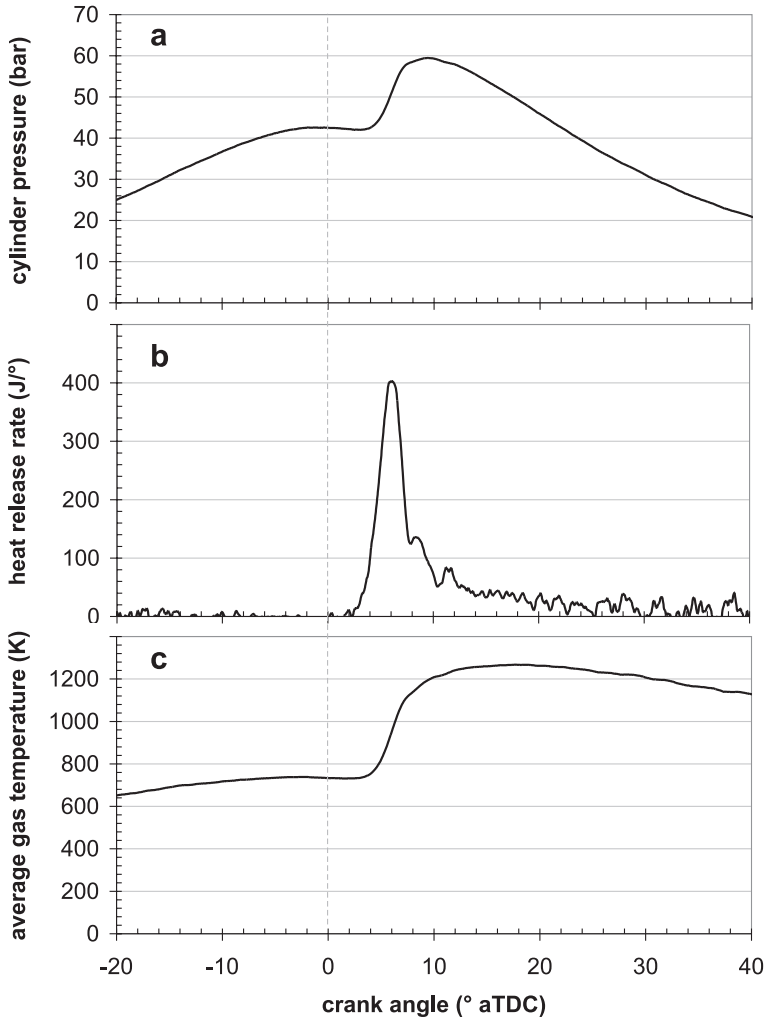


Figure 2.2: Cylinder pressure (panel a), rate of heat release (panel b), and average gas temperature (panel c) for the measurement cylinder under 25% load conditions.

representing the volume averaged gas temperature. It is shown in Fig. 2.2c. A maximum of 1270 K is observed, but it should be emphasised that local temperatures may reach values in excess of 2500 K.*

*Since the thermal NO formation mechanism shows an almost exponential dependence on temperature, it is obvious that the average gas temperature cannot be used to estimate the in-cylinder NO density.

A commonly used expression for the output work per cylinder is the indicated mean effective pressure (IMEP). It is obtained by dividing the area of the p-V diagram (see e.g. Fig. 1.3) by the displaced volume per cylinder, yielding an effective pressure. In case of the *gross* indicated mean effective pressure (gIMEP), only the compression and power strokes are taken into account, i.e. pumping losses during the inlet and exhaust strokes are neglected:

$$\text{gIMEP} = \frac{1}{V_{\text{displ}}} \int_{\vartheta=-180^{\circ}}^{\vartheta=180^{\circ}} pVd\vartheta'. \quad (2.2)$$

Using the pressure data in Fig. 2.2, a gIMEP of 530 kPa is calculated.

The exact start and end of the fuel injection have been monitored by means of a needle lift sensor. The needle is a central part of the fuel injector, opening the nozzle orifices when it is lifted by the fuel pressure (see Fig. 2.3). Thus, the moment when the needle rises (or falls) indicates the start (or end) of injection. The needle is pushed down by a spring, and opens at a fuel pressure of 230 bar. Both the injector pressure and the needle lift are shown in Fig. 2.3. Due to the shape of the cam driving the fuel pump plunger, the injection pressure is not constant but increases almost linearly instead. The curve for 50% load (96 mg injected per cycle) is shown for comparison. At 25% load, a maximum pressure of just over 450 bar is reached, as compared to well over 600 bar for 50% load. The injection duration for 25% load is approximately 11°.

2.4 The common-rail fuel injection system

With a common-rail (CR) system, the fuel injection is no longer powered by the camshaft driving the plungers that each provide one cylinder with fuel. Instead, all injectors are connected to one common supply (the rail) that is kept at a constant pressure by an electric fuel pump. This means that the injection pressure remains (almost) constant during the entire injection event. Fuel injection is regulated electronically by means of a solenoid-actuated valve (needle), which allows a more precise control of the injected fuel quantity. High injection pressures (1000–2000 bar), combined with smaller nozzle orifices, improve the fuel spray atomisation and the subsequent mixing of fuel and air, which reduces the soot formation. Since the injection is controlled electronically, the injection timing and duration can be controlled freely.

The flexible injection timing and the high injection pressures are the two main reasons for mounting a common-rail system to the measurement cylinder of the

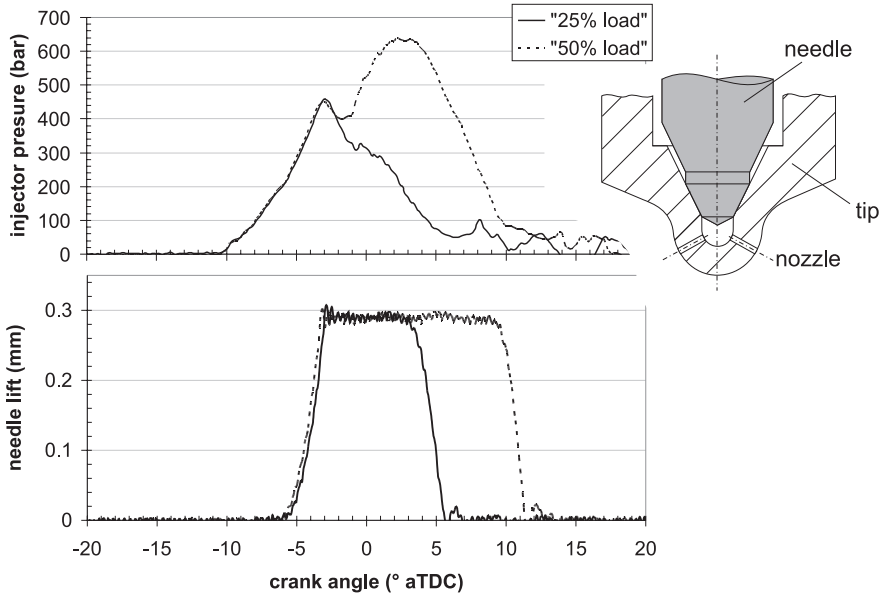


Figure 2.3: Injector pressure (upper panel) and needle lift (lower panel) for the line pump, at 25% and 50% load, as well as a schematic picture of the injector tip (on the right). The 8-hole injector (nozzle orifices of $\varnothing 230 \mu\text{m}$) opens at 230 bar.

research engine in Nijmegen. The fact that the timing of the fuel injection has a significant influence on the amount of NO_x formed (as was discussed in Chapter 1) makes it an interesting parameter to study. Furthermore, it was questioned whether the expected reduction of soot would lead to an improved optical transmission of the laser beam and the fluorescence during NO LIF measurements. These two issues are further discussed in Chapter 7.

High-speed fuel spray visualisation

The many degrees of freedom in the new system, like injection pressure, timing, and duration, and choice of nozzle orifice diameter, required a better understanding of their influence on the spray characteristics. One point of concern was the possibility of liquid fuel reaching the relatively cold cylinder wall (“wall wetting”), causing unnecessary soot formation. In order to determine an appropriate operating setting for the measurement cylinder, a number of experiments were carried out, focussing on (1) the cylinder pressure (and HRR), and (2) high-speed visualisation

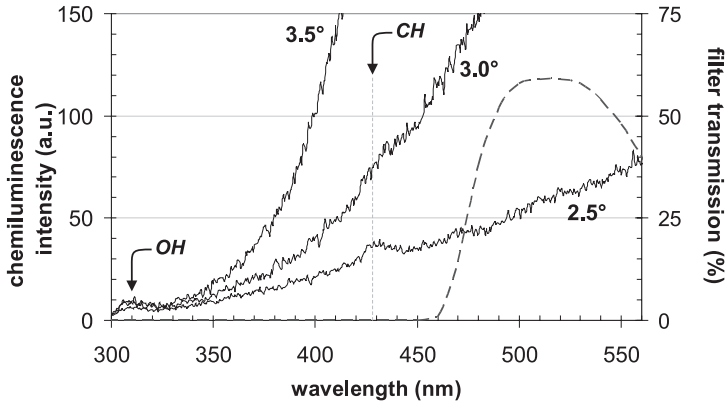


Figure 2.4: Solid lines: chemiluminescence spectra taken recorded from the measurement cylinder, equipped with the line-pump; dashed line: transmission spectrum of the filter used for the high-speed movies. Crank angles (in $^{\circ}$ aTDC) are indicated. The broadband, sloping curve is attributed to soot incandescence. After 3.5° aTDC, it overwhelms the CH feature.

of the fuel injection. Measurements were performed under both non-reacting (N_2) and reacting environments (air, see Section 2.4). The fuel sprays were illuminated by a continuous-wave Argon ion laser beam (Spectra Physics, Stabillite 2016) of circa 5 W (operating at a.o. 488 and 517 nm), entering via the piston window. The laser beam was directed towards a 16-mm diameter metal sphere located below the piston window, resulting in a highly divergent reflection illuminating almost the entire combustion chamber. The scattered light was recorded through the same window by a high-speed camera (Phantom V7.1, 160 kHz maximum frame rate). In order to maintain frame rates of 31 kHz (0.27° CA), the image size was limited to 304×184 pixels, capturing only one or two sprays completely, with a resolution of $143 \mu\text{m}$ per pixel for the N_2 measurements. For the measurements with air, the resolution was $275 \mu\text{m}$ per pixel. The combustion light was suppressed by a filter combination (BG 18 and GG 475 Schott coloured glass filters), transmitting between 460 and 640 nm, with a maximum around 520 nm. This means that not only scattered laser light is detected, but also a fraction of the natural combustion luminosity. The latter is interpreted as soot incandescence, because OH and CH chemiluminescence are beyond the spectral transmission of the filter set and the sensitivity of the camera; besides CH chemiluminescence is generally overwhelmed by the soot intensity, see Fig. 2.4. The setup is depicted schematically in Fig. 2.5.

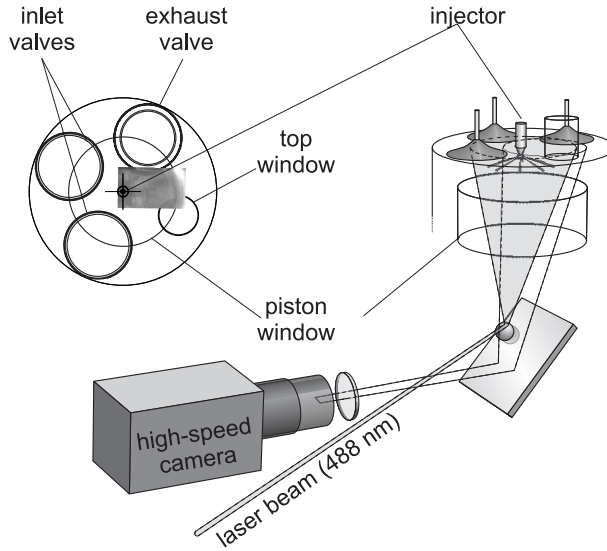


Figure 2.5: Three-dimensional schematic representation of the setup. The camera field-of-view is indicated in the top view of the measurement cylinder (upper left).

The air intake buffer vessel was continuously filled with either air or N_2 . In order to use the limited supply of N_2 per measurement session as efficiently as possible, a valve was mounted to be able to switch to N_2 only during the actual measurements. The rail pressure was set at 1200 bar, slightly below the maximum pressure (1400 bar) to ensure reliable operation, but considerably higher than the maximum line pump pressure. Two different injector tips were used (orifice diameter of tip 1: $184 \mu\text{m}$; tip 2: $128 \mu\text{m}$). The amount of fuel was kept at 60 mg per cycle, as it was for the line-pump experiments. It was soon discovered that the injector tip with larger nozzle orifices caused very short injection durations ($\leq 5^\circ$), with insufficient time to fully lift the injector needle. As this caused a very short, intense combustion, it was decided to use the $128\text{-}\mu\text{m}$ tip for which the injection of 60 mg at 1200 bar and 1430 rpm lasts approximately 15° . Figure 2.6 shows an image sequence of a fuel injection with inert environment. The fact that the fuel sprays seem “detached” from the injector is an artifact of the measurement technique: over the first few millimetres the liquid fuel spray remains intact before it breaks up into droplets. Because scattering by an ensemble of droplets is much more efficient than that by the liquid core, the latter is hardly visible in the images. Light scattering by fuel vapour is too weak to be detected. As a result, the images mainly show fuel

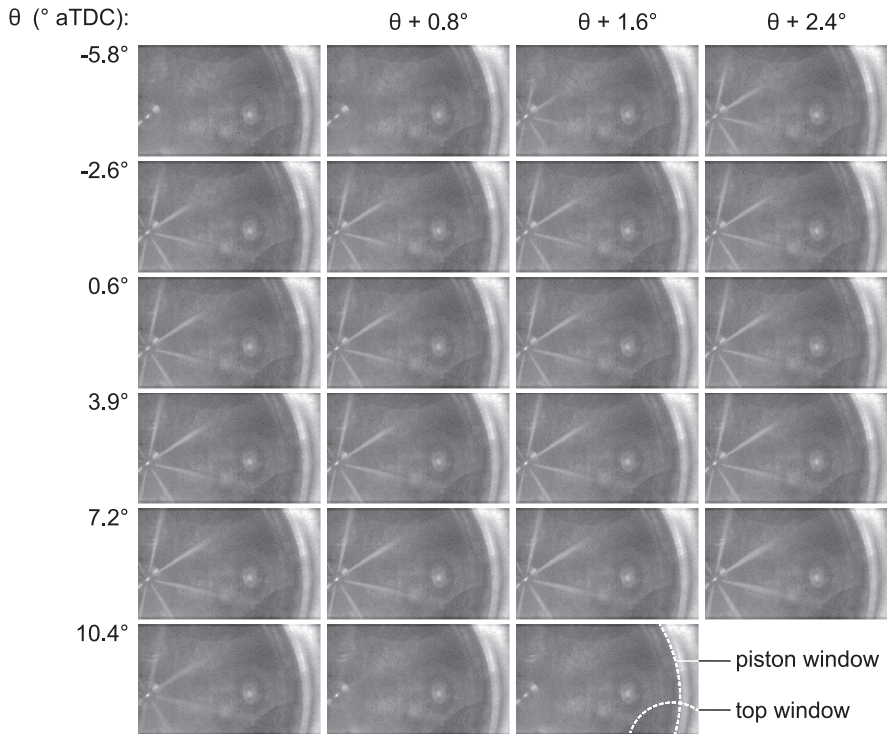


Figure 2.6: “Movie” of a single fuel injection into N_2 environment, with the common-rail system. Rail pressure: 1200 bar; fuel injected: 60 mg; nozzle \varnothing : 128 μm ; boost pressure: 1.4 bar. Injection trigger (current): 8.0° bTDC; actual Sol: 4.7° bTDC. Crank angles are indicated (only every third frame is shown, increasing the inter-frame time from 0.27° to 0.8°). The bright dots above the top window are an artefact (probably reflections off the cylinder head).

droplets. The liquid core could, however, be visualised more effectively with LIF, which is sensitive to fuel volume fraction. Previous measurements in this engine have shown the strongest LIF signals over the first 2-3 mm from the injector indicating the liquid core.⁶⁵

The image sequence in Fig. 2.6 proves that wall wetting does not occur, since no spray droplets are observed further than halfway between the injector and the piston bowl wall. In Fig. 2.7a an image sequence for the line pump system is shown. Comparing the spray behaviour of the common-rail system to the line-pump system reveals that the CR-sprays are narrower and shorter than the sprays produced by the line-pump system. The latter can be explained by the fact that smaller orifice diameters

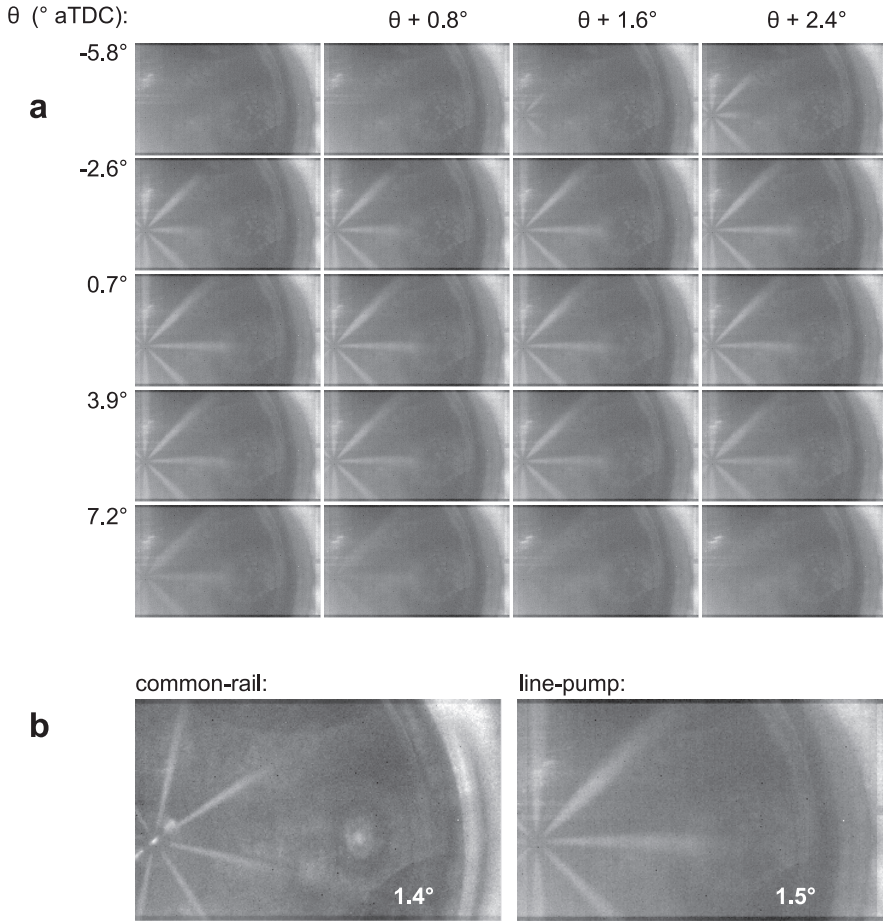


Figure 2.7: Panel a: “movie” of a single fuel injection into N₂ environment, with the line-pump system. Fuel injected: 60 mg; nozzle \varnothing : 230 μm ; boost pressure: 1.4 bar. Start of injection (needle lift): 5.3° bTDC; first sprays visible at 4.4° bTDC. Crank angles are indicated (only every third frame is shown). Panel b: enlarged images from panel a (line-pump) and Fig. 2.6 (common-rail).

lead to a shorter liquid length, i.e. the maximum distance from the nozzle at which fuel droplets can be found.^{69,70} (Based on this trend, on hindsight the initial questions about wall wetting seem unfounded considering that the nozzle diameter was decreased from 230 μm to 128 μm .) The injection pressure has no significant influence on the liquid length, because both the fuel injection rate and the entrainment of ambient air depend on the injection pressure in the same manner. Consequently,

the distance needed to vaporise all fuel remains the same.^{69,70} The improved atomisation and evaporation of the fuel spray in the case of smaller nozzle holes reduces the volume occupied by light scattering droplets, leading to the smaller spray angles (i.e. narrower sprays) in the image sequence of the common-rail experiments, see also Fig. 2.7b.

The rail pressure as well as the (uncalibrated) needle lift signal are shown in Fig. 2.8. Since the needle lift signal was converted by non-linear electronics, the resulting curve can only be interpreted qualitatively. Before injection the rail pressure is constant, but it drops by 150 bar when the needle is lifted. The oscillations are due to reflecting pressure waves. The sharp increase at 11° aTDC is caused by the sudden closing of the injector (similar to the water shock effect when a tap is suddenly closed). Although the solenoid current is triggered to rise at 8° bTDC, the first fuel is visible at only 4.7° bTDC (based on the movie in Fig. 2.6), coinciding with a little “hump” in both the pressure and needle lift curves. The end of injection as determined from the movies (11.1° aTDC) is in good agreement with the rail pressure data. The needle lift signal, however, does not unambiguously indicate the exact end of injection.

High-speed visualisation of the combustion process

Spray measurements were also performed with air instead of N_2 . It turns out that the combustion process is very different for both injection systems, even though the starts of injection are almost equal (common-rail: 4.7° bTDC, line-pump: 4.4° bTDC). The injection *duration* with the common-rail system is somewhat longer (15.4° vs. 11.4° ; values based on the data in Figs. 2.6 and 2.7). Figure 2.9 shows that with the common-rail system, the heat release rate is less pronounced, with a peak value that is almost 50% smaller than with the line-pump. Instead it spreads over a longer time, and it is difficult to recognise the premixed and mixing-controlled phases (compared with the example in Fig. 1.4). With the common-rail system, auto-ignition occurs approximately 2.0° earlier. The 1.7° shorter ignition delay, compared to the line-pump, can be explained by the improved spray atomisation and the ensuing mixing of fuel and air.

The image sequences of the combustion process for the two injection systems are shown in Figs. 2.10 and 2.11. In both images the effect of swirl is evident, causing a clockwise motion of the flames. Even after the heat release, the line-pump movie still shows considerable combustion luminosity (soot incandescence), whereas the common-rail movie is almost dark after 33° aTDC. This suggests that

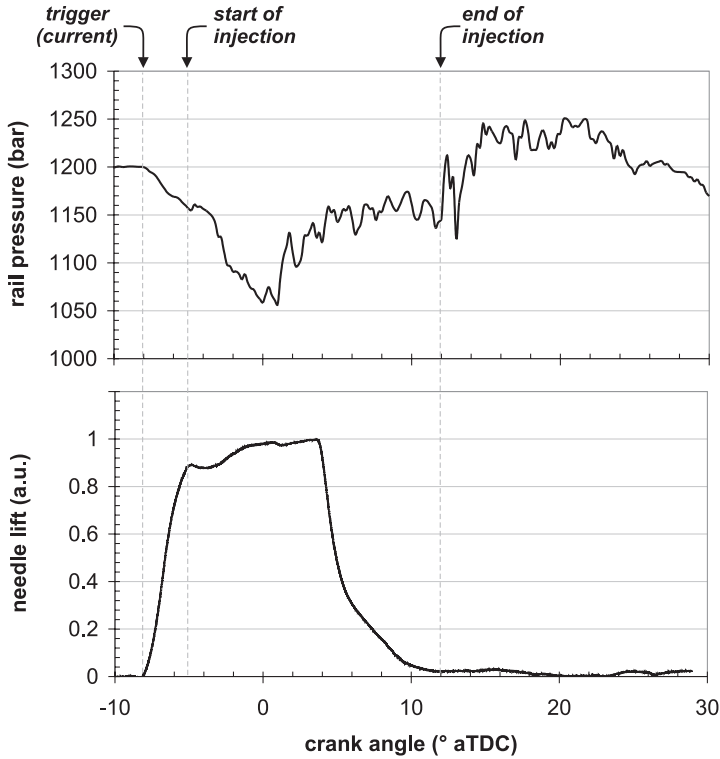


Figure 2.8: Injector pressure (upper panel) and uncalibrated needle lift (in arbitrary units, lower panel) for the common-rail fuel injection system. The solenoid current is triggered at 8° bTDC; the start and end of injection are also indicated.

less soot is formed with the latter, as expected*. However, lower temperatures and thus weaker incandescence could be another plausible explanation.

It appears that with common-rail injection the first combustion luminosity (i.e. soot) shows up close to the piston bowl rim, and only later does the flame stabilise closer to the injector. This is in contrast to the line-pump measurements where the first spots appear roughly halfway between the injector and the piston bowl, close to the point where the flame stabilises. These observations are possibly explained by the higher spray velocity in case of the common-rail system (the initial velocity scaling with the square-root of the pressure drop across the injector¹⁸), but a de-

*This is in agreement with the observed cleaner quartz windows after a measurement session. Besides, LII experiments have shown considerably lower signal intensities with the common-rail system.⁷¹

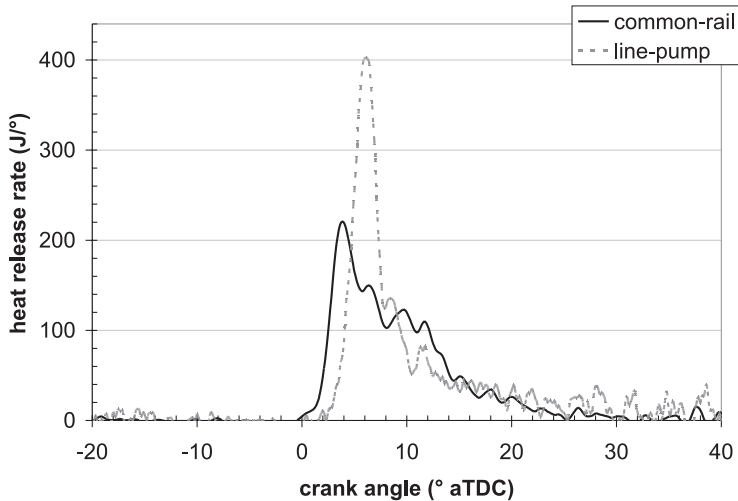


Figure 2.9: Rates of heat release for the common-rail and line-pump systems. Fuel injected: 60 mg; boost pressure: 1.4 bar. Start of injection: 4.7° bTDC (common-rail) and 4.4° bTDC (line-pump).

tailed, quantitative analysis is beyond the scope of this chapter. The distance of the flame stabilisation point to the injector is also known as the flame lift-off length (FLOL).⁷² It is considered a useful diagnostic parameter,⁷³ as it yields important information on air entrainment. Flame lift-off lengths can be measured relatively easily using OH chemiluminescence or OH LIF as a flame front marker.⁷² Siebers and Higgins have measured flame lift-off lengths over a wide range of injector nozzle diameter and fuel injection pressure,⁷⁴ showing that the lift-off length increases with increasing nozzle diameter ($\text{FLOL} \propto d^{0.34}$) and with increasing injection pressure ($\text{FLOL} \propto \text{spray velocity}$). Interpolating their findings to these measurements, it is expected that for the common-rail system the flame lift-off length is $\sim 20\%$ higher than for the line-pump. In practice, however, for both systems the flame seems to stabilise at the same distance from the injector. It should be noted that the images here show soot incandescence rather than OH chemiluminescence being outside the spectral detection range. This limits a quantitative interpretation, as OH is generally observed closer to the injector.⁷²

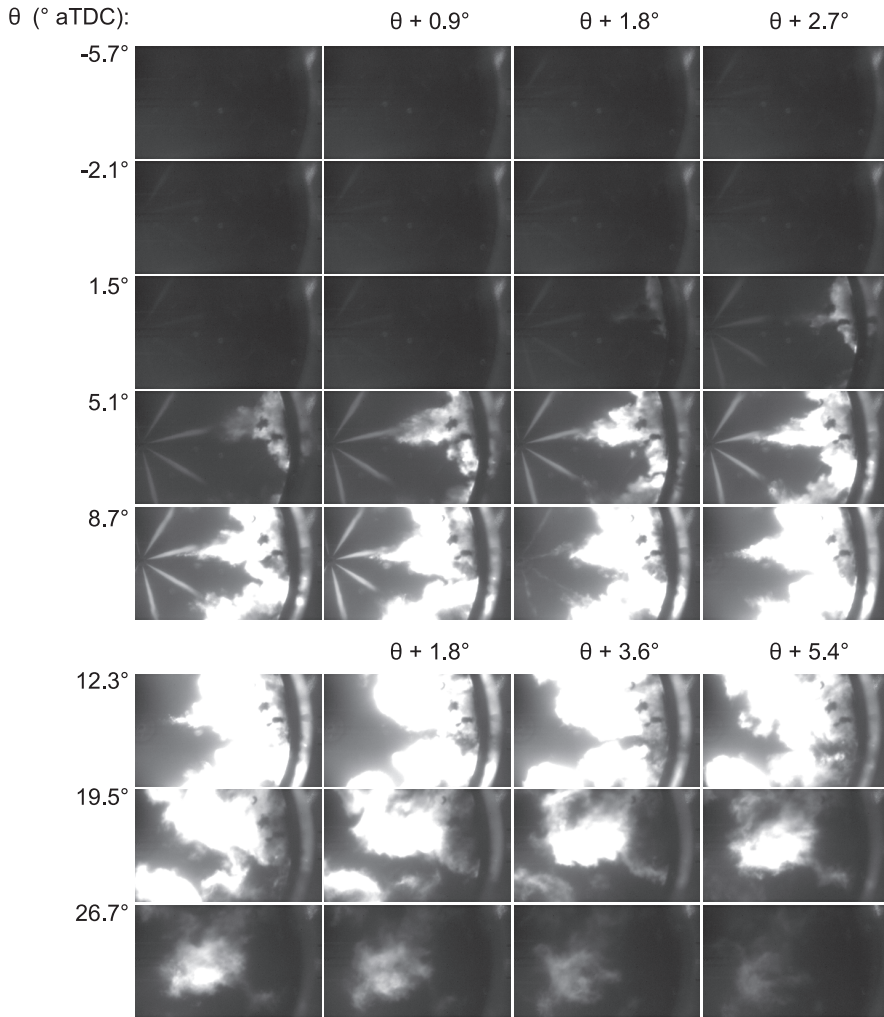


Figure 2.10: “Movie” of a single combustion event with the common-rail system. Same engine settings as in Fig. 2.6. Crank angles are indicated; notice the slightly larger crank angle steps compared to Figs. 2.6, 2.7, and 2.11. Due to lower laser intensity, before combustion the fuel sprays are not as clear as in the other movies.

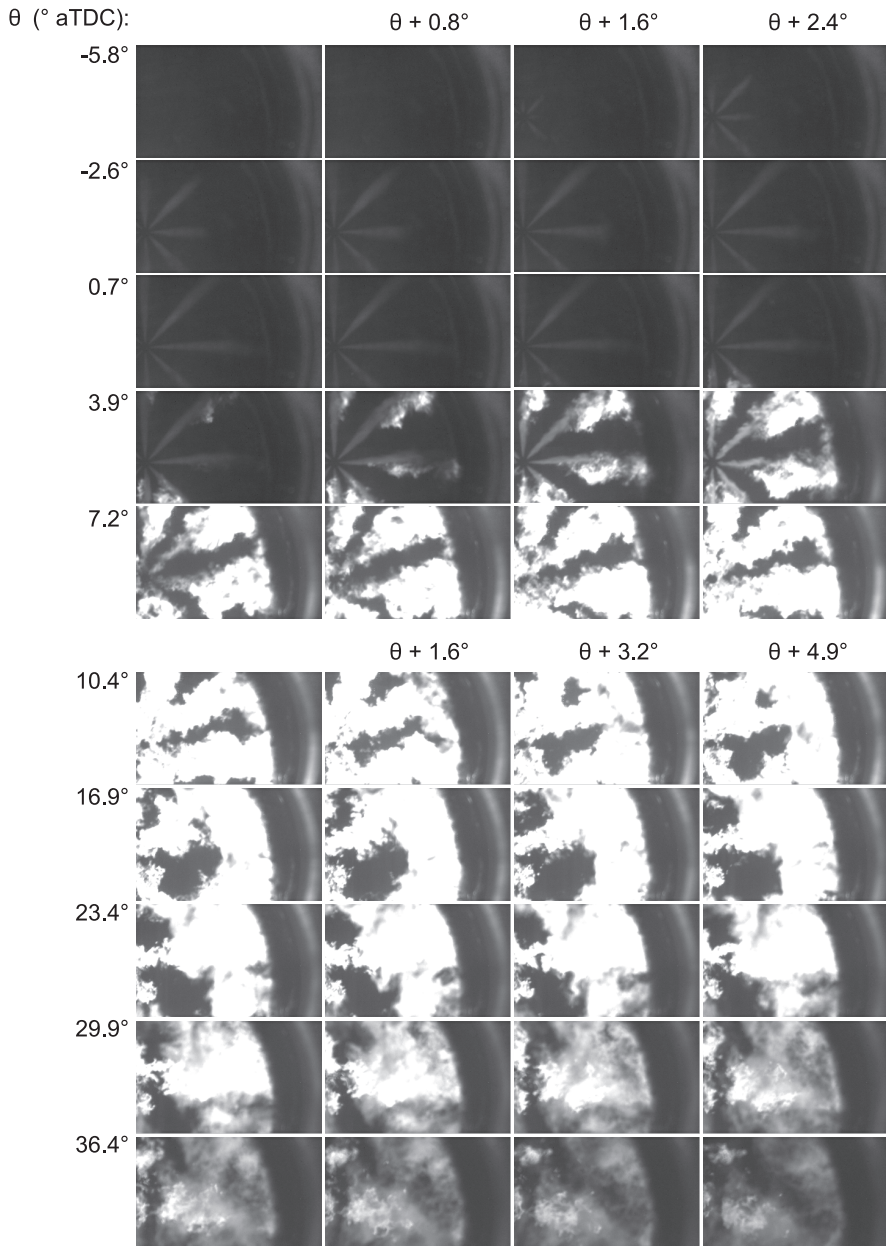


Figure 2.11: “Movie” of a single combustion event with the line-pump system. Same engine settings as in Fig. 2.7. Crank angles are indicated.

Summary

High-speed movies have been recorded for the common-rail and line-pump systems, under both inert (N_2) and reactive (air) conditions. The major observations can be summarised as follows:

1. Wall-wetting is not an issue with the injector nozzles and injection pressures investigated here, in agreement with the fact that smaller nozzle orifices cause shorter liquid lengths.
2. There is a delay between the start of the needle lift and the actual start of injection as determined by the spray movies. This delay is $\sim 3^\circ$ for the common-rail system and $\sim 1^\circ$ for the line pump.
3. The common-rail injection causes a smoother heat release as compared to the line-pump. This is in agreement with the shorter ignition delay and the longer injection duration.
4. With the line-pump, glowing soot remains visible even after the end of the heat release, which is not the case for common-rail experiments. This suggests that the common-rail injection leads to reduced soot formation.
5. With common-rail injection, the first soot luminosity appears close to the piston bowl rim; during the line-pump measurements it is much closer to the injector.
6. The fact that the flame lift-off length is the same for both injection systems does not agree with FLOL trends reported in literature.⁷⁴ However, the actual flame front, indicated by OH chemiluminescence rather than soot incandescence, was not monitored in these experiments.

2.5 Exhaust NO concentration measurements

The exhaust NO concentration has been measured by a commercial exhaust gas analyser (SIGNAL Instruments, NOX analyser series 4000). Its sampling probe is connected to the exhaust pipe of the measurement cylinder, and the probed gases are led to the analyser through electrically heated tubing (kept at 473 K to prevent water condensation). In the analyser, the gases are dried and diluted. The actual NO concentration measurement is based on the chemiluminescent reaction of NO

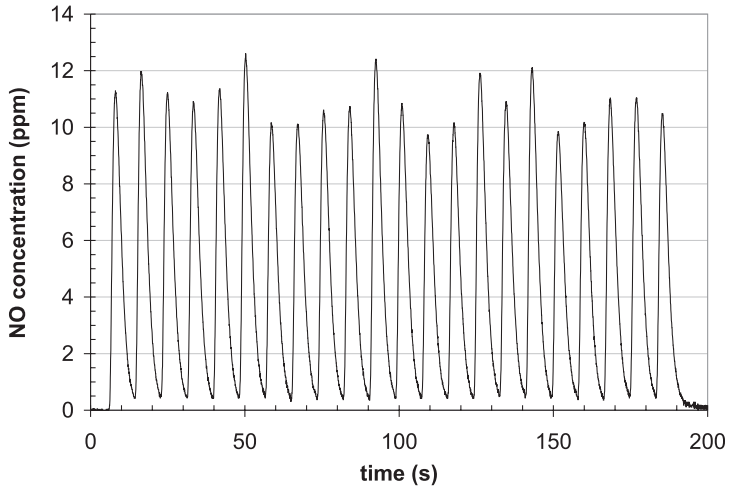


Figure 2.12: The exhaust NO concentration of the measurement cylinder for 22 fuel injections, at a skip-fire ratio of 1:99, with the line-pump fuel injection system.

with ozone:



About 10% of the formed NO_2 is electronically excited, and gives rise to light emission (chemiluminescence), which is proportional to the NO mass flow rate, and is detected by a photomultiplier tube.

Fig. 2.12 shows a typical exhaust NO concentration curve as measured by the analyser. Due to mixing of the exhaust gas from a fired cycle with previous and following non-fired cycles, the NO “pulse” of each fired cycle is spread over ~ 10 seconds (rather than the 84 ms corresponding to one cycle). Consequently, the detected NO concentration is much lower than the concentration of the undiluted pulse. In order to separate all NO pulses, the measurement cylinder was fired at the maximum skip-fire ratio allowed by the control system (i.e. 99 cycles instead of the usual 1:35), corresponding to 8.3 s between fired cycles. This way, both the average NO concentration and the cycle-to-cycle variations can be calculated. A consequence of skip-firing is that the exhaust gas of a fired cycle is strongly diluted with the compressed air resulting from previous and following motored cycles. If the exhaust gas were measured isokinetically (i.e. equal sampling speed for all cycles), the NO concentration from a fired cycle would simply equal the average concentration times the skip-fire ratio. In practice, it was observed that the hot exhaust from fired

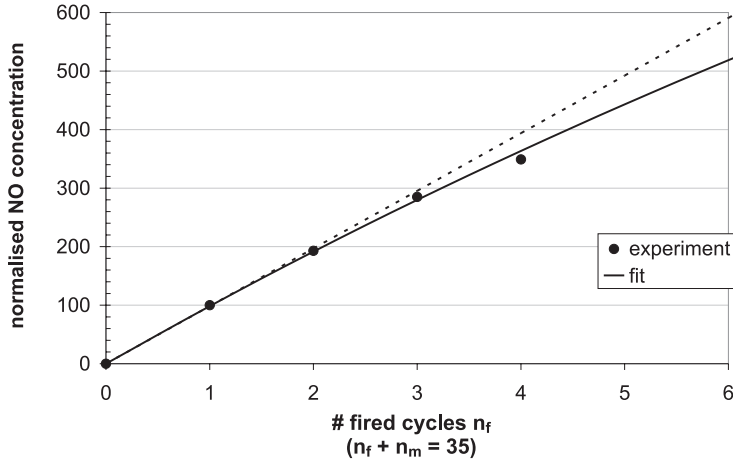


Figure 2.13: Normalised, measured exhaust NO concentration⁷⁵ as a function of the number of fired cycles per 35. The dashed straight line assumes a linear dependence; the curved solid line yields a bias of $\xi = 2$.

cycles is sampled more effectively, thus biasing the average concentration. This is demonstrated in Fig. 2.13, showing a sub-linear dependence of the analyser reading as a function of fired cycles per 35. The fit is given by the equation:

$$[NO]_{\text{meas}}(n_f) = \frac{\xi n_f [NO]_{\text{actual}}}{n_m + \xi n_f}, \quad (2.4)$$

with $[NO]_{\text{meas}}$ the measured NO concentration, $[NO]_{\text{actual}}$ the actual NO concentration from a fired cycle, n_f and n_m the number of fired and motored cycles, respectively, and ξ the “bias” towards a fired cycle. The best fit is obtained with $\xi \approx 2$, indicating that a skip-fired exhaust measurement overestimates the NO concentration from a fired cycle by approximately a factor of two. Obviously, for $n_f = 35$ (and $n_m = 0$) one would directly measure the NO concentration of a fired cycle. In general, the higher n_f , the more accurate the value of ξ . In practice, n_f is restricted to low values in order to prevent damage to the non-lubricated measurement cylinder.

Taking Eq. 2.4 into account, a concentration of 230 ± 50 ppm was found for the line-pump. The exhaust NO concentration for the common-rail system is slightly higher: 270 ± 60 ppm, which is rather unexpected considering the lower heat release rate (Fig. 2.9), causing lower combustion temperatures and thus less thermally formed NO.

Chapter 3

NO LIF in more detail

3.1 Introduction

In this chapter we will take a closer look at the central measurement technique of the work presented in this thesis: laser-induced fluorescence. It was already briefly discussed in Chapter 1, and further attention will be paid to the pressure and temperature dependence of the fluorescence yield (Section 3.2), and to a number of excitation-detection schemes for NO LIF that have been applied in engine research (Section 3.3).

Quantum mechanics forms the basis of atomic and molecular spectroscopy. Molecular internal energy can, to a first approximation, be attributed to the motion of the electrons and motion of the nuclei, the latter of which can further be divided into vibrational and rotational motion. Since these three processes occur on different time scales, ranging from fast electronic motion to relatively slow nuclear motion, the molecular Hamiltonian can be separated, to good approximation, into electronic, vibrational, and rotational parts. The corresponding energy values can be calculated for each part individually, resulting in electronic energy levels with vibrational “substructure” that is further split into a range of rotational energy levels. This is shown schematically in Fig. 3.1, representing two electronic states with their vibrational and rotational sublevels. The discussion here is limited to diatomic molecules only. Rotational energy levels are characterised by the rotational quantum number J ; for vibrational levels the vibrational quantum number ν is used. In case of a transition, upper state quantum numbers are usually denoted with a prime (e.g. ν' or J'), while a double prime indicates lower levels (ν'' or J''). Electronic energy

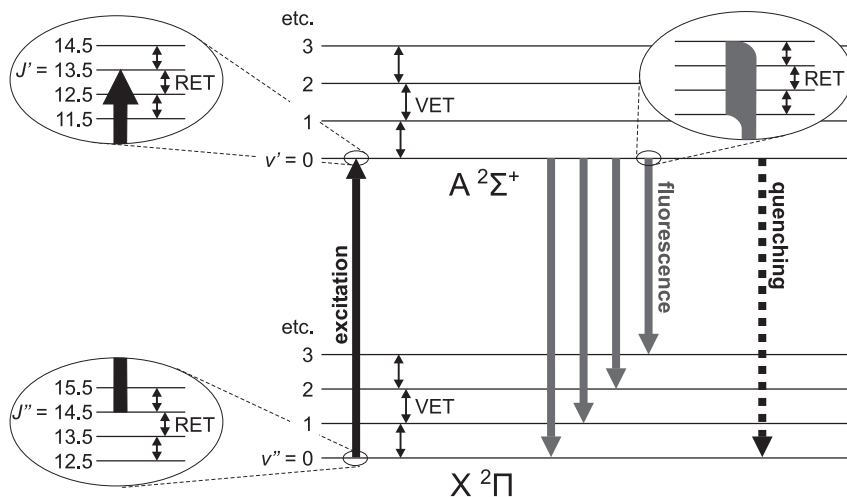


Figure 3.1: Schematic representation of laser-induced fluorescence of NO, including processes like RET, VET, and quenching. (EET is not indicated, since the A -state is the lowest electronically excited state.) The energy level distances are not to scale. The rotational and vibrational quantum numbers (J and v , respectively) are indicated for both electronic states.

states are labelled with upper- and lowercase letters. The ground state or lowest state is always named X , and the subsequent levels with the same total electronic spin S as the X state are named A , B , C , \dots , whereas electronic energy levels with different spin are labelled with lowercase letters a , b , c , \dots .

Upon the absorption of a photon, a molecule makes a transition to a higher energy level (i.e. excitation). This may occur on rotational, vibrational, and/or electronic scale, the corresponding light ranging from microwave, to infrared, to ultraviolet radiation, respectively. In practice, a molecular transition can be a combination of a rotational and a vibrational transition (a “rovibrational” transition), or a combination of rotational, vibrational, and electronic (“rovibronic”) transitions. Rotational transitions are divided into so-called branches: transitions with $\Delta J = J' - J'' = -2, -1, 0, 1, 2$ are called O , P , Q , R , and S branches, respectively. The example in Fig. 3.1 (excitation, indicated by the upward arrow) thus shows a $A^2\Sigma(v'=0) \leftarrow X^2\Pi(v''=0) P(14.5)$ transition.

Typically, molecules in excited electronic states are not stable. They can lose their excess energy by any of three competing processes: (1) decay to a lower energy level by the spontaneous emission of a photon (fluorescence), (2) collisional

energy transfer that may occur on rotational, vibrational, and electronic level (RET, VET, and EET), and (3) collision-induced, non-radiative decay to the electronic ground state, also known as *quenching*. Energy transfer processes may be followed by either fluorescence (at a slightly different wavelength) or quenching. This is illustrated schematically in Fig. 3.1 for the case of RET, leading to fluorescence from multiple J' levels (even though only the $J' = 13.5$ is initially excited) and thus leading to multiple emission lines per “vibronic” transition. In general, VET is relatively slow compared to RET and quenching, and fluorescence from $v' = 1$ is only a marginal contribution to the total emission. Quenching is an important competitor to LIF: especially at elevated pressures (i.e. high collision rates) it causes a substantial decrease in the fluorescence yield. It should be noted that RET also takes place in the ground state, refilling the laser-excited J'' level.

3.2 Processes involved and their p,T dependence

In the case of non-saturated NO LIF there is a linear proportionality between the LIF intensity and the NO number density N_{NO} in the laser probe volume*. In the following, the factors that influence this proportionality are discussed.

Boltzmann fraction The number of molecules in the energy level(s) v'', J'' probed by the laser beam is given by the temperature dependent Boltzmann fraction $f_B(T)$:

$$\begin{aligned} f_B(T) &= f_B^{(\text{vib})} f_B^{(\text{rot})} \\ &= \frac{\exp(-\hbar\omega_e v''/k_B T) (2J''+1) \exp(-B J''(J''+1)/k_B T)}{1 - \exp(-\hbar\omega_e/k_B T) Z_{\text{rot}}}, \end{aligned} \quad (3.1)$$

where k_B is Boltzmann’s constant and $Z_{\text{rot}} \approx k_B T/\sigma B$ the rotational partition function, used for normalisation of the Boltzmann distribution. The symmetry number σ equals 1 or 2 for non-symmetric or symmetric diatomic molecules, respectively. The molecular constants for vibration ω_e and rotation B are accurately known for NO.⁷⁶

*A transition is said to saturate when the fraction of excited molecules is no longer very small compared to the population of the laser-probed energy level. As a consequence, there is no linear relation between the fluorescence intensity and the laser intensity anymore. Note that higher refill rates of the probed energy level (e.g. by RET) extend the linear regime.

Spectral overlap and line broadening The fraction of the molecules in the lower state v'' , J'' that actually absorb a laser photon depends on (1) how well the laser frequency matches the energy of the induced transition and (2) the transition strength. The latter will be discussed in the next paragraph; the former is described by the overlap integral $g(\nu_L, \nu_a)$ of the (normalised) spectral profiles of the laser beam (subscript L) and the NO absorption line (subscript a):

$$g(\nu_L, \nu_a) = \int_{-\infty}^{\infty} g_L(\nu, \nu_L) g_a(\nu, \nu_a) d\nu. \quad (3.2)$$

If Gaussian lineshapes are assumed, and with the laser close to resonance (i.e. $\nu_L \approx \nu_a$), the overlap integral is proportional to

$$g(\nu_L, \nu_a) \propto \frac{1}{\sqrt{\Delta\nu_L^2 + \Delta\nu_a^2}}, \quad (3.3)$$

with $\Delta\nu_L$ and $\Delta\nu_a$ the widths (FWHM) of the laser profile and the absorption line shape, respectively. At higher pressures this approximation is no longer valid since the absorption line will have a Lorentzian shape due to the dominant pressure broadening. In that case, Eq. 3.2 will have to be evaluated numerically.

Although $\Delta\nu_L$ is fixed, $\Delta\nu_a$ changes with pressure and temperature, being affected by Doppler broadening and pressure (or collisional) broadening. In combustion engines, pressure broadening is the dominant contribution to the absorption linewidth (>95% at 3 bar, and >99% at 20 bar). Temperature dependent collisional linewidths of the NO $A-X(0,0)$ system have been measured by Chang et al.,⁷⁷ DiRosa and Hanson,⁷⁸ and Vyrodov et al..⁷⁹ These depend on the collision partner, and are of the form:

$$\Delta\nu_{\text{coll}} = a \left(\frac{295}{T} \right)^b. \quad (3.4)$$

Table 3.1 lists the (experimental) values of a and b for some collision partners. Collision-induced lineshifts have also been observed, but their effect is generally swamped by the increased linewidth. In practice, the laser profile overlaps with a number of absorption lines, and Eqs. 3.3 and 3.1 need to be evaluated for each individual transition. This number increases with increasing pressure, partly compensating the decreasing line overlap.

Transition strength The probability of a molecule (in the lower state v'' , J'') absorbing a laser photon is proportional to the number of photons per unit volume. The molecules are thus excited at a rate:

$$\frac{dN_{v'', J''}}{dt} = B_{12} \rho_\nu N_{v'', J''}, \quad (3.5)$$

Table 3.1: Collisional broadening constants for various collision partners of NO

coll. partner	a (cm ⁻¹)	b	reference
NO	0.551	-	77
H ₂ O	0.79	0.79	78
O ₂	0.53	0.66	78
N ₂	0.58	0.75	77

with N_{ν_j} the number of molecules in respectively the upper and lower states and ρ_ν the spectral energy density of the laser radiation field. The proportionality constant B_{12} is known as the Einstein coefficient for (stimulated) absorption from lower level 1 (or $\nu''J''$) to upper level 2 ($\nu'J'$). It can be shown that the coefficient for *stimulated emission* $B_{21} = B_{12}$ (assuming equal degeneracy for levels 1 and 2). Furthermore, the rate of *spontaneous emission* (i.e. fluorescence), A_{21} , is related to B_{12} by

$$A_{21} = \frac{8\pi h\nu_{21}^3}{c^3} B_{12}. \quad (3.6)$$

Both the excitation rate (via B_{12}) and the fluorescence rate (via A_{21}) determine the intensity of the emitted fluorescence. Since the fluorescence involves transitions from and to many energy levels, one should sum over all relevant A_{ij} coefficients to obtain the total fluorescence rate.

Although A and B are not pressure or temperature dependent, they vary with ν'' and J'' . Since the populations of the probed states depend on temperature, and as the number of levels probed by the laser beam depends on the degree of pressure broadening, this indirectly changes the effective values of A and B .

Spontaneous emission, VET, and quenching As already stated, quenching is a major decay channel as compared to spontaneous emission and VET. Upper state RET does not influence the vibronic band intensities (only the rotational substructure); if the fluorescence is detected at vibrational resolution, which is the case for the experiments in the following chapters, RET can be neglected. Since the A -state is the lowest electronically excited state, EET is not important for $A-X$ excitation. It is, however, for $D-X$ excitation.⁸⁰

Measurements of $\nu' = 1 \rightarrow 0$ VET in the A -state of NO have been reported by Cattolica et al.⁸¹ who found a cross section of $1.8 \pm 0.4 \text{ \AA}^2$ for collisions with H₂O at 1340 K. Thoman et al.⁸² showed cross sections of $0.129 \pm 0.014 \text{ \AA}^2$ and

Table 3.2: Electronic quenching cross sections for several collision partners, $1000 \leq T \leq 3000$ K. *Italic values:* CO and N₂ cross sections also vary with temperature above 1000 K, and an average value is given for $1000 \leq T \leq 2000$ K. Data from Paul et al..^{83,85}

species	quenching cross section σ_i (\AA^2)
CO ₂	55
NO	42
H ₂ O	28
O ₂	26
CO	<i>8.0 (average)</i>
N ₂	<i>0.5 (average)</i>

$0.46 \pm 0.11 \text{ \AA}^2$ with respectively N₂ and NO as collision partners at 1900 K. By the principle of detailed balancing, the corresponding cross sections for $v' = 0 \rightarrow 1$ VET would be 0.14, 0.021, and 0.077 \AA^2 at the respective temperatures of 1340 K and 1900 K.

Electronic collisional quenching rates of the NO A²Σ($v' = 0$) state have been measured and modelled by (a.o.) Paul et al.^{e.g.82–85} for a number of (combustion relevant) collision partners. For most species, quenching cross sections were found to be constant for temperatures above 1000 K. They are listed in Table 3.2. Quenching (or VET) cross sections are related to the quenching (or VET) rate Q by:

$$Q = \sum_i N_i \sqrt{\frac{8 k_B T}{\pi \mu}} \langle\langle \sigma_i(T) \rangle\rangle, \quad (3.7)$$

with N_i the number density of species i and $\langle\langle \sigma_i(T) \rangle\rangle$ its thermally-averaged electronic quenching (or VET) cross section. It is evident that quenching rates are typically 100 times larger than those for VET.

The fraction of excited molecules that fluoresce is given by the *Stern-Vollmer factor*, also known as the *fluorescence quantum yield*. It is defined as the ratio of fluorescence rate to the total decay rate. It is illustrative to compare the quenching rate to the spontaneous emission rate A . Taking $p = 30$ bar and $T = 2000$ K, corresponding to 30° aTDC (see Chapters 5–7), and typical mole fractions from gas sampling experiments,⁸⁶ a quenching rate of $1.9 \times 10^{10} \text{ s}^{-1}$ is obtained. This is much higher than the spontaneous emission rate of $4.6 \times 10^6 \text{ s}^{-1}$, so that the Stern-Vollmer factor $A/(A + Q) \approx A/Q = 2.5 \times 10^{-4}$ for this example.

Total p,T dependence of NO LIF Combining the terms discussed above, one obtains the total expression for the emitted fluorescence intensity I_{LIF} . For convenience, the notation is changed from energy level quantum numbers ν, J to indices denoting the initial lower (i), intermediate upper (j), and final (k) energy states. Upon $i \rightarrow j$ excitation, the fluorescence intensity from state j to k can be written as

$$I_{\text{LIF}}^{(k)} \propto N_{\text{NO}} I_{\text{laser}} f_B g(\nu_L, \nu_{ij}) B_{ij} \frac{A_{jk}}{\sum_l A_{jl} + Q_j}, \quad (3.8)$$

where the summation is over all fluorescent transitions.

Equation 3.8 allows to calculate the NO emission spectrum for any given excitation wavelength, pressure, and temperature. Two numerical models for calculating LIF spectra are widely available, LIFbase⁶³ and LIFSim.⁶⁴ Another model exists, developed by DiRosa⁶² and later extended by Jamette⁸⁷ to include $\nu'' = 1$ and 2 levels as well. It is similar to LIFSim. Unfortunately, LIFbase does not include a quenching model. To date, neither model includes RET, but this is currently under way.⁶⁴ On the other hand, RET becomes important only at high laser intensities (i.e. when saturation may occur) or when rotationally resolved emission spectra are of interest.

3.3 NO LIF excitation-detection schemes

Over the last two decades, a number of excitation strategies for NO LIF in high-pressure combustion applications have been reported. These strategies include $A-X(0,0)$, $A-X(0,1)$, $A-X(0,2)$, and $D-X(0,1)$ excitation around respectively 226, 237, 248, and 193 nm. The relevant potential energy curves (to scale, this time) are shown in Fig. 3.2. The ideal excitation strategy will vary from experiment to experiment. However, each strategy can be evaluated objectively against a number of criteria. These include signal strength (depending on both the transition strength and attenuation effects), the temperature and pressure dependence of the emitted fluorescence, and selectivity against interference from other fluorescent species. Most of these issues have been introduced in the previous section. Interference is the — sometimes unavoidable — excitation of and emission by other species in the same spectral region as the molecule of interest. Molecular oxygen is a good example, its dense $B^3\Sigma_u^- - X^3\Sigma_g^-$ Schumann-Runge system overlapping with many lines in both the $A-X$ and $D-X$ bands of NO. Since the dominant decay channel for excited

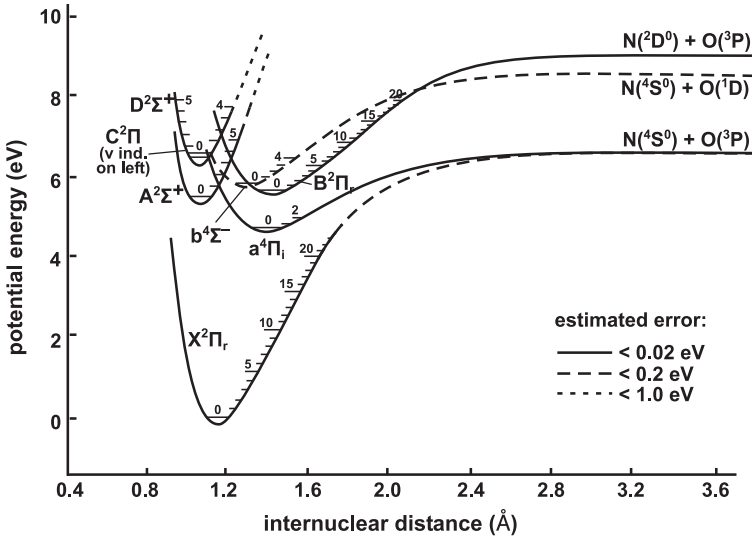


Figure 3.2: Potential energy curves for the seven lowest electronic states of NO, as compiled by F.R. Gilmore.⁸⁸ Vibrational levels are indicated. The Π -states are split by spin-orbit interaction (not visible on the scale of the graph).

O_2 is predissociation* instead of quenching, the O_2 fluorescence intensity is much less dependent on pressure than that of NO. As a result, O_2 interference becomes increasingly important at elevated pressures, and must be carefully minimised for measurements in combustion engines.

The abovementioned excitation strategies for NO will be discussed in the following, with a focus on their application in engine research.

D-X(0,1) excitation First attempts trace back to the early 90's when Andresen et al. used a tunable ArF excimer laser for $D^2\Sigma^+(v' = 0) \leftarrow X^2\Pi(v'' = 1)$ excitation around 193 nm to (qualitatively) image NO in a gasoline engine,⁹ a scheme that was also applied in diesel engines by Arnold et al..⁸⁹ Brugman et al. used 193-nm radiation in an IDI diesel engine² and post-processed the fluorescence distributions for laser beam attenuation and window fouling.³ Stoffels et al. corrected for both the attenuation of the laser beam⁹⁰ and the p,T dependence of the fluorescence yield to arrive at semi-quantitative NO concentrations.⁵ O_2 interference was minimised

*Predissociation occurs when a bound molecular electronic state is crossed by a repulsive one, causing a mixing of the respective wavefunctions near the crossing point. As a consequence, molecules in a stable energy level near the crossing may still dissociate via the repulsive state.

by excitation at 193.377 nm whilst detecting the $D-X(0,4)$ emission band around 216 nm.⁸⁰

At 193 nm, light attenuation was generally so severe that measurements could only be realised at the end of the combustion or even during the exhaust stroke, with the exception of the work by Stoffels.⁵ Unfortunately, little is known about quenching and line broadening of the electronic D state,⁸⁰ which limits a detailed quantitative description of the p, T -dependent photophysics.

A-X(0,0) excitation $A^2\Sigma^+(v' = 0) \leftarrow X^2\Pi(v'' = 0)$ excitation around 226 nm is a popular scheme. Its first application in engine research was reported by Alataş et al.⁹¹ for planar LIF measurements in a diesel engine with oxygen-enriched intake air, later followed by Nakagawa et al.,⁹² and by Bräumer et al. who studied a square-piston SI engine.⁹³ Dec and Canaan employed $A-X(0,0)$ excitation in a heavy-duty diesel engine with both regular diesel and a low-sooting fuel, and accounted for quenching, collisional broadening, and the Boltzmann distribution.⁴ The low-sooting fuel was claimed to cause negligible attenuation. $A-X(0,0)$ excitation was also used by Van den Boom^{7,65} in the same engine that is studied in this work, using realistic diesel fuel. The data were processed for the photophysics of NO, and for laser beam attenuation under the assumption of uniform extinction coefficients. 226-nm radiation is generally provided by a frequency-doubled or mixed dye laser system, although frequency-doubled OPO systems⁴ and even Raman-shifting the radiation from an excimer laser, operating on either ArF⁹⁴ or KrF,⁵¹ have been reported. Although laser beam extinction is still considerable at 226 nm, it is not as severe as for 193 nm. An additional advantage is that with 226 nm the highly populated vibrational ground state is probed, compared to the $v''=1$ state for 193 nm.

Extensive research has been dedicated to quenching,⁸²⁻⁸⁵ and pressure broadening⁷⁷⁻⁷⁹ of the $A^2\Sigma^+(v' = 0) \leftarrow X^2\Pi(v'' = 0)$ transition, which benefits a quantitative interpretation of measurements using $A-X$ excitation.

A-X(0,1) excitation $A-X(0,1)$ excitation is an interesting compromise between laser beam attenuation (which is a problem with (0,0) excitation) and energy level population (and hence signal strength, which is a problem with (0,2) excitation). Jamette et al. investigated the possibilities for $A-X(0,1)$ excitation (and (0,2)+(0,3) detection) of NO and they are to date the only group known to have applied this strategy in an optical, single-cylinder gasoline engine.¹⁴ They accounted for laser beam attenuation by using averaged extinction coefficients (i.e. assuming uniform extinction). Pressure and temperature dependent variations of the LIF intensity

were accounted for, too. In these experiments, considerable laser beam attenuation was still observed. 236-nm radiation was provided by a frequency-doubled optical parametric oscillator (OPO), but can also be produced by a frequency-doubled dye laser system.⁹⁵

A–X(0,2) excitation In order to avoid severe attenuation of the laser beam, Knapp et al. applied A–X(0,2) excitation around 248 nm for qualitative NO imaging in a gasoline engine.¹⁰ They measured the transmission spectrum of broadband UV light passing through the optical cylinder, and concluded that the transmission improved considerably for 248 nm as compared to 226 nm. They also observed that the (blue-shifted) (0,0) and (0,1) emission bands suffer much less from interference by other species. Schulz et al. extended the technique by an extensive analysis of the LIF intensity dependence, allowing quantitative measurements.^{11,96,97} Although corrections for attenuation of the blue-shifted fluorescence are not mentioned, they have been addressed^{98,99} and applied^{13,15} in subsequent papers. The strong in-cylinder UV absorption, increasing for shorter wavelengths, was later attributed to broadband absorption by CO₂ and H₂O^{99,100} (see also item 4 on page 53). Hildenbrand et al. were the first to apply A–X(0,2) excitation for quantitative NO imaging in a DI diesel engine.^{6,8}

A disadvantage of A–X(0,2) excitation is that only hot ($v''=2$) NO is probed, which limits the possibility of measurements late in the combustion cycle, when the combustion products have cooled down. To some extent, this can be compensated by the very powerful KrF excimer lasers used to access this wavelength region. The high power of this light source also makes it a popular tool for two-dimensional imaging using a laser light sheet.

Comparison of schemes A few years ago, Bessler et al. presented an extensive comparative study of A–X excitation schemes, focussing on the selection criteria mentioned above.^{95,101,102} All measurements were conducted in high-pressure flames for various pressures up to 60 bar and at different stoichiometries. After selecting a good (rovibronic) excitation line for A–X(0,0)¹⁰¹ and A–X(0,1)⁹⁵ excitation from a number of candidates, a comparison of (0,0), (0,1), and (0,2) excitation schemes with both blue- and red-shifted detection was reported as well.¹⁰² A–X(0,2) excitation was discussed earlier.^{103,104} Table 3.3 gives some details of the transitions they investigated. Bessler's conclusions can be summarised as follows:

Table 3.3: $A-X$ excitation-detection schemes for NO LIF as compared by Bessler et al.¹⁰² The $A-X(0,0)$ transition at 226.03 nm was also used for the measurements presented in this thesis.

$A-X$ band	combined transitions	λ_{exc} (nm)	detection
(0,0)	$P_1(23.5)$, $Q_1 + P_{21}(14.5)$, and $Q_2 + R_{12}(20.5)$	226.03	(0,1)+(0,2)
(0,1)	$P_1(25.5)$, $R_1 + Q_{21}(11.5)$, and $Q_1 + P_{21}(17.5)$	235.87	(0,0) or (0,2)+(0,3)
(0,2)	$O_{12}(7.5-10.5)$ bandhead	247.94	(0,0)+(0,1) or (0,3)+(0,4)

1. Signal strength: At combustion temperatures (1500-2500 K), the $v'' = 0$ state is the most populated vibrational state. Although the strength and the number of excited rovibronic lines also determine the signal strength, the highest intensities are indeed observed for (0,0) excitation (at 1900 K); they are about three times higher than (0,1) excitation with (0,2)+(0,3) detection and 25 times higher than (0,2) excitation.
2. Interference: The level of O_2 LIF interference is strongly dependent on the excitation wavelength (at rotational resolution), in contrast to the broadband LIF from CO_2 and polycyclic aromatic hydrocarbons (PAHs). It further depends on the spectral width of the detection window. Bessler chose for broadband detection (20-nm window). With spectrographic detection, interferences can be identified and corrected for, whereas with broadband detection the interference contribution to the total signal can only be determined by off-resonance measurements at a comparable interference intensity.^{62,105} This is illustrated in Fig. 3.3, showing the emission spectra of NO and O_2 upon excitation at 226.03 nm. It is clear that O_2 emission around 235, 241, and 271 nm is still spectrally separated from the adjacent NO bands, but separate detection is not possible with broadband optical filters. On the other hand, broadband detection is more suitable for planar LIF imaging.

In lean flames, O_2 LIF is the main interference source, with the least interference for (0,0) excitation and the most for (0,2) excitation. For the latter

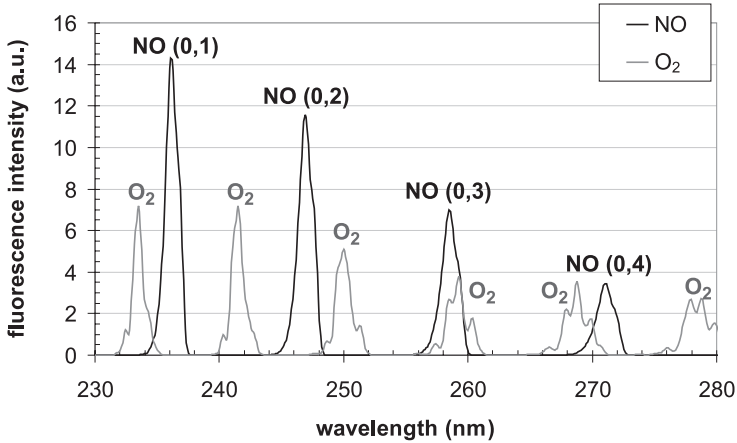


Figure 3.3: Fluorescence spectra from NO and O₂, simulated with LIFSim⁶⁴ for excitation at 226.03 nm at 1000 K and 40 bar. Note that the relative intensities for the NO and O₂ spectra are not to scale.

scheme, O₂ interference is reduced with blue-shifted detection. CO₂ LIF interference behaves similar to O₂. Interference by PAHs occurs in richer flames, but was not studied quantitatively. It was concluded that (0,0) excitation yields the highest signal purities, in both lean and rich conditions ($\Phi = 0.83$ and 1.13, respectively).

3. Temperature dependence: In many practical situations the local temperature is very difficult to obtain. The resulting uncertainty in a quantitative NO concentration measurement can be reduced by selecting a transition that has minimal temperature dependence. Since the fluorescence intensity is proportional to the NO number density (see Eq. 3.8), converting this number to the NO mole fraction x_{NO} involves an additional temperature dependence since $x_{\text{NO}} = N_{\text{NO}}/N_{\text{total}} = N_{\text{NO}} k_B T/p$. Therefore, the overall temperature sensitivity depends on whether the data are interpreted in terms of mole fractions or number densities. Based on spectral simulations, Bessler predicted the temperature dependence for the abovementioned excitation strategies. In terms of number densities, (0,0) excitation yields relatively temperature independent LIF signals, varying by 7% between 1700 and 2500 K at 10 bar, compared to 18% and 36% for respectively (0,1) and (0,2). In terms of mole fractions, (0,1) excitation was found the best candidate, with variations of only 3% against 25% for (0,0) and 19% for (0,2) excitation.

4. Wavelength dependent attenuation: Hot CO_2 and H_2O may cause considerable attenuation in the UV, especially at combustion temperatures and at wavelengths below 250 nm for CO_2 and 230 nm for H_2O . Both feature smooth, broadband absorption spectra, the absorption increasing with increasing temperature and with decreasing wavelength. Because of the strong wavelength dependence, the effective attenuation varies from one NO LIF strategy to the other. Additionally, it depends on the experimental geometry and conditions. For instance, relatively long laser path lengths shift the balance in favour of (0,2) excitation (with blue-shifted detection to reduce interference), whereas (0,0) and (0,1) excitation (and red-shifted detection) are advantageous if the fluorescence travels the longer distance. Besides, the influence of CO_2 and H_2O absorption becomes more pronounced at higher temperatures.

As a conclusion, $A-X(0,0)$ excitation offers many advantages in terms of signal strength and purity, and small temperature dependence. Concerning the wavelength dependent UV absorption by CO_2 and H_2O , $A-X(0,0)$ excitation together with red-shifted detection is advantageous for experiments with a relatively short path length for the laser beam and a longer one for the fluorescence. This issue is further discussed in Chapter 5.6.

3.4 Calibration

We have seen that the fluorescence intensity is proportional to the NO number density (Eq. 3.8). The proportionality constant itself is not always straightforward to obtain accurately, as it depends on the (spectral) sensitivity of the detector, the collection angle, and transmission properties of further optics (lenses, mirrors). Instead, it is often preferred to calibrate the system by a reference measurement.

Calibration of the optical setup can be realised by adding (“seeding”) NO to the intake gases, and is often applied in (high pressure) flames,^{104,105} and also in a gasoline engine.¹¹ This method is, however, limited to lean combustion, as the seeded NO may reburn under fuel-rich conditions.¹⁰⁶ This makes it unreliable for application in diesel engines, where the stoichiometry varies from (globally) lean to (locally) rich.²⁹ In that case, the optical setup can be calibrated with a lean methane-air flame, doped with different amounts of NO, positioned inside or close to the measurement cylinder.^{8,15}

Alternatively, the semi-quantitative in-cylinder concentration history based on LIF can be scaled such that its value at the end of the combustion stroke matches

the NO concentration in the exhaust. The latter can be measured relatively easily and accurately by means of a commercially available exhaust gas analyser. This technique was used by Jamette et al.,¹⁴ and was also applied in this work (see Chapters 2.5, 6, and 7). This approach requires that the concentration in the probe volume is representative for the global concentration measured in the exhaust.

Chapter 4

Absorption of NO LIF by hot O_2 and CO_2^*

4.1 Introduction

Laser-induced fluorescence (LIF) is frequently used as a diagnostic tool in combustion research, offering high spatial and temporal resolution, high species selectivity, and low intrusion. In many cases, absorption of laser light and/or fluorescence needs to be corrected for. UV-LIF measurements of nitric oxide (NO) can be significantly affected by CO_2 absorption;^{99,100} additional absorption can be caused by aromatic fuel compounds, soot, and — especially at high temperatures — O_2 . In this chapter, a (simplified) parameterisation of the UV absorption spectrum of O_2 will be presented. Furthermore, the effect of O_2 and CO_2 absorption on NO LIF measurements in a diesel engine will be demonstrated.

4.2 O_2 absorption spectra

Figure 4.1a shows O_2 absorption cross sections for a number of temperatures, simulated with LIFSim.⁶⁴ Unlike the smooth, structure-less CO_2 absorption spectrum (Fig. 4.1b),¹⁰⁰ the O_2 spectrum consists of many closely-spaced rovibronic lines, belonging to the Schumann-Runge ($B^3\Sigma_u^- - X^3\Sigma_g^-$) system that extends from 175 to 535 nm.¹⁰⁷ The actual absorption of an NO (vibronic) fluorescence band depends

*Adapted from: K. Verbiezen, A. P. van Vliet, W. L. Meerts, N. J. Dam, and J. J. ter Meulen, *Combustion and Flame* 144, 638 – 641 (2006)

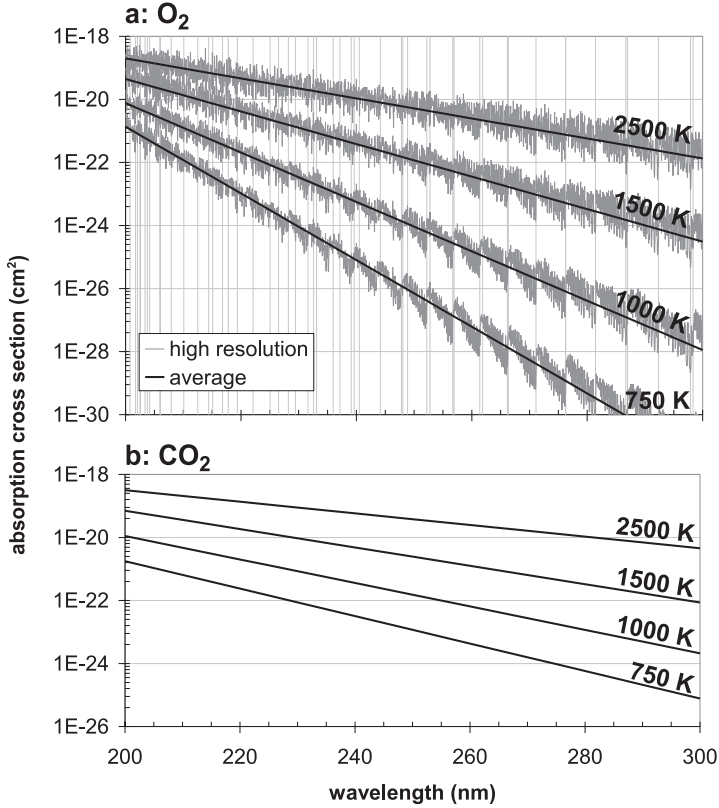


Figure 4.1: Simulated O₂ (a) and CO₂ (b) absorption cross section vs. wavelength, based on Refs. 64 and 100, respectively. The straight lines in panel a are fits using Eqs. 4.1 – 4.3. Vertical gridlines indicate the band origins, values from Krupenie.¹⁰⁷

on the intensities and relative positions of NO emission and O₂ absorption lines. As this is a numerically expensive calculation for a fitting procedure, we approximate the O₂ absorption cross section by a simplified curve analogous to the CO₂ absorption function.¹⁰⁰ This expression was fitted to simulated absorption spectra (LIFSim⁶⁴) over a range of temperatures (500 < T < 3000 K) and wavelengths (200 < λ < 300 nm), yielding:

$$\bar{\sigma}_{\text{O}_2} = \exp(a + b \lambda) \quad (4.1)$$

$$a = -45.25 + 1.34 T + \frac{33.66}{T} \quad (4.2)$$

$$b = 1.916 - 0.593 T - \frac{19.36}{T}, \quad (4.3)$$

with σ in cm^2 , λ in units of 100 nm, and T in units of 1000 K. Equation 4.1 represents an average O_2 absorption cross section; some curves are shown in Fig. 4.1. At high pressures, the strong variations in O_2 transmission are (to some extent) averaged out by the broad NO emission bands. Although $\exp(-nL\bar{\sigma}_{\text{O}_2}) \neq \overline{\exp(-nL\sigma_{\text{O}_2})}$, which may cause significant errors for large O_2 column densities, in our experiments Eq. 4.1 leads to acceptable deviations of $\sim 5\%$ for the transmission of the detected NO fluorescence (see below) as compared to high-resolution calculations.

Although the O_2 absorption cross section is smaller than that for CO_2 , the higher number density of O_2 may compensate for this. For both CO_2 and O_2 , the (average) absorption increases with increasing temperature and with decreasing wavelength.

4.3 Experiment

NO fluorescence was induced by a 226.035 nm laser beam directed into the measurement cylinder of a diesel engine (60 mg fuel injected, gIMEP of around 500 kPa); an iCCD camera-spectrograph system recorded the $A \rightarrow X(0,1)-(0,4)$ vibronic fluorescence bands of NO. Rotational structure is not resolved. The probe volume is 37 mm away from the detection window. Further details can be found in Refs. 7, 108, 109, or Chapters 5 and 6 in this thesis.

The relative intensities of the NO fluorescence bands are governed by (constant) Franck-Condon factors*; any observed deviations from these intensity ratios are attributed to wavelength-dependent absorption of the fluorescence. Some measured spectra are shown in Fig. 4.2, clearly showing varying relative intensities during the stroke. Transmission spectra are obtained after dividing the fluorescence by a reference spectrum (recorded at the end of the combustion stroke, 130° aTDC, when temperatures of ~ 800 K are too low to cause significant CO_2 and O_2 absorption), and normalising these ratios at 271 nm. By taking ratios, wavelength-dependent detector response is automatically corrected for. Subsequently, these spectra are fitted by simulated O_2 and CO_2 transmission spectra (also normalised at 271 nm). Additional, wavelength-independent absorption (e.g. by soot) cannot be measured with this technique, being (almost) equal for all NO fluorescence wavelengths. In order to limit the number of free parameters, the O_2 number density was not treated as a variable, but instead calculated from Raman scattering by O_2 and N_2 ¹¹⁰ (Fig. 4.3),

*Fluorescence from the $A^2\Sigma(v' = 1)$ state, which is populated by $v' = 0 \rightarrow v' = 1$ VET, cannot be separated from $v' = 0$ fluorescence by our setup. However, VET rates are low compared to other competing processes like quenching, and the $v' = 1$ fluorescence is 100 times weaker than that from the $v' = 0$ state (see also Chapter 3.2).

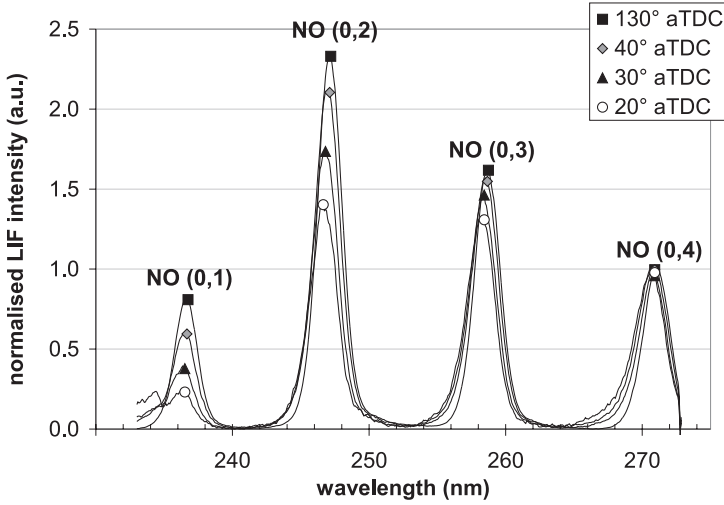


Figure 4.2: NO emission spectra (15-shot averages) at various crank angles, all normalised at 271 nm. The spectrum at 130° aTDC is used as a reference spectrum (see text).

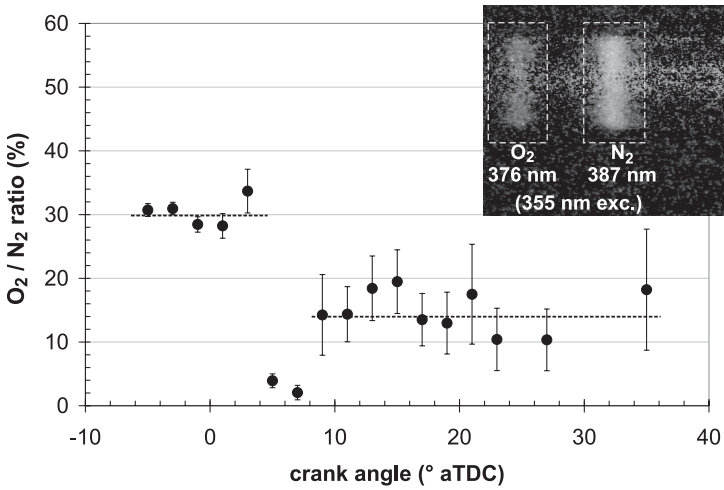


Figure 4.3: The local O₂/N₂ ratio, obtained from Raman scattering experiments (upper right corner). All data shown are 20-shot averages.

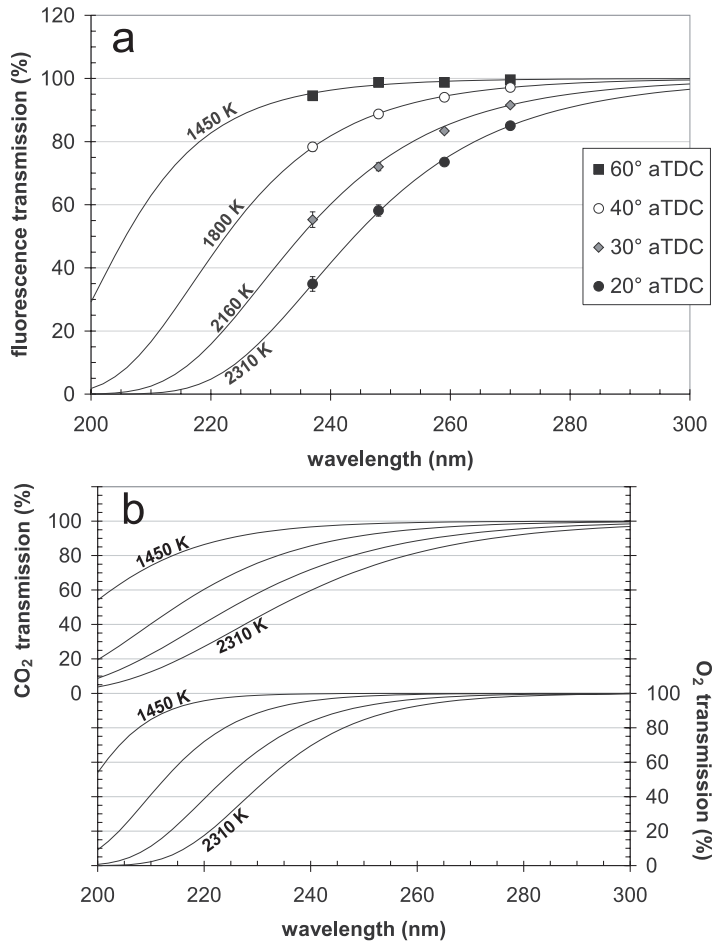


Figure 4.4: (a): fitted transmission spectra, based on absorption by CO₂ and O₂. (b): the same transmission spectra, split into the individual contributions by CO₂ and O₂.

revealing that only $(50 \pm 10)\%$ of the O₂ in the probe volume is consumed. The remaining parameters, CO₂ density and temperature, follow from the fit.

4.4 Results and discussion

Figure 4.4a displays the transmission of four NO fluorescence bands for a number of crank angles, together with fitted O₂ and CO₂ transmission spectra. In Fig. 4.4b

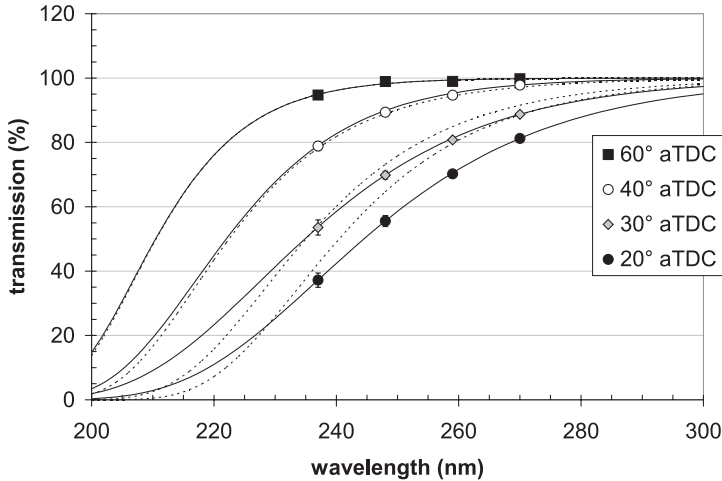


Figure 4.5: Same as Fig. 4.4, but now taking only CO₂ into account as an absorber. Symbols represent (rescaled) data, solid lines are fitted spectra. The fitted spectra from Fig. 4.4a, are added as dashed lines for comparison.

these fits are split into contributions by CO₂ and O₂. It is clear that O₂ causes considerable UV absorption, especially at shorter wavelengths and at lower crank angles (i.e. higher temperatures) when O₂ and CO₂ contribute almost equally to the total absorption. Although O₂ absorption has a more pronounced temperature and wavelength dependence, the general shape of the CO₂ and O₂ absorption spectra is similar. Misleadingly, the data in Fig. 4.2 can be fitted equally well with only CO₂ as an absorber (see Fig. 4.5), but this leads to an overestimation of the CO₂ density by typically 60% for the experiments shown here. Apparently, this ambiguity can only be resolved with independent measurements of either O₂ or CO₂ densities.

Acknowledgements

We thank C. Schulz for the elucidating discussions. This research is supported by the Technology Foundation STW, applied science division of NWO and the technology programme of the Dutch Ministry of Economic Affairs.

Chapter 5

Attenuation corrections for in-cylinder NO LIF measurements in a heavy-duty diesel engine*

Abstract

Quantification of the nitric oxide (NO) concentration inside the cylinder of a diesel engine by means of laser-induced fluorescence (LIF) measurements requires, amongst others, knowledge of the attenuation of the ultraviolet radiation involved. We present a number of laser diagnostic techniques to assess this attenuation, enabling a correction for laser intensity and detection efficiency of the raw NO LIF data. Methods discussed include overall laser beam transmission, bidirectional laser scattering (bidirectional LIF), spectrally resolved fluorescence imaging, and Raman scattering by N₂. Combination of techniques is necessary to obtain the complete attenuation of laser beam and NO fluorescence. The overall laser beam transmission measurements and bidirectional LIF measurements (the latter yielding spatially resolved transmission) provide evidence of a non-uniform attenuation distribution, with predominant attenuation within or near the piston bowl. Fluorescence imag-

*Adapted from: K. Verbiezen, R.J.H. Klein-Douwel, A.P. van Vliet, A.J. Donkerbroek, W.L. Meerts, N.J. Dam, and J.J. ter Meulen, *Applied Physics B* 83, 155 – 166 (2006)

ing of multiple vibrational bands through a spectrograph is shown to be a powerful method for obtaining spatially resolved data on the transmission losses of fluorescence. Special attention is paid to the role of CO_2 and O_2 as UV light absorbers, and the consequences to different excitation-detection schemes for NO.

5.1 Introduction

In order to improve the exhaust emissions of oxides of nitrogen (NO_x) from diesel engines, it is of great importance to study the formation processes involved. The laser-induced fluorescence (LIF) technique has been widely employed for in-cylinder visualisation of nitric oxide (NO) in diesel engines^{3–8} and SI engines,^{9–15} offering robust and non-intrusive diagnostics, high spatial and temporal resolution, and species selectivity, even under extreme combustion conditions of high pressures and temperatures.

This work focusses on in-cylinder NO LIF measurements in a diesel engine by $A \leftarrow X(0,0)$ excitation at 226 nm and detecting the fluorescence bands around 237, 248, 259, and 271 nm. Absolute NO densities can be obtained from the raw LIF intensity, after processing the data for several effects, among which temperature and pressure dependence of the excitation efficiency, collisional quenching, and overlap of the excitation line with the spectral profile of the laser. Interference by O_2 LIF must carefully be investigated as well. All these issues have been extensively studied (see e.g. Refs. 7, 101, 102, 111, 112).

More elusive, but equally important, are the necessary corrections for non-uniform excitation laser intensity and fluorescence attenuation. Previous in-cylinder measurements of NO, conducted in our engine, suggest that both the laser beam and the induced NO fluorescence are strongly attenuated by the cylinder contents during a large fraction of the combustion stroke.^{7,110} Such attenuation is usually attributed to absorption and scattering by fuel (droplets and/or vapour),^{113–116} soot particles,^{4,117} absorption by aromatic fuel compounds,^{118,119} and absorption by combustion products such as CO_2 and H_2O .^{100,120} In addition, the numerous and closely-spaced vibronic transitions of the Schumann-Runge system of O_2 cause UV absorption that may become significant at combustion temperatures.¹²¹ Since the spatial distribution of all these agents is mostly unknown, it is difficult to predict the in-cylinder attenuation of the laser beam and the NO fluorescence.

In this chapter, a number of experimental techniques are presented to quantitatively assess this attenuation, focussing on: (1) the *local* attenuation of the laser

method	provides information on...	combination
CO ₂ and O ₂ absorption spectroscopy	fluorescence attenuation (by CO ₂ and O ₂ only)	1 and 2
bidirectional laser scattering	local laser beam attenuation	1
N ₂ Raman scattering	soot-based attenuation of laser beam and fluorescence	2

Table 5.1: Measurement techniques for attenuation corrections of laser-induced fluorescence.

beam, (2) the attenuation of the fluorescence on its way to the detection window, and (3) losses due to soiled windows. Each technique assesses one or more of these items, as is illustrated in Table 5.1. They will be introduced in the next section. Generally, *combinations* of techniques are needed for a complete picture of all attenuation factors; the three techniques in Table 5.1 constitute two combinations that assess the total attenuation. Quantitative in-cylinder NO measurements, based on the attenuation corrections discussed here, will be presented elsewhere¹⁰⁹ (chapter 6).

5.2 Laser diagnostics

5.2.1 Fluorescence attenuation: absorption by hot CO₂ and O₂

Since the laser probe volume is a distance $d = 37$ mm away from the detection window, the induced NO fluorescence can be significantly attenuated before it reaches the detector. A major part of this fluorescence attenuation turns out to be caused by absorption by CO₂ and O₂. Schulz et al. have demonstrated that CO₂ and, to a lesser extent, H₂O are potential UV absorbers ($\lambda \leq 300$ nm) at combustion temperatures ($T \geq 1000$ K).¹⁰⁰ Both species feature broad-band absorption in the wavelength range of NO LIF, the cross section increasing with decreasing wavelengths, and with increasing temperature. It can be parameterised by a function of the form¹⁰⁰

$$\sigma_{\text{CO}_2} = \exp[a(T) + b(T)\lambda]. \quad (5.1)$$

In most practical cases, the H₂O absorption cross section is at least one order of magnitude smaller than that of CO₂.¹²⁰ Since UV absorption by H₂O is generally negligible in combustion engines,⁹⁹ it is not taken into account here.

In addition to CO₂, O₂ can lead to significant attenuation,¹²¹ especially at high temperatures. The many closely-spaced absorption lines in the O₂ transmission spectrum are (to some extent) averaged by the spectrally broader emission bands of NO. As a result, the O₂ absorption cross section can be *approximated* by a smooth absorption function, similar to Eq. 5.1. This approximation is by no means valid in general, but in our experiments it leads to deviations of < 5% compared to detailed calculations based on simulated high-resolution O₂ absorption and NO emission spectra.

Detection of NO LIF through a spectrograph gives the opportunity to simultaneously measure the intensities of a number of vibronic bands. The relative intensities of these bands are governed by Franck-Condon factors and spectral efficiency of the detection system, and are therefore constant. Thus, any deviations of the observed LIF spectrum from the theoretical spectrum are caused by wavelength-dependent absorption of the fluorescence. A discrete transmission spectrum can be obtained by dividing the observed (relative) LIF peak intensities by their theoretical values, as was demonstrated by Hildenbrand and Schulz (albeit with O₂ LIF instead of NO LIF).⁹⁹ Subsequently, the transmission spectrum of CO₂ and O₂ can be fitted to this spectrum, using the temperature dependent absorption cross sections from Refs. 100 and 121, respectively (NO self absorption is negligible; < 5% for the band at 237 nm and less for the others). This fit yields both the effective fluorescence absorption by CO₂ and O₂, as well as an effective temperature of the absorbing volume.

Unfortunately, this method only yields the wavelength dependent attenuation of the NO fluorescence; attenuation by soot (which can be significant but has only a very weak wavelength dependence compared to the molecular absorbers) cannot be retrieved. It can be measured with Raman scattering by N₂, however, as will be presented in Section 5.2.3.

5.2.2 Laser beam attenuation: bidirectional LIF

Although it is straightforward to measure the transmission of the laser beam over its entire traversal of the measurement cylinder (and thus the *average* extinction), this is a line-of-sight measurement and spatial information (along the laser beam) is lacking. Spatially resolved laser beam transmission measurements can be realised with a technique called bidirectional laser scattering,^{90, 114, 122, 123} involving two laser pulses traversing the same trajectory through the cylinder (quasi) simultaneously, but in opposite directions (see Fig. 5.1). Both pulses will be scattered by the same

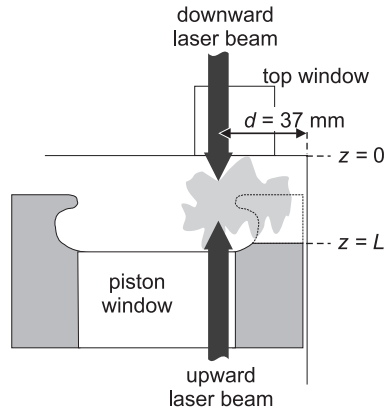


Figure 5.1: Geometry of bidirectional laser scattering in the measurement cylinder (vertical cross section). The laser beams propagate along the vertical axis z . The slot on the right of the piston bowl ensures optical access throughout the cycle.

medium but have a different “history” in terms of integrated extinction. The (in-) elastically scattered light from each laser pulse is recorded separately on a CCD camera. From the two intensity profiles, the local extinction coefficient can be reconstructed. Stoffels et al.⁹⁰ applied this technique to correct for laser beam extinction in a diesel engine. Corrections for laser beam extinction in fuel sprays have also been reported.^{113–115}

In this work, spatial profiles of NO fluorescence were measured for both laser beam propagation directions (i.e. top-down and bottom-up). The analysis is slightly different to that by Stoffels et al., in order to handle the strong noise amplification that is inherent to this technique.^{90,114}

In general, the detected NO LIF signal $S(z)$ can be written as:

$$S(z) = C A(z) n_{\text{NO}}(z) \sigma_{\text{NO}}(z) I_{\text{laser}}(z), \quad (5.2)$$

in which z is the location within the combustion chamber, measured from the top of the detection window, as is indicated in Fig. 5.1. C is a proportionality constant accounting for e.g. detection efficiency, $A(z)$ the collection efficiency (including fluorescence transmission on its way to the detector), n_{NO} the NO number density, σ_{NO} the NO fluorescence cross section, and $I_{\text{laser}}(z)$ the local laser intensity. For clarity the temperature and pressure dependence of σ_{NO} are not written explicitly.

The intensities of the downward and upward laser beams I_{down} and I_{up} are given

by:

$$I_{\text{down}}(z) = I_{\text{down}}(0) \exp \left\{ - \int_0^z \alpha(z') dz' \right\}, \quad (5.3)$$

and

$$I_{\text{up}}(z) = I_{\text{up}}(L) \exp \left\{ - \int_z^L \alpha(z') dz' \right\}, \quad (5.4)$$

where $I_{\text{down}}(0)$ is the intensity of the downward laser beam before it enters the cylinder, $I_{\text{up}}(L)$ is the intensity of the upward laser beam at the bottom of the field of view (i.e. at $z = L$; L increases with increasing crank angle until the detection window is no longer partially blocked by the piston, see Fig. 5.1), and $\alpha(z)$ is the effective local extinction coefficient encountered by both laser beams.

Combining Eqs. 5.2, 5.3, and 5.4, we see that in the quotient of S_{up} and S_{down} the NO densities and $A(z)$ cancel, and the laser beam attenuation is left as the only z -dependent term:

$$\begin{aligned} \frac{S_{\text{down}}(z)}{S_{\text{up}}(z)} &= \frac{C_{\text{down}} I_{\text{down}}(0)}{C_{\text{up}} I_{\text{up}}(L)} \\ &\times \exp \left\{ -2 \int_0^z \alpha(z') dz' + \int_0^L \alpha(z') dz' \right\}. \end{aligned} \quad (5.5)$$

This can be rewritten to express the local attenuation coefficient in terms of S_{up} and S_{down} :

$$\alpha(z) = -\frac{1}{2} \frac{d}{dz} \ln \left[\frac{S_{\text{down}}(z)}{S_{\text{up}}(z)} \right], \quad (5.6)$$

which is identical to the equation presented by Stoffels et al.,⁹⁰ and may be used to directly calculate the laser beam transmission along the beam path. Unfortunately, the mathematical operations in Eq. 5.6 cause severe noise amplification, which limits its use to cases with very good signal-to-noise ratios. Therefore, we return to Eq. 5.5 and note that the square root of $S_{\text{down}}/S_{\text{up}}$ is proportional to the integrated laser beam extinction:

$$S_q(z) \equiv \sqrt{\frac{S_{\text{down}}(z)}{S_{\text{up}}(z)}} \propto \exp \left\{ - \int_0^z \alpha(z') dz' \right\}. \quad (5.7)$$

In practice, S_q is a gradually varying function of the location z . Rather than taking the logarithm and derivative, the function

$$f(z) = p_1 \exp \left\{ -(p_2 z + p_3 z^2 + p_4 z^3) \right\}, \quad (5.8)$$

is fitted to S_q , immediately yielding the local laser beam transmission after setting parameter p_1 equal to 100%. A third degree polynomial fits our data within the uncertainty of the observed laser beam transmission profiles; for this reason no higher degrees were included.

5.2.3 Combined laser beam and fluorescence attenuation: N_2 Raman scattering

Similar to NO LIF, the intensity of the Raman-scattered light by N_2 is not only proportional to the N_2 density, but is also affected by attenuation of both the laser beam and the Raman-scattered light. Since the amount of N_2 is constant during the combustion, and density variations due to temperature inhomogeneities can be estimated (e.g. using the temperature obtained from the fitted UV absorption spectra, see previous section), the variation of the N_2 Raman scattering intensity is a direct measure of the relative attenuation by the cylinder contents. This attenuation includes both laser beam and fluorescence attenuation. The relatively low Raman scattering efficiency can be compensated by high laser intensities and — especially early in the stroke — the high N_2 density, yielding good signal-to-noise levels.

If the Raman wavelengths are beyond the CO_2 and O_2 absorption range (as is the case here), the derived transmission mainly reflects soot-based attenuation. In order to extrapolate to NO LIF wavelengths, the additional absorption by CO_2 and O_2 (as discussed in Section 5.2.1) needs to be included. Additionally, the marginal wavelength dependence of scattering and absorption properties of soot particles may need to be taken into account as well (see Appendix I). Finally, the Raman scattering cross section varies up to 30% over the temperature range of interest here,⁴⁹ which needs to be accounted for.

5.2.4 Losses caused by window fouling

After each fuel injection, some of the in-cylinder soot will deposit on the windows. Fouling of the entrance window for the laser beam and of the detection window will cause the (detected) fluorescence intensity to decrease during a measurement session. The average effect of window fouling can be derived by monitoring the LIF intensity at a certain (fixed) crank angle as a function of the number of fuel injections. Except for random variations due to cycle-to-cycle fluctuations, the generally decreasing trend can be attributed to increasing window opacity.

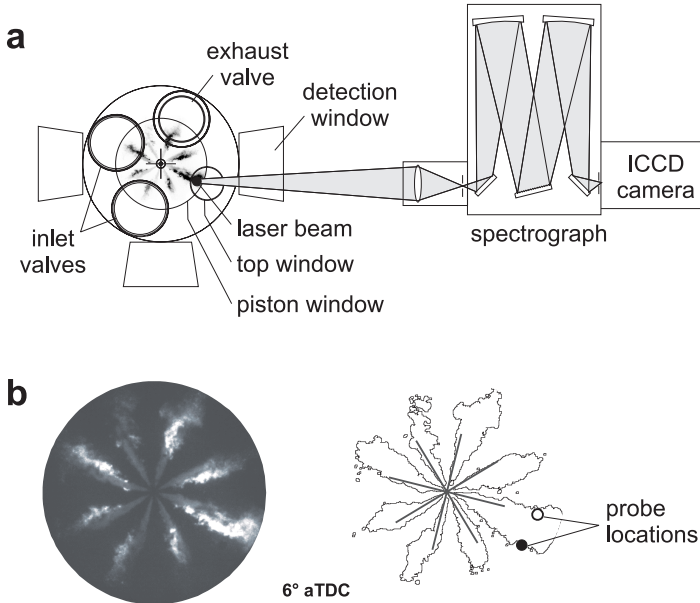


Figure 5.2: (a) Schematic representation of the setup (top view). The laser beam propagation is out of plane, nearly parallel to the cylinder axis, either top-down or — for the bidirectional measurements — bottom-up. NO fluorescence is detected by an imaging grating spectrograph through the nearest side window. (b) 100 ns snapshot of the combusting fuel sprays (left), together with a contour plot (right) of the same image, indicating the two laser probe positions and the spray axes (solid grey lines). Circle: “through spray”; dot: “between sprays”).

5.3 Experiment

5.3.1 The engine

All measurements have been performed on a heavy-duty, six-cylinder truck engine (DAF 1160 series block, cylinder head WS268L). One cylinder is fitted with the cylinder head of the modern DAF 95XF type engine and is used for in situ measurements. Apart from changes providing optical access, it has been kept as realistic as possible. Five quartz windows are mounted in the cylinder, see Figs. 5.1 and 5.2. One of the exhaust valves was replaced by a cylindrical window, referred to as the top window. Additionally, there are three $48 \times 23 \text{ mm}^2$ windows in the cylinder wall (“side windows”), giving a view of the uppermost part of the combustion chamber. Finally, a 70 mm diameter window in the piston (flat surfaces to prevent image

distortion) enables an upward view into almost the complete chamber. An example image of the combusting sprays, as seen through the piston window, is shown in Fig. 5.2 b. The cam-driven, eight-hole fuel injector is mounted in the centre of the cylinder head. It can be rotated, allowing measurements at different positions relative to the fuel sprays without repositioning the laser beam. In this work, the laser probe volume is 35 mm downstream of the fuel injector, either along the fuel spray path (“through spray”), or with the injector rotated by 22.5° (“between sprays”).

A slot machined into the piston crown provides optical access through one of the side windows even at Top Dead Centre (TDC). Because of this slot and the flat windows in the cylinder wall and in the piston, the compression ratio is reduced from 16 to 15. The resulting lower TDC temperature is partly compensated by preheating the inlet air. No lubricants are used since they would absorb the UV (laser) radiation and contribute to soot formation; to avoid overheating the measurement cylinder is skip-fired (1:35). Steady-state conditions are mimicked by (pre-) heating the cooling water to operational temperatures.

All measurements presented here were conducted at an engine speed of 1430 rpm and 25% load. The latter corresponds to injection of 60 mg of low-sulfur diesel between 5° before TDC (bTDC) and 6° after TDC (aTDC), with a boost pressure of 130 kPa (absolute). With these settings, a TDC temperature of 688 K, and a gross Indicated Mean Effective Pressure (gIMEP) of around 500 kPa were calculated from the cylinder pressure data.²⁹

5.3.2 NO LIF measurements

NO is detected by means of laser-induced fluorescence (LIF), exciting the molecules from the electronic ground state $X^2\Pi(v'' = 0)$ to the $A^2\Sigma(v' = 0)$ state. The coinciding $P_1(23.5)$, $Q_1 + P_{21}(14.5)$, and $Q_2 + R_{12}(20.5)$ transitions are induced by laser radiation at 226.035 nm. This excitation wavelength was suggested by DiRosa et al. for its high sensitivity and minimal O_2 LIF interference even at elevated pressures.⁶²

Laser radiation is produced by either a frequency-doubled dye laser (Lambda Physik ScanMate 3 using Coumarin 47) pumped by a Nd:YAG laser (Continuum PowerLite 9010), or a frequency-mixed dye laser (Radiant Narrowscan D, using Rhodamin 101) pumped by a Nd:YAG laser (Continuum Powerlite Precision II 8010). The unfocused laser beam (4 mm diameter) of circa 2.5–5 mJ/pulse traverses the combustion chamber nearly parallel to the cylinder axis, entering through the top window, and leaving it through the piston window (see Figs. 5.1 and 5.2). For the

bidirectional LIF experiments, measurements were also performed with a reversed laser beam direction.

Laser-induced fluorescence is detected through a side window closest to the probe volume by an intensified CCD camera (Roper Scientific, ICCD 512T, 512^2 pixels, 16 bits) mounted behind a spectrograph (ARC SpectraPro 500i, 600 grooves/mm) that is equipped with a Nikkor UV 105 mm objective. The spectrograph allows spatially and spectrally resolved simultaneous detection of the $A \rightarrow X(0,1)$, $(0,2)$, $(0,3)$, and $(0,4)$ fluorescence bands around respectively 237, 248, 259, and 271 nm. Its entrance slit is parallel to the laser beam and fully open (3 mm) to maximise signal strength. The probe volume is determined by the diameter of the incident laser beam (4 mm), and the height of the side window (23 mm), or, early in the stroke, by the slot in the piston crown. Since the laser beam immediately enters the field of view, the effect of laser beam extinction is minimised. The in-cylinder fluorescence path length is 37 mm. Background combustion luminosity is reduced by short camera gating (~ 60 ns).

5.3.3 Transmission measurements

During the NO LIF measurements, the transmission of the laser beam over its trajectory through the cylinder is recorded simultaneously. After exiting the cylinder through the piston window, the laser beam is deflected by a 45° dichroic mirror onto a quartz diffuser plate where it is scattered and detected by a second intensified CCD camera (Roper Scientific ICCD 512T; 16 bits, 512^2 pixels, Nikkor UV 105 mm objective). Background combustion light is suppressed by the dichroic 45° mirror; any remainder is smeared out by the diffuser plate and contributes to a uniform background. This background is eliminated by fitting a Gaussian curve through a cross section of the laser spot, yielding not only the transmitted laser intensity (the area under the curve), but also information on beam steering and divergence.

The gradually increasing effect of window fouling during a measurement session is excluded by normalising the transmission at each crank angle by a reference measurement at the same crank angle during a previous, non-fired cycle. Here it is assumed that soot deposition is a gradual process, without dramatic changes between individual cycles. Musculus et al. give an extensive discussion of laser-extinction-based measurements of fuel jet soot and window soot in a diesel engine.⁷³

5.3.4 O₂ LIF measurements

The experimental configuration for the O₂ LIF measurements is identical to the one used for NO LIF, except the laser radiation being provided by a tunable pulsed ArF excimer laser (Lambda-Physik, Compex 350T). Fluorescence of O₂ was induced by laser radiation at 193.221 nm, corresponding to the combined $P_1+P_2+P_3(15)$ and $R_2+R_3(17)$ lines in the $B^3\Sigma_u^+(v'=10) \leftarrow X^3\Sigma_g^-(v''=2)$ transition in the Schumann-Runge system. Since the O₂ excitation spectrum contains many, closely-spaced, lines involving transitions to and from various vibrational energy levels,¹⁰⁷ emission spectra from more than one vibrational state cannot be avoided. This transition was chosen because it is relatively strong, and because 193.221 nm is minimally absorbed by cold oxygen in the ambient air (the laser beam travels over 5 m before it reaches the measurement cylinder). The spectrograph was set to detect O₂ fluorescence bands around 225, 233, 240, 248, 255, and 265 nm, corresponding to the $v' = 10 \rightarrow v'' = 7 - 12$ transitions respectively.

5.3.5 N₂ Raman scattering measurements

Raman measurements have been performed in a setup similar to that for NO LIF detection, using the unfocused 355 nm radiation of a frequency-tripled Nd:YAG laser (Spectron Lasers, SL 8354 YDA) at about 210 mJ pulse energy, and an ARC SpectraPro 300i spectrograph with a 1200 grooves/mm grating. The grating was oriented such that Raman scattering by O₂ (376 nm) and N₂ (387 nm) could be observed simultaneously.

5.4 Results and discussion

5.4.1 Transmission measurements

Figure 5.3 shows averaged laser beam transmission curves at 226 nm for the two probe locations. Early in the stroke, the laser beam transmission decreases drastically to approximately 1% for both locations. The earlier decrease for the “through spray” position may be explained by the fuel spray hitting the laser beam between 1° and (at least) 7° aTDC, as confirmed by shadowgraphy experiments (top of Fig. 5.3).

At the “between sprays” position, the transmission decreases shortly after the start of combustion, as can be seen from the pressure rise around 3° aTDC (the first combustion spots are visible through the piston window at 3° aTDC). Likely

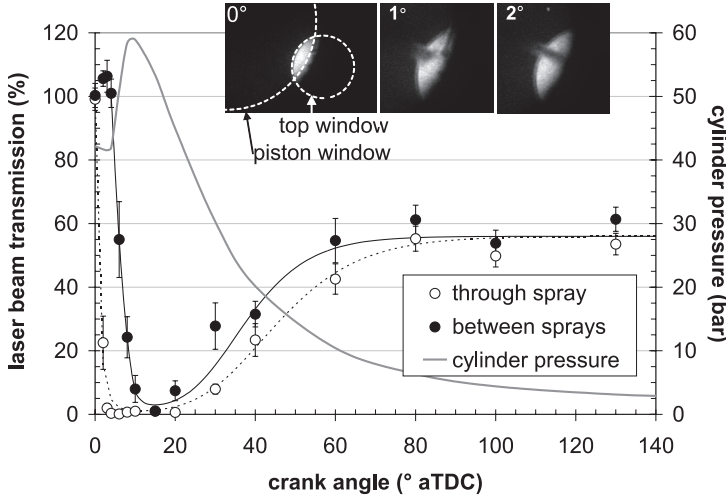


Figure 5.3: Laser beam transmission over its complete trajectory through the cylinder (averages of 15 cycles, error bars denote the standard error) The lines are added to guide the eye; the solid grey line shows the cylinder pressure. Top: shadowgraphs of the fuel spray at TDC, 1°, and 2° aTDC. The top window is uniformly and continuously illuminated, while the shadow is recorded through the piston window (window contours indicated by dashed white circles). The camera gate width is 60 μ s, which corresponds to 0.5° CA.

attenuators are soot, hot CO₂, and hot O₂. Around 20° aTDC, both curves start to increase asymptotically to about 55% (and reach 100% in the subsequent non-fired stroke).

5.4.2 NO fluorescence absorption by hot CO₂ and O₂

Fig. 5.4 displays two NO LIF images as recorded through the spectrograph at 20° aTDC and 130° aTDC. In both images the laser beam enters from the top and is directed through a fuel spray. The (0,1), (0,2), (0,3), and (0,4) emission bands are visible as “sub-images” (indicated by dashed grey contours). Along the vertical axis, these sub-images contain spatial information; the horizontal axis is a convolution of space and the (rovibronic) emission spectrum. There is no sign of O₂ fluorescence in either image. Despite the slot in the piston crown, the side window is still partly blocked at 20° aTDC, resulting in shorter sub-images.

As was mentioned in Section 5.2.1, CO₂ and O₂ are the most likely candidates for

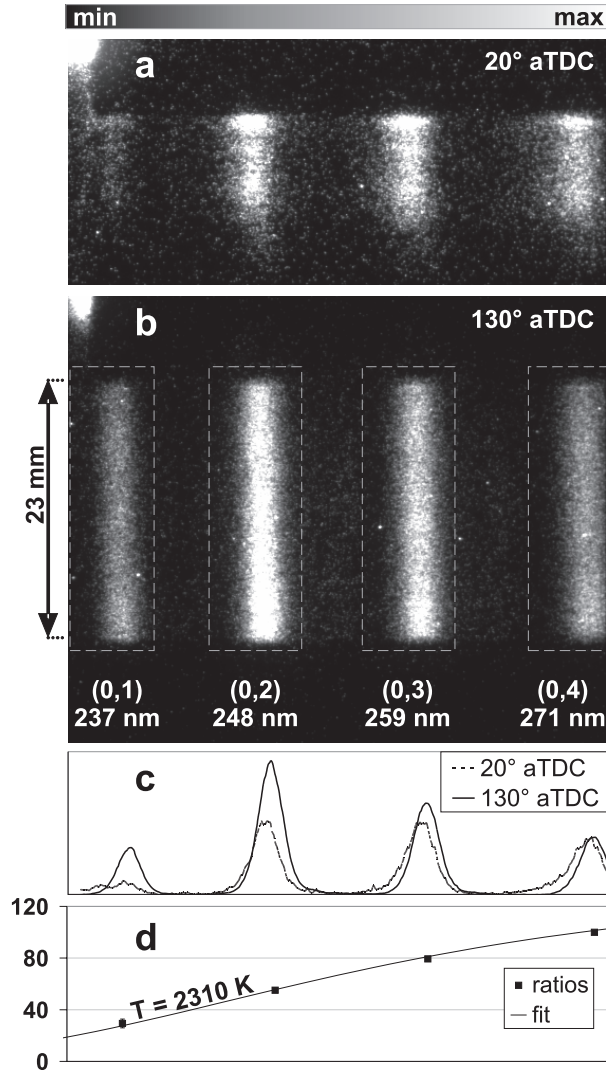


Figure 5.4: Panels a and b: two single-shot NO fluorescence images recorded through the side window and spectrograph. Four (vibronic) fluorescence bands are clearly visible at 237, 248, 259, and 271 nm. Horizontal intensity profiles (obtained by summing all relevant pixel rows, and both normalised at 271 nm) are shown in panel c. Notice the difference in relative intensity of the fluorescence bands between 20° and 130° aTDC. Panel d shows the ratio of the peak intensities in panel c (in %; black squares), as well as the fitted transmission spectrum through CO₂ and O₂ (solid line, also normalised at 271 nm).

wavelength dependent attenuation of the NO fluorescence. Since this attenuation strongly depends on the CO₂ and O₂ densities and on temperature, the fluorescence transmission will vary during the combustion stroke. This can be seen in Fig. 5.4 c: at 20° aTDC, the (0,1) and (0,2) bands are much weaker compared to the spectrum at 130° aTDC. At 130° aTDC, the average gas temperature (calculated from the cylinder pressure trace²⁹) is around 800 K, which is too low for significant CO₂ and O₂ absorption.

The relative transmission of the NO fluorescence is calculated by dividing the intensities of the four detected fluorescence bands by those at the end of the stroke (i.e. 130° aTDC). These intensity ratios (still in arbitrary units) are normalised at 271 nm, so that they represent the fluorescence transmission relative to that at 271 nm. An example is given in Fig. 5.4 d. By dividing the spectra, wavelength dependent detector response is eliminated as well.

Subsequently, these relative fluorescence transmission spectra are fitted by CO₂ and O₂ spectra (Fig. 5.4 d) using the absorption cross sections from Refs. 100 and 121. Free fitting parameters are temperature (assumed uniform over the path length) and CO₂ number density. The O₂ density is not treated as a variable, but instead determined from the local O₂/N₂ ratio¹²¹ measured by Raman scattering.

By fitting CO₂ and O₂ transmission spectra for a number of crank angles, one obtains transmission values during the combustion stroke for each NO fluorescence band. They are presented in Fig. 5.5 showing considerable attenuation of the shorter wavelengths, especially at 10–40° aTDC. Extrapolation to 226 nm is shown as well. As the cylinder volume expands (and the temperature decreases) absorption by CO₂ and O₂ decreases. By 80° aTDC, it is negligible. The fitted temperature agrees with the values reported by Flynn et al.,³⁰ reaching values of 2400 K between 20° and 30° aTDC. Later in the stroke, it approaches the average gas temperature. The obtained CO₂ number densities are realistic as well: e.g. at 40° aTDC, $n_{\text{CO}_2} = 3.4 \times 10^{18} \text{ cm}^{-3}$, whereas complete combustion of the injected 60 mg of diesel fuel would yield $n_{\text{CO}_2} = 6.2 \times 10^{18} \text{ cm}^{-3}$, assuming uniformly distributed CO₂, and taking C₁₆H₃₄ as a diesel representative.

For comparison, fluorescence transmission data based on the same analysis but using O₂ LIF instead of NO LIF are included in Fig. 5.5 as smaller symbols. Both experiments were performed under identical engine conditions, and in the same probe volume. Within the experimental accuracy and cyclic variations, the two independent results match well, proving the consistency of this method.

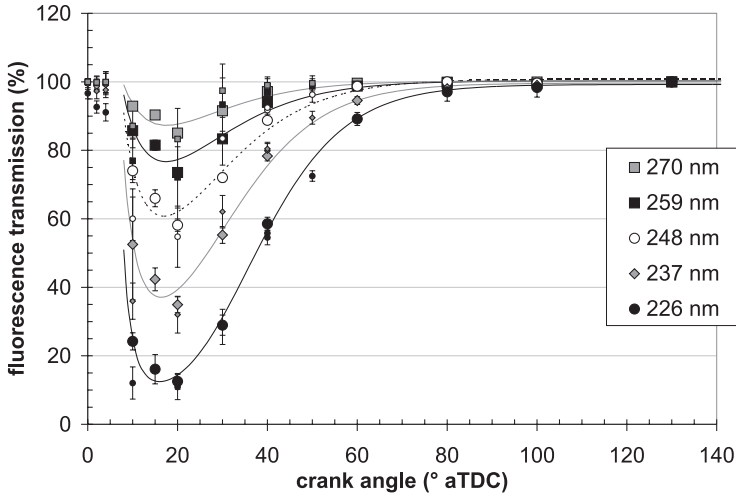


Figure 5.5: Transmission curves for the individual NO fluorescence bands at the “through spray” location, together with an extrapolation to 226 nm. The fluorescence transmission curves are based on the observed CO_2 and O_2 absorption spectra (see Figs. 4.4 and 5.4); possible additional transmission losses due to soot are *not* included. The smaller symbols correspond to independently fitted spectra based on O_2 LIF instead of NO LIF. All data points are averages of 15 laser shots; the error bars represent the standard error. The lines are drawn to guide the eye.

5.4.3 Bidirectional LIF

For the bidirectional LIF measurements, NO LIF images like those in Fig. 5.4 have been recorded separately for the two opposite directions of the excitation laser beam. Vertical NO LIF profiles are constructed by summing the intensities of the pixel rows (horizontal direction in Fig. 5.4) in all NO subimages and plotting this sum as a function of the vertical distance z (see also Fig. 5.1). Two vertical LIF profiles recorded at 16° aTDC are presented in panel a of Fig. 5.6. At 16° aTDC, only the uppermost 13 mm of the combustion chamber are visible. The two profiles have not been recorded simultaneously for practical reasons; average profiles of ten shots (20 for bottom-up propagation where the signal is weaker) are presented here instead. A similar example is given in panel b for 40° aTDC.

Panels c and d show S_q (defined in Eq. 5.7) for 16° and 40° aTDC, respectively, together with a fit of the exponentially decaying curve described in Eq. 5.8. This fit follows the data very well, indicating that a third degree polynomial is indeed

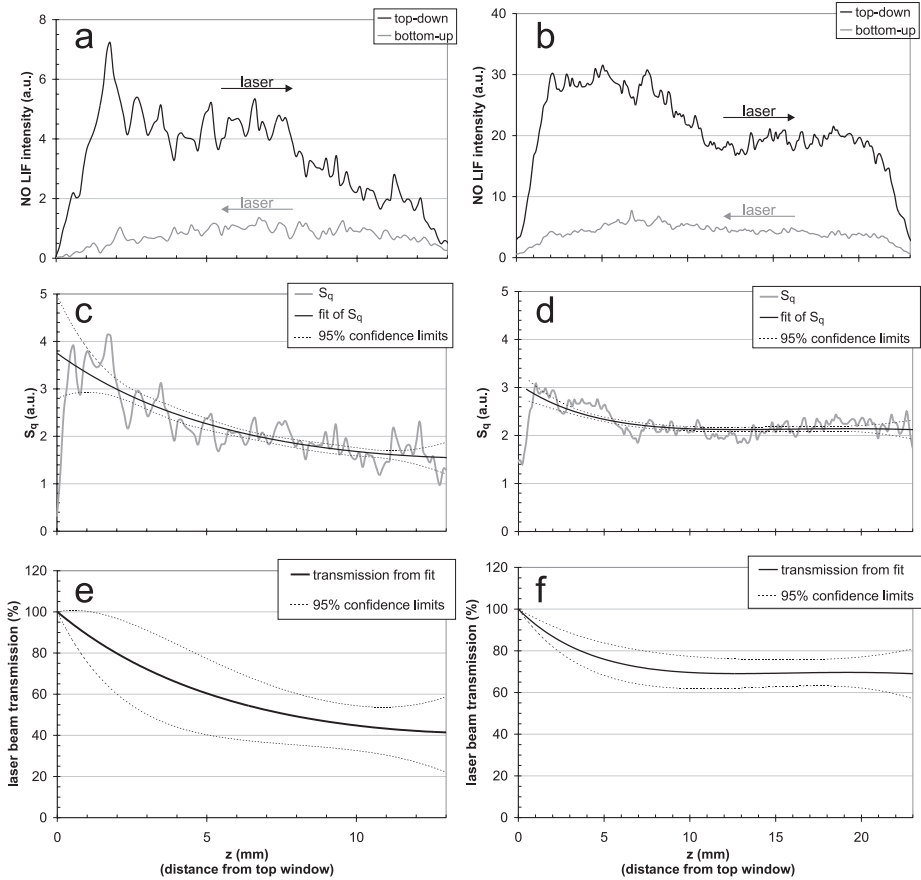


Figure 5.6: Vertical cross sections of the LIF signal for both laser beam directions at 16° aTDC (panel a) and 40° aTDC (panel b). The square root of their quotient, S_q , including a fit, is given in panels c and d for the two crank angles. The local laser beam transmission (downward laser beam), calculated from the fit through S_q , is shown in panels e and f.

sufficient to describe the extinction coefficient. The 95% confidence limits are based on numerical simulations, and show the highest uncertainty around $z = 0$ and $z = L$ (where the signal-to-noise ratio of S_q is lowest). This affects the accuracy of the overall constant p_1 , and as a consequence the 95% confidence intervals for the transmission curves (panels e and f) are considerably larger than those for the fit of S_q . A more detailed description of the noise sensitivity of this method is presented in Appendix II.

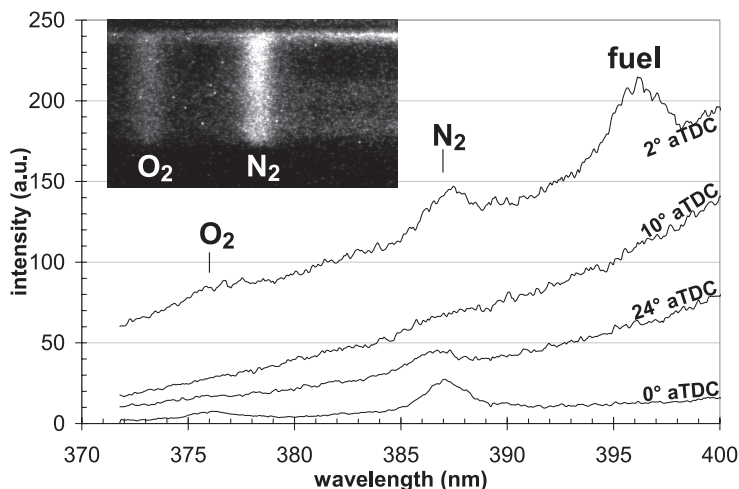


Figure 5.7: Raman scattering spectra recorded during the combustion stroke. Each spectrum is averaged over 20 cycles. A typical image (20-shot average, taken at 6° bTDC) is shown in the upper left corner.

At 40° aTDC the laser beam attenuation is not as strong as at 16° aTDC. Additionally, the NO signal is much stronger, increasing the signal-to-noise ratio of S_q . The results for 40° aTDC show a 30% attenuation of the laser beam, even though the two NO LIF profiles have similar *shapes* by eye judgement, which would suggest negligible extinction.¹¹⁰ This apparent inconsistency stresses the importance of a quantitative analysis.

5.4.4 Raman scattering by N₂

Raman spectra, recorded in the engine, are shown in Fig. 5.7. They are obtained by summing the intensities of all (relevant) pixel rows of an iCCD image similar to the example in the upper left corner. These spectra have been recorded during the first 40° CA of the combustion stroke. Later in the stroke the signal becomes weaker due to decreasing density.

Already at 2° aTDC is the spectrum dominated by broad-band radiation, caused by (laser-induced) incandescence (LII) of soot, and/or laser-induced fluorescence of aromatic fuel components.^{124, 125} The actual Raman intensities are obtained by fitting a set of Gaussians to the spectra, including a broad one to account for the background. An additional feature at a Raman shift of $\sim 3000\text{ cm}^{-1}$, corresponding

to the C–H stretch and attributed to fuel, can be observed at 397 nm between 2° and 6° aTDC.

The possible presence of LII raises the question if the laser beam is not simply burning soot away, thus measuring too low extinction. Vander Wal and Jensen¹²⁶ observed that 1064 nm laser beam transmission through a sooting flame suddenly improved for fluences above 0.5 J/cm². Above this threshold intensity, the initial part of the laser pulse causes soot to evaporate, improving the transmission of the later part. They estimated that this threshold scales with wavelength, leading to 0.2 J/cm² for 355 nm radiation. In order to compensate for the relatively weak Raman scattering, the laser fluence was kept at 1.0 J/cm² in our experiments, clearly exceeding the threshold of 0.2 J/cm². Yet, for a Gaussian laser beam profile (as in our measurements) the intensity threshold is somewhat higher¹²⁷ (Vander Wal and Jensen used a top-hat beam profile). Moreover, C₂ fluorescence, indicative of soot particle fragmentation, was not observed in our experiments.

The curves in Fig. 5.7 nicely demonstrate the effect of attenuation: at 10° aTDC hardly any N₂ signal is visible, and even the broadband background is less compared to 2° aTDC. The broadband luminosity never disappears completely; the strong attenuation (as reflected in the N₂ signal) is possibly partly compensated by increased emission due to increased soot volume fraction (if the signal is due to LII) or increased fuel density (if it is fuel LIF). Both soot and fuel droplets do attenuate the N₂ Raman intensity, of course. By 24° aTDC, there is a clear N₂ peak again, indicating that the transmission has already increased.

The N₂ signal can be interpreted as the product of the laser beam transmission and the transmission of the Raman-scattered light. To this end, the crank angle dependence of the *local* N₂ density is calculated from (1) the cylinder volume and (2) the ratio of the local temperature (estimated from the fitted absorption spectra) and the average gas temperature (calculated from the cylinder pressure trace²⁹). Additionally, the N₂ Raman scattering cross section depends on temperature,⁴⁹ and can be calculated using the estimated local temperature. Furthermore, the scattering and absorption properties of soot particles depend on wavelength, particle size, and the refractive index of soot (itself also a function of wavelength). As a result, the extinction observed at the Raman wavelengths is slightly different than for NO LIF wavelengths. This effect is discussed in Appendix I. Finally, the corrected curves (still in arbitrary units) are scaled to 100% transmission at crank angles before the start of injection. They will be addressed in Section 5.5.3.

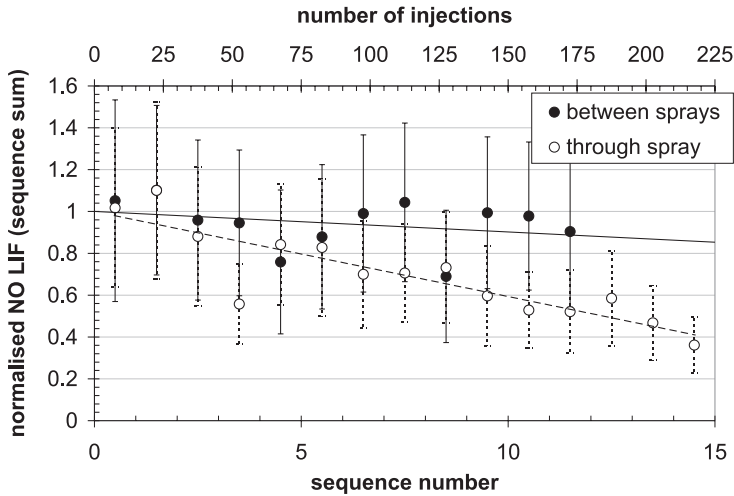


Figure 5.8: Window transmission during a measurement session, for both fuel spray configurations. The normalised total NO LIF per crank angle sequence is plotted as a function of sequence number. Each sequence consists of 15 engine firings. The error bars reflect the large variation in raw NO LIF intensity during the stroke.

5.4.5 Window fouling

Figure 5.8 shows the normalised NO LIF intensity (at constant crank angles) during a measurement session. The decreasing trend is attributed to window fouling (the error bars are due to cycle-to-cycle variations¹⁰⁹). The fouling rate for the “through spray” probe location is significantly higher than for the other position, in agreement with visual inspection of the detection window after a measurement session. This is explained by the different orientation of the fuel injector: for the “through spray” measurements the fuel jet is directed towards the slot in the piston crown, causing more soot to deposit on the detection window. The curves show that window fouling effects are respectively $\leq 4\%$ and $\leq 1\%$ for the “through spray” and “between sprays” locations, for the measurement order in our experiments*. This is negligible compared to the cyclic fluctuations (typically 25–30%).

*The NO LIF measurements are repeated in sequences of increasing crank angle, each sequence consisting of 15 crank angles.

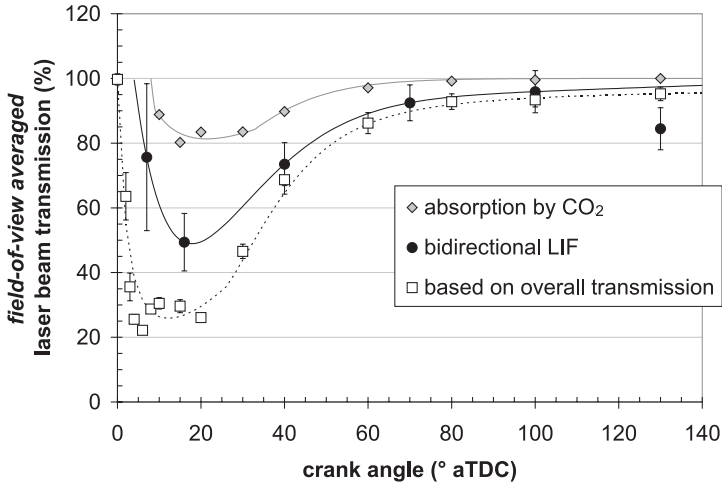


Figure 5.9: Field-of-view averaged laser beam transmission, according to different measurements. The curves are based on (overall) laser beam transmission assuming uniform attenuation (Fig. 5.3), bidirectional LIF (Fig. 5.6), and measured absorption by CO₂ (Fig. 5.5, assuming similar CO₂ absorption for both the laser beam and the NO fluorescence). The lines are drawn to guide the eye.

5.5 Discussion: complete attenuation correction requires combination of techniques

5.5.1 Bidirectional LIF versus laser beam extinction

From Fig. 5.6 it follows that laser beam extinction is not at all uniform, not even over the relatively small field of view of 23 mm (compared to the stroke of 146 mm). As a consequence, overall laser beam transmission measurements (Fig. 5.3) are not suitable for accurate attenuation correction. This is illustrated in Fig. 5.9, displaying the *field-of-view averaged laser beam transmission** as derived from both the bidirectional LIF results and the overall transmission data, assuming uniform attenuation for the latter (the CO₂ absorption curve is discussed below). Until about 40° aTDC, the laser beam transmission measurements greatly underestimate the local laser intensity. This leads us to the conclusion that the major laser beam

*The field-of-view averaged transmission is obtained by averaging the transmission curve between $z = 0$ and $z = L$. It thus is a measure for the average laser beam intensity in the probe volume.

attenuation takes place *below* the field-of-view, most likely within the piston bowl. This is also reflected in the window fouling; after a measurement session, the piston window is generally more opaque than the detection window.

5.5.2 CO₂ and O₂ absorption in relation to the total attenuation

The extrapolation of the fluorescence transmission to 226 nm in Fig. 5.5 suggests that the laser beam, too, may be strongly absorbed by hot CO₂. O₂ absorption, on the other hand, is negligible for the laser beam as its frequency is carefully chosen to avoid O₂ excitation. According to the conceptual model proposed by Flynn et al.,³⁰ hot CO₂ is concentrated around the diffusion flame. As a consequence, the laser beam and the NO fluorescence would traverse similar regions with high temperature and high CO₂ density, and it is reasonable to expect similar CO₂ absorption for the two.

It is illustrative to compare the (field-of-view averaged) laser beam transmission through hot CO₂ with the transmission obtained from the bidirectional LIF results, the latter reflecting *all* contributions to laser beam attenuation. The laser beam attenuation by CO₂ can be calculated from the fit parameters from Fig. 5.5, accounting for the shorter path length (23 mm against 37 mm). It is included in Fig. 5.9. During the first 40° CA, CO₂ absorption contributes for 30% to the total extinction. The remaining laser beam attenuation, most likely absorption and scattering by soot particles, is readily calculated. It has been used to estimate the soot-based attenuation of the NO fluorescence.

5.5.3 Combined transmission of laser beam and fluorescence

The product of laser beam transmission and fluorescence transmission can be obtained by combining the bidirectional LIF data (yielding the local laser beam transmission, the middle curve in Fig. 5.9) and the CO₂ and O₂ transmission curves of the fluorescence radiation, Fig. 5.5). The remaining fluorescence attenuation by soot can be estimated from Fig. 5.9 (Section 5.5.2).

Alternatively, the N₂ Raman scattering data already encompass the combined laser beam and fluorescence transmission, albeit without the effect of absorption by CO₂ and O₂ (the Raman wavelengths are beyond the absorption range of CO₂ and O₂). This absorption, however, is easily included taking the data in Fig. 5.5.

This brings us two combinations of techniques to assess the combined transmission:

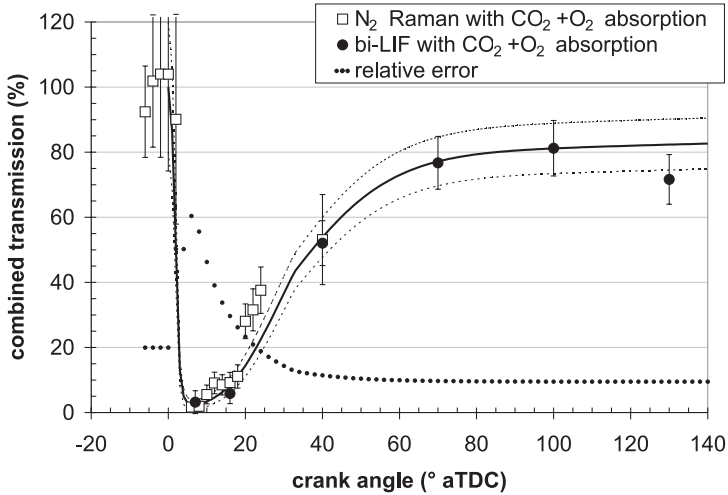


Figure 5.10: Product of the laser beam transmission (averaged over the field of view) and the fluorescence transmission, including both weakly wavelength-dependent (soot) and wavelength-dependent attenuation (CO_2 and O_2 absorption). The error bars for the Raman scattering curve include additional data processing errors (i.e. temperature dependence and difference in wavelength range, see Appendix I). The lines are drawn to guide the eye; dashed lines indicate the $1\text{-}\sigma$ confidence limits. The (estimated) relative uncertainty is shown as a dotted line.

1. bidirectional LIF combined with CO_2 and O_2 absorption spectra, and
2. N_2 Raman scattering, also combined with CO_2 and O_2 absorption spectra

The two resulting curves are shown in Fig. 5.10, and show good agreement. This demonstrates the reliability and accuracy of either combination. The relative accuracy is generally around 20%, except at very low transmission (2%), when it reaches 50–60%. Yet, attenuation correction of NO LIF signals is possible at all crank angles of interest.

5.6 Discussion: comparison of excitation-detection schemes for NO LIF

The combined laser beam and fluorescence losses depend on the wavelengths used for excitation and detection. Bessler et al. have discussed several excitation-detection

schemes for NO measurements in high-pressure combustion.¹⁰² One of the discussion points is the effect of CO₂ absorption on these excitation-detection schemes in terms of laser beam and fluorescence losses in piston engines. For their particular experimental geometry (laser beam entering through cylinder window, travelling 40 mm; LIF detected through piston window, travelling 10 mm), absorption losses were found minimal for $A \leftarrow X(0,2)$ excitation of NO at 248 nm.¹⁰² In our setup, the fluorescence path is considerably *longer* than that of the laser beam, necessitating a new analysis.

The transmission curves in Fig. 5.5 allow us to predict the field-of-view averaged laser beam transmission for other NO excitation wavelengths, again assuming similar absorption by CO₂ and O₂ for the laser beam and the fluorescence. This way, the transmission losses can be calculated for each excitation laser wavelength and for each detected fluorescence band, allowing several excitation-detection schemes for NO LIF to be compared. The individual fluorescence transmission curves are averaged using the appropriate Franck-Condon factors as weight factors. Additional losses by soot are not included, but since these are almost equal for all schemes, they do not affect our conclusions (the weak wavelength dependence of soot-based attenuation is neglected). Figure 5.11 shows the product of laser beam and fluorescence transmission curves (i.e. *combined* transmission) for the following excitation-detection schemes:

1. excitation at 226 nm and detecting red-shifted fluorescence at 237, 248, 259, and 272 nm;
2. excitation at 237 nm and detecting red-shifted* fluorescence at 248, 259, and 272 nm;
3. excitation at 248 nm and detecting blue-shifted† fluorescence at 226 and 237 nm.

With a spectrograph, simultaneous detection of blue- and red-shifted fluorescence is possible, whereas bandpass filters limit the choice of detection wavelengths to either red- or blue-shifted fluorescence. The abovementioned schemes can be, and have been, implemented using band-pass filters (see e.g. Refs. 4, 11, 14), but we advocate the use of a spectrograph as it provides an on-line monitoring of spurious fluorescence

*Detection of blue-shifted fluorescence at 226 nm is possible, but yields lower signal than the combined (0,2) and (0,3) bands⁹⁵

†Detection of red-shifted fluorescence is not recommended due to lower signal and increased interference by O₂ LIF.¹⁰²

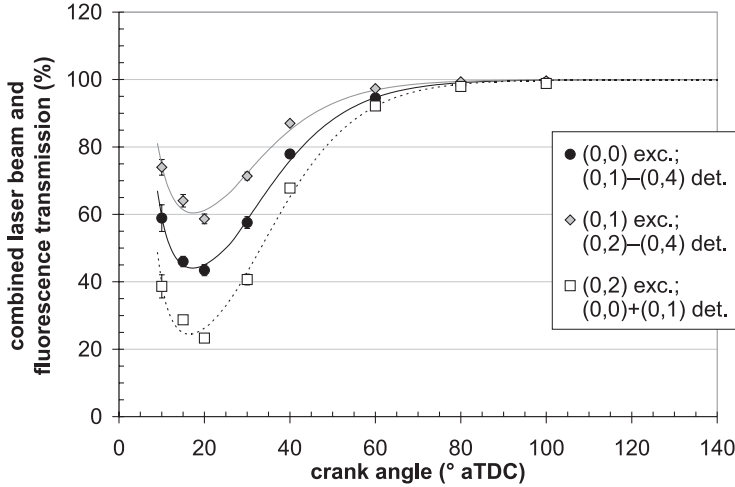


Figure 5.11: Combined laser beam and fluorescence transmission curves for three excitation-detection schemes commonly used for NO LIF measurements in combustion, applied to the geometry of our experimental setup. The laser beam transmission — averaged over the field of view — is based on the fluorescence transmission curves in Fig. 5.5 assuming uniform attenuation. Broadband attenuation is not included but has the same effect on all schemes. The lines are drawn to guide the eye.

interference. Figure 5.11 shows that, in terms of attenuation, 237 nm excitation would clearly be advantageous in our setup, with a combined transmission of at least 59% compared to 44% and 23% for 226 nm and 248 nm excitation, respectively. The apparent discrepancies with the calculations by Bessler et al.¹⁰² are caused by differences in experimental geometry, detection wavelengths (in the case of 226 nm excitation), temperature, and column densities of CO₂ and O₂, showing that the “optimal” (i.e. least affected by absorption) scheme for NO detection indeed depends strongly on the experimental configuration.

Besides attenuation effects, absolute signal strength is an important selection criterion for excitation-detection schemes. The signal strength varies from one scheme to the other, additionally depending on the available laser power, population(s) of the laser-excited state(s), transition strength, spectral sensitivity of the detection system, and the number of detected fluorescence bands. In Fig. 5.12 we predict the signal strength in our engine for the above-mentioned schemes, taking into account the effects of (vibrational) energy level population (using the temperature from the fits in Fig. 5.5), transition probabilities (i.e. Einstein absorption and emission co-

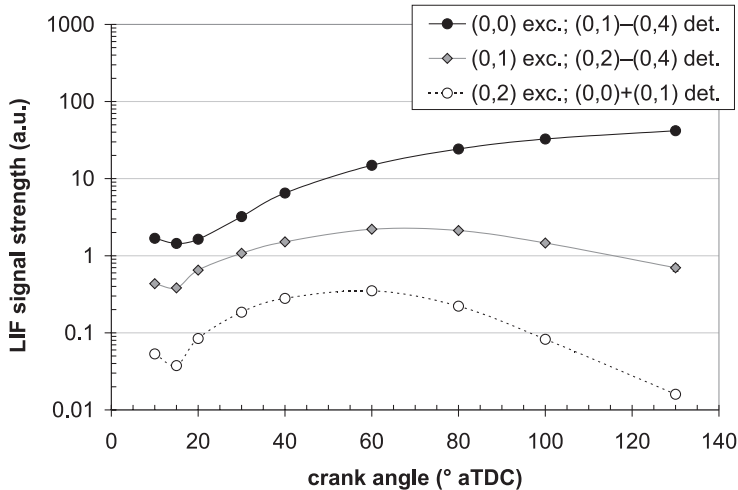


Figure 5.12: Signal strength for three NO excitation-detection schemes, calculated from Fig. 5.11. The additional effects of (vibrational) energy level population and transition probability (Einstein A-coefficients) have been included. Laser power and detection efficiency have been assumed equal for these schemes. The lines are drawn to guide the eye.

efficients), quenching, and, of course, attenuation (Fig. 5.11). As a consequence, these curves may be interpreted as LIF intensities per NO molecule per laser pulse energy unit. Detector sensitivity is not included. It is obvious that 226 nm excitation yields the strongest signal throughout the combustion stroke (note the logarithmic ordinate).

5.7 Summary and conclusions

We have demonstrated three laser diagnostic techniques for assessment of (fractions of) the attenuation involved in in-cylinder NO LIF experiments. Complete attenuation corrections require combination of techniques, combining CO₂ and O₂ absorption spectroscopy with (1) bidirectional LIF or (2) N₂ Raman scattering. When a spectrograph is used, the fluorescence absorption by CO₂ and O₂ can be retrieved from the NO LIF spectra themselves, and only one additional measurement is required, being either the second, reversed laser pulse for bi-LIF, or N₂ Raman scattering. All methods can in principle be used on a single-shot basis, although

this requires extensive equipment, and averaging may be a good alternative. In our experiments, signal-to-noise levels did not allow a single-shot approach. The bidirectional LIF combination yields slightly better signal-to-noise ratios (as is reflected in the error bars in Fig. 5.10). The accuracy of the Raman-based transmission measurements can be improved by selecting an excitation wavelength that is closer to 226 nm (Appendix I).

The bidirectional LIF results indicate that laser beam attenuation is far from uniform, being mainly localised in the piston bowl. This implies that (overall) laser beam transmission measurements cannot be used to accurately determine the local laser beam intensity.

UV absorption by CO_2 and O_2 leads to significant attenuation. Up to 40° aTDC, CO_2 causes one third of the laser beam attenuation, the remaining part being attributed to soot (scattering and absorption). Later in the stroke, absorption by CO_2 and O_2 is less prominent due to the lower temperatures. If the local O_2 density is not known, the transmission of the NO fluorescence could be estimated by fitting only the CO_2 absorption cross section. In our case, this yields fits of equal quality, deviating by $\sim 10\%$ from those in Fig. 5.5. The fitted CO_2 density is then overestimated by about 60%.¹²¹

The wavelength dependence of the absorption by CO_2 and O_2 should be kept in mind when selecting an appropriate excitation-detection scheme for NO LIF measurements. The actual effect of such absorption on some commonly used schemes strongly depends on the experimental geometry. In our setup, $A \leftarrow X(0,1)$ excitation with red-shifted detection is least affected by CO_2 and O_2 absorption, although attenuation up to 40% is still predicted. In terms of absolute signal strength, $A \leftarrow X(0,0)$ excitation is clearly advantageous, yielding the strongest NO signal per laser pulse energy throughout the entire combustion stroke.

Despite the short path lengths in our experimental configuration, the laser beam and the NO fluorescence are heavily attenuated, reaching (combined) transmission levels as low as 2%. Later in the stroke, it increases to 85%. Since even the lowest observed transmission can be measured reasonably accurately (50–60% relative error), correction of NO LIF for attenuation effects is now possible at all relevant crank angles. Applications of these findings for quantitative in-cylinder NO measurements have been published elsewhere¹⁰⁹ (Chapter 6).

Acknowledgements

This research is supported by the Technology Foundation STW, applied science division of NWO and the technology programme of the Dutch Ministry of Economic Affairs.

Appendix I: Wavelength-dependence of extinction by soot particles

Many studies of the optical properties of soot have been reported, showing a considerable variety in extinction spectra and the derived refractive index. Here, we refer to UV-visible extinction spectra measured in the exhaust of a diesel engine.^{117,128,129} These experiments (soot primary particle diameter $d_p = 20 - 25$ nm) show a wavelength dependence of the extinction coefficient K_{ext} that is very close to that in the Rayleigh approximation (valid for $d_p < 0.1\lambda$), i.e. $K_{\text{ext}} \propto \lambda^{-1}$. Despite coagulation of particles into chain-like structures, the observed extinction and scattering spectra can be attributed to the primary particle size.¹¹⁷ Schnaiter et al. reported that, above a certain aggregate size, coagulation hardly influences the extinction spectra.¹²⁹ Furthermore, the extinction scales with λ^{-D_f} , where D_f is the fractal dimension of the aggregate ($D_f = 1$ for a chain of primary particles).

Time-resolved laser-induced incandescence measurements in our engine indicate primary particles around 50 nm.¹³⁰ Although this is in the order of the Rayleigh limit, we will use the ratio 355/226 to scale the soot-based attenuation obtained with N₂ Raman scattering to 226 nm, with an estimated relative error of 20%. (This value is in agreement with more detailed calculations, extending the valid range to $d_p < 0.25\lambda$ by taking higher order terms of the Mie theory expansion into account.)

Appendix II: Noise analysis of the bidirectional LIF method

The sensitivity of the bidirectional LIF method to noise on the input signals S_{down} and S_{up} has been studied with numerical simulations. In these simulations, the spatial resolution, the extinction and scattering distributions, and signal strength were kept identical to the data in panels a and b, but different amounts of noise were added. The noise characteristic of the iCCD cameras was modelled assuming

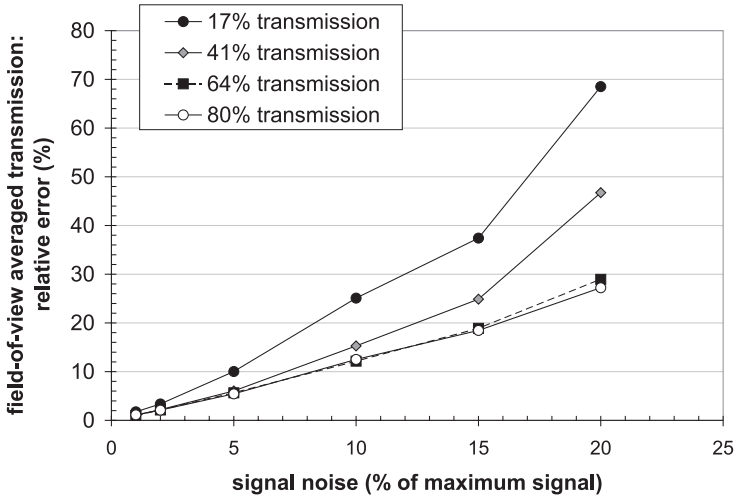


Figure 5.13: Dependence of the fitted laser beam transmission curve (averaged over the field of view) on the signal noise level.

Poisson statistics.¹³¹ For each given noise level, the S_{up} and S_{down} signal were generated 100 times, and the resulting laser beam transmission was calculated for each generation.

The relative uncertainty of the (field-of-view averaged) laser beam transmission as a function of the noise on the S_{down} and S_{up} signals is shown in Fig. 5.13 (the curve for 41% transmission). This analysis was repeated for different extinction values (multiplying the extinction distribution by a factor of 0.25, 0.5, or 2), covering the range observed in the combustion stroke. The noise dependence behaves linearly, except for higher extinction values or high noise levels (both leading to low signal-to-noise ratios). Judging from the graph in Fig. 5.13, noise levels of 15 – 20% (i.e. signal-to-noise ratios of 6 – 5) are still accepted by the algorithm.

Chapter 6

Quantitative laser-induced fluorescence measurements of nitric oxide in a heavy-duty diesel engine*

Abstract

We present quantitative, in-cylinder, UV-laser-induced fluorescence measurements of nitric oxide in a heavy-duty diesel engine. Processing of the raw fluorescence signals includes a detailed correction, based on additional measurements, for the effect of laser beam and fluorescence attenuation, and for the pressure and temperature dependence of the fluorescence efficiency, based on numerical modelling. These corrections are largest early in the stroke, when quenching rates are high and UV transmission is low. Together, they vary over more than three orders of magnitude during the combustion stroke.

Fully quantitative results are realised by an overall calibration using independent concentration measurements in the exhaust gas. The data provide evidence of NO formation during both the premixed and mixing-controlled combustion phases.

*Adapted from: K. Verbiezen, R.J.H. Klein-Douwel, A.P. van Vliet, A.J. Donkerbroek, W.L. Meerts, N.J. Dam, and J.J. ter Meulen, *Proceedings of the Combustion Institute* 31 (2006)

6.1 Introduction

Reduction of nitrogen oxides (NO_x) emissions from diesel engines requires fundamental knowledge of the formation processes involved. Numerical models describing the complex chemistry and fluid dynamics of diesel combustion are important for the efficient evaluation of new engine designs. These models should be validated with experimental results obtained under characteristic engine conditions. To this end, laser techniques are frequently used, offering robust and non-intrusive diagnostics for measurements at high spatial and temporal resolution.

Although laser-induced fluorescence (LIF) has often been employed for visualisation of nitric oxide (NO) in diesel engines²⁻⁸ and SI engines,⁹⁻¹⁵ quantification of the LIF signals in terms of NO densities or mole fractions has proven to be very difficult, requiring (1) knowledge of the (local) excitation laser intensity, (2) knowledge of the attenuation of the ensuing NO fluorescence, and (3) a good spectroscopic model predicting the dependence of NO LIF on temperature, pressure, and gas composition. Finally, the local temperature needs to be known.

This chapter presents quantitative, crank-angle resolved NO LIF measurements in a diesel engine by means of $A \leftarrow X(0,0)$ excitation at 226 nm. Correction strategies for laser beam and fluorescence attenuation are discussed extensively in a separate paper¹⁰⁸ (Chapter 5), but will be briefly summarised here. We compare the pressure and temperature dependence of NO LIF as predicted by LIFSim⁶⁴ to our calculations, with special attention to the influence of the gas composition.

6.2 NO LIF signal dependence

The fluorescence intensity is determined by a number of (pressure and temperature dependent) factors. Generally, for a laser-induced $i \rightarrow j$ transition, the fluorescence signal from state j to k can be written (in the weak excitation limit) as

$$S_{\text{LIF}}^{(k)} \propto N_{\text{NO}} I_{\text{laser}} \tau_F f_B g(\nu_L, \nu_{ij}) B_{ij} \frac{A_{jk}}{\sum_l A_{jl} + Q_j}, \quad (6.1)$$

where N_{NO} is the NO number density in the laser probe volume, I_{laser} the local laser intensity, and τ_F the fluorescence transmission on its way to the detector. $f_B(T)$ is the Boltzmann fraction, $g(\nu_L, \nu_{ij})$ the overlap integral of the laser spectral profile and the absorption line, and B_{ij} the Einstein coefficient for this transition. The fraction at the right is known as the Stern-Vollmer factor, and is the ratio of the fluorescence rate (i.e. the spontaneous emission coefficient A) to the total

Table 6.1: Engine specifications and operating conditions.

engine type	four-stroke, DI diesel engine
bore	130 mm
stroke	146 mm
displacement	1.939 ℓ (per cylinder)
compression ratio	15 (unmodified: 16)
swirl number	1.8
fuel injected	60 mg city diesel
boost pressure	1.4 bar (abs.; no EGR)
speed; gIMEP	1430 rpm; 500 kPa

decay rate, including other fluorescent transitions and non-radiative collisional energy transfer (rate constant Q). Since pressure broadening and collisional quenching are species dependent, evaluation of Eq. 6.1 depends on the gas composition. Results may be presented in terms of number densities, N_{NO} , or mole fractions, x_{NO} , related by

$$x_{\text{NO}} = \frac{N_{\text{NO}}}{N_{\text{total}}} = N_{\text{NO}} \frac{k_B T_{\text{probe}}}{p}, \quad (6.2)$$

with N_{total} the total number density, k_B Boltzmann's constant, T_{probe} the local temperature, and p the pressure.

6.3 Experiment

6.3.1 The engine

The optical engine is a heavy-duty, six-cylinder diesel engine; specifications are listed in Table 6.1. Fig. 6.1 shows the optically accessible measurement cylinder. A slot machined into the piston crown allows observations through one of the side windows even at Top Dead Centre (TDC). The (cam-driven) fuel injection takes place through a central, eight-hole nozzle. The injector can be rotated, allowing measurements at different positions relative to the fuel sprays without repositioning the laser beam. The top window can be replaced by a pressure transducer (AVL QHC32). To avoid overheating the non-lubricated measurement cylinder is skip-fired (1:35). Steady-state conditions are mimicked by (pre-) heating the cooling water to operational temperatures.

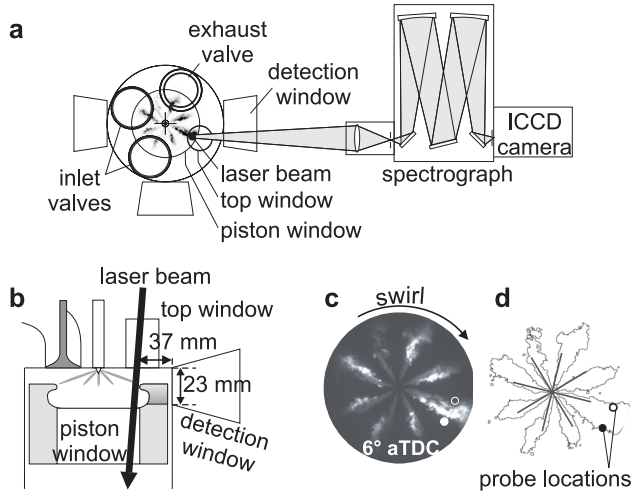


Figure 6.1: Schematic representation of the setup: (a) top view; (b) close-up side view of the measurement cylinder; (c) 100 ns snapshot of the combusting fuel sprays; (d) contour plot of the same image, indicating the two laser probe positions and the spray axes (solid grey lines). The laser beam traverses the cylinder almost parallel to its axis. NO fluorescence is detected by an imaging grating spectrograph via the nearest side window.

Figure 6.2 shows some characteristics for the measurement cylinder. The heat release rate shows that combustion begins around 3° after TDC (aTDC).

6.3.2 NO LIF experiments

All measurements have been carried out with the laser beam traversing the combustion chamber parallel to the cylinder axis, probing either *through* a fuel spray or exactly *between* two sprays (indicated in Fig. 6.1 d). NO LIF is induced by laser radiation at 226.03 nm, resonant with the coinciding $A^2\Sigma(v'=0) \leftarrow X^2\Pi(v''=0)$ $P_1(23.5)$, $Q_1 + P_{21}(14.5)$, and $Q_2 + R_{12}(20.5)$ transitions. Laser radiation is produced by a frequency-mixed dye laser (Radiant Narrowscan D, using Rhodamin 101) pumped by a seeded Nd:YAG laser (Continuum Powerlite Precision II 8010). The unfocussed beam (~ 3.5 mm diameter) of 5 mJ pulse energy is directed into the combustion chamber via the top window, immediately entering the field of view. Four vibronic fluorescence bands (at 237, 248, 259, and 270 nm, corresponding to the $A \rightarrow X(0,1) - (0,4)$ transitions respectively) are detected through the nearest side window by an intensified CCD camera (Roper Scientific, ICCD 512T, 512^2 pix-

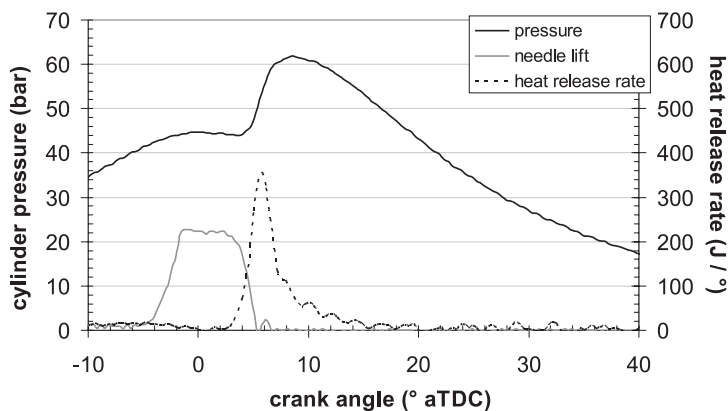


Figure 6.2: Cylinder pressure, heat release rate, and needle lift (in arbitrary units) for the engine conditions relevant here.

els, 16 bits) mounted behind a spectrograph (ARC SpectraPro 500i, 600 lines/mm grating). The entrance slit of the spectrograph is parallel to the laser beam direction, and fully opened for maximum signal. Elastic scattering is suppressed by a 0° 226-nm mirror. In this configuration, the path lengths of laser beam and fluorescence within the combustion chamber are kept minimal (23 and 37 mm, respectively), thereby minimising the effect of attenuation.

Fluorescence imaging through a grating spectrograph is advantageous for a number of reasons. Firstly, it allows correction for any broadband background signal (which was found negligible in our measurements). Secondly, interference of LIF from O_2 molecules can be monitored (found to be minimal in our experiments). Thirdly, since the spectrograph provides NO fluorescence images for each vibronic emission band individually, variations in relative band intensities throughout the stroke can be used to derive effective attenuation coefficients,¹⁰⁸ as will be described in more detail below. As a disadvantage, imaging through a grating spectrograph degrades spatial resolution. If desired, this can be compensated for to a large extent by proper post-processing,^{132, 133} but that is not pursued here.

6.3.3 Attenuation measurements

Ideally, all attenuation correction experiments (detailed below) are performed simultaneously with the NO LIF measurements. Due to practical reasons this was not feasible in our setup (except for the attenuation assessments that are based on the

NO LIF spectrum itself, see Section 6.4.2). As a consequence, we correct cycle-averaged NO measurements with cycle-averaged attenuation factors. Of course, the engine conditions and the two probe positions were identical for all measurements.

6.3.4 Calibration

The NO LIF measurements are calibrated by scaling the in-cylinder concentration curve (still in arbitrary units) such that its value at the end of the stroke (the exhaust valve opens at 130° aTDC) matches the exhaust NO concentration, as determined by a commercial exhaust gas analyser (SIGNAL Instruments, NOX analyser series 4000). The latter is connected to the exhaust of only the measurement cylinder; its reading is scaled by the skip-fire ratio and by an additional factor* accounting for the fact that the sampling occurs non-isokinetically (see Chapter 2.5). We assume reasonably homogeneous NO distributions at 130° aTDC.

6.4 Data processing

6.4.1 Interpretation of NO LIF images

Two example NO LIF images are shown in Fig. 6.3, for 8° and 130° aTDC. The vertical axis displays spatial information (parallel to the laser beam); wavelength dispersion is in the horizontal direction. If the entrance slit of the spectrograph were narrow, one would obtain a pure spectrum. In our case (open slit), the spectra are convolved with the spatial intensity profile of the laser beam and the NO density. Still, the vibronic fluorescence bands are clearly separated. They are labelled by transition and wavelength in Fig. 6.3.

At 8° aTDC, the field of view is slightly limited by the piston blocking the lower part of the detection window, causing an apparently shorter NO image. The window is clear from 27° aTDC onwards. The examples in Fig. 6.3 show that, in our case, both O_2 interference and broadband background luminescence (i.e. laser-induced incandescence, fuel LIF) are negligible with 226 nm excitation, although some broadband (fuel) LIF can be observed at the “through spray” position shortly after TDC.

The NO measurements presented in this work are spatially averaged spectra, obtained by summing all pixel values attributed to individual fluorescence bands

*This factor was not included in the original paper, explaining why the results in Fig. 6.8 are approximately a factor two lower.

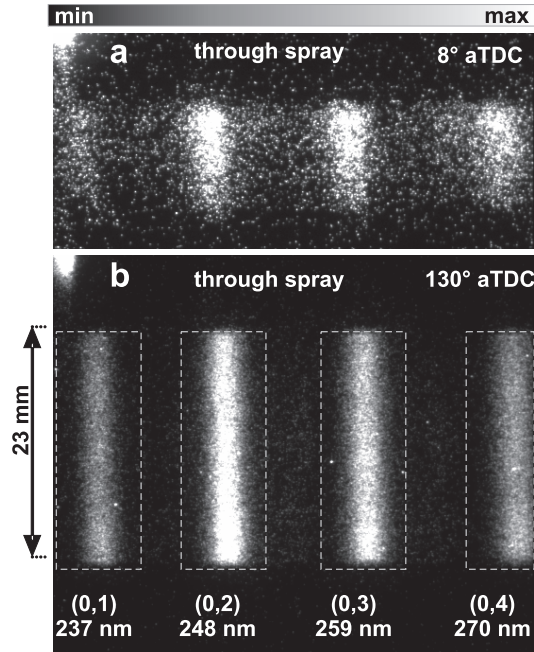


Figure 6.3: Two single-shot NO LIF images, recorded at 8° aTDC (a) and 130° aTDC (b). The intensity scales are adjusted to show maximum contrast for each image. The regions of interest for the emission bands are indicated by dashed grey rectangles in panel b. The difference in the *relative* peak intensities between the two LIF spectra is attributed to wavelength dependent fluorescence absorption by CO_2 and O_2 . This absorption is weaker at 130° aTDC due to the lower temperature. The bright spot in the upper left corner is a reflection of a fraction of the laser beam that was coupled out to monitor pulse-to-pulse energy fluctuations.

within the CCD image, corrected for background. This basically treats the NO LIF data as point measurements, sacrificing the vertical information for clarity (e.g. easy comparison of measurements at different crank angles or probe locations) and circumventing deconvolution. The vertical position dependence of the NO signal has been used, however, to assess the local laser beam extinction by means of bidirectional laser scattering.¹⁰⁸

6.4.2 Attenuation effects

Brief summary of techniques

Previously, we have presented two combinations of techniques to assess the attenuation of both the laser beam and the ensuing NO fluorescence.¹⁰⁸ Here, we briefly summarise these techniques, including (1) bidirectional laser scattering (bidirectional LIF), (2) absorption spectroscopy of CO₂ and O₂, and (3) N₂ Raman scattering.

1. With bidirectional LIF, spatial NO fluorescence intensity profiles are recorded from two counterpropagating laser pulses passing the same trajectory. From the ratio of these profiles the spatially resolved laser beam transmission is derived.^{90, 114, 122, 123}
2. The detected NO LIF spectrum is affected by broadband UV absorption by CO₂,¹⁰⁰ which changes the relative intensities of the detected emission bands at 237, 248, 259, and 271 nm. Division of this LIF spectrum by a reference spectrum (i.e. without UV absorption) yields the *relative* transmission for each NO LIF band; *absolute* transmission values can be obtained by fitting the CO₂ transmission spectrum, using the parameterised CO₂ absorption cross section in Ref. 100. This method is analogous to that by Hildenbrand and Schulz,⁹⁹ who used O₂ LIF instead of NO LIF. Additionally, the NO fluorescence will suffer absorption by O₂. As the spectrally broad NO emission bands encompass many narrow O₂ absorption lines, the *effective* O₂ absorption can be *approximated* by a smooth, CO₂-like absorption function¹²¹ (in our experiments leading to errors of $\leq 5\%$). It is fitted together with the CO₂ absorption spectrum.

By extrapolating the CO₂ absorption spectrum to 226 nm, it is possible to estimate the contribution of CO₂ absorption to the (total) laser beam extinction measured with bidirectional LIF (O₂ absorption is negligible as the laser beam is off O₂ resonance). The remaining extinction is attributed to absorption by NO and soot. The latter can be used to estimate the soot-based fluorescence attenuation.

3. Provided the N₂ density is known, its Raman scattering signal reflects the combined transmission of the laser beam and the Raman-scattered light. N₂ density variations due to temperature inhomogeneities are corrected for using the estimated local temperature (see below). In our experiments, the Raman wavelengths are beyond the CO₂ and O₂ absorption ranges, and only the

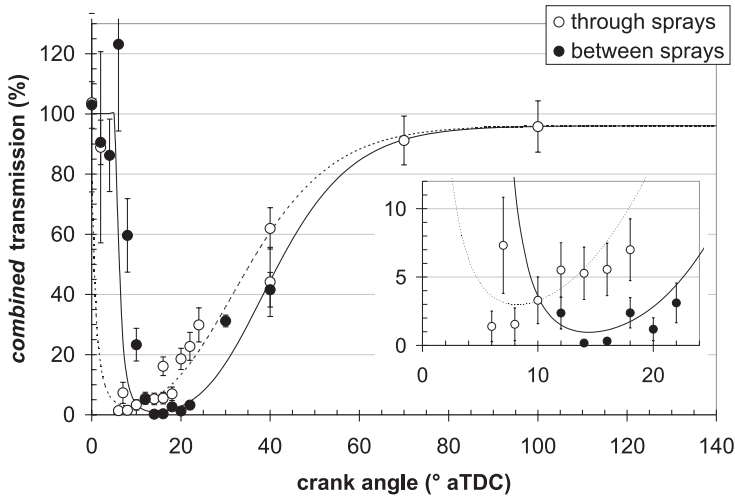


Figure 6.4: Product of the laser beam transmission and the fluorescence transmission, for both probe positions. Lines guide the eye.

essentially wavelength-independent attenuation (attributed to soot) can be retrieved.

Since each of the abovementioned techniques only reveals a part of the attenuation, it is essential to combine the CO_2 and O_2 absorption spectra with either (1) bidirectional LIF or (2) N_2 Raman scattering results, to calculate the total attenuation of laser beam and fluorescence. These two strategies show good agreement;¹⁰⁸ their average is shown in Fig. 6.4 for both probe locations. It is evident that attenuation has a significant influence on the NO LIF signal, the combined transmission ranging between 1% and 90% during combustion. The earlier transmission decrease at the “through spray” location is caused by the fuel spray hitting the laser beam; the earlier increase is explained by the air swirl motion (clockwise in Fig. 6.1c, d), moving the flames and combustion products towards the “between sprays” position. (The curves in Fig. 6.4 are slightly different from the data in Ref. 134, where fluorescence attenuation by soot was not included.)

(Self) absorption by NO

At relatively high NO number densities ($\geq 2 \times 10^{-17} \text{ cm}^{-3}$), laser beam attenuation due to NO absorption is no longer negligible. This means that the combined transmission (Fig. 6.4) and the NO density are essentially coupled. Self-consistent

values for the NO density and combined transmission were obtained by iteratively calculating the transmission (including NO laser absorption) and the resulting NO number density, typically converging within five to ten iterations. The effect of laser beam absorption by NO is included in Fig. 6.4.

Fluorescence trapping or self absorption by NO was not taken into account for two reasons. Firstly, NO self absorption spectra feature a much stronger wavelength and temperature dependence compared to CO₂, and do not match the observed relative LIF transmission. Secondly, since temperature variations along the absorption path are not accounted for (i.e. only one, effective, temperature is fitted), and due to the stronger temperature dependence of NO, the effective path length for NO absorption is expected to be considerably shorter than that for CO₂. This would result in less self absorption than calculated from the in situ measurements.

6.4.3 NO LIF dependence on pressure, temperature, and gas composition

The pressure and temperature dependent terms in Eq. 6.1 require measurement of the pressure (Fig. 6.2) and the *local* temperature. The latter can be estimated from the measured CO₂ and O₂ absorption spectra (discussed in Section 6.4.2), taking advantage of their strong temperature dependence.^{100,135} Since the CO₂ and O₂ absorption spectra are line-of-sight measurements, the fitted temperature is an effective temperature, biased to regions with strong absorption (i.e. high temperature and / or CO₂ density). However, it is arguably quite close to that in the probe volume, where we expect a temperature that is considerably higher (thus leading to stronger absorption) than in regions closer to the cylinder wall. The systematic temperature uncertainty due to this assumption is estimated at ~10%*, leading to ~5% uncertainty in the final NO density.

Figure 6.5 shows the estimated local temperature as well as the average gas temperature, derived from the pressure trace (assuming ideal gas behaviour and neglecting heat losses and blow-by).²⁹ The local temperatures are substantially higher, especially between 10° and 60° aTDC, with peak temperatures around 2500 K at 20°-30° aTDC. Later in the stroke, they approach the average gas temperature.

*This estimate is based on a number of calculations with several fictive temperature profiles along the NO fluorescence path. Each profile has a minimum at the detection window corresponding to the temperature of the unburnt gases and a maximum temperature at the probe volume. According to these calculations, the effective temperature is typically 10% lower than the maximum temperature.

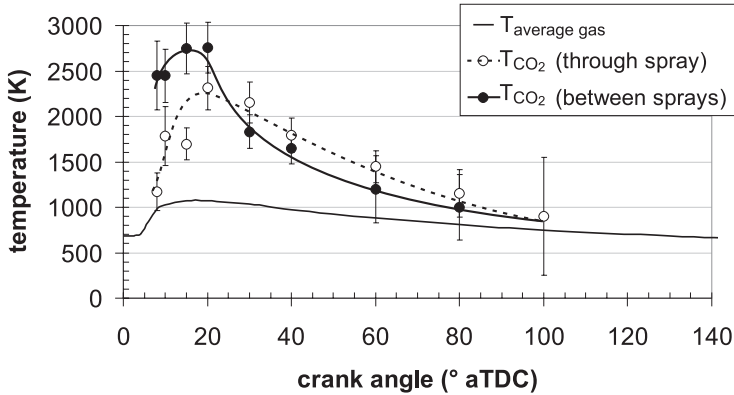


Figure 6.5: “Local” temperatures estimated from fitted CO_2 and O_2 absorption spectra,^{108,121} and the average gas temperature during the combustion stroke. Lines through the data points guide the eye.

The difference between the two local temperatures before 20° aTDC might be explained by the presence of the evaporating fuel spray, extracting heat from its surroundings; shadowgraphy experiments showed a (liquid) spray structure until at least 7° aTDC.¹⁰⁸ Another possible explanation is the swirling air motion (clockwise in Fig. 6.1c), moving the hot combustion products from the “through spray” towards the “between sprays” position. After 60° aTDC, CO_2 and O_2 absorption becomes very small, causing an increased uncertainty of the fitted spectra and thus of the inferred temperature.

The calculated NO LIF variation due to the temperature and pressure variations during the stroke is shown in Fig. 6.6, for both constant ($[\text{O}_2]:[\text{N}_2] = 1:4$) and varying composition of the in-cylinder gases. The error bars are due to uncertainties in the measured temperature and pressure. For the varying gas composition we followed the approach of Van den Boom,⁶⁵ who used mole fractions from gas sampling data by Aoyagi et al.⁸⁶ to estimate quenching rates for our engine. Our calculations show good agreement with the results from LIFSim,⁶⁴ despite our assumption of temperature-independent quenching cross sections.⁸³ Unfortunately, LIFbase⁶³ does not calculate collisional quenching rates and thus cannot be used for comparison. The difference between constant and varying gas compositions is negligible compared to the experimental accuracy, except perhaps for crank angles $< 8^\circ$ aTDC when they have the same order of magnitude. Further analysis is based on the LIFSim curve with constant gas composition.

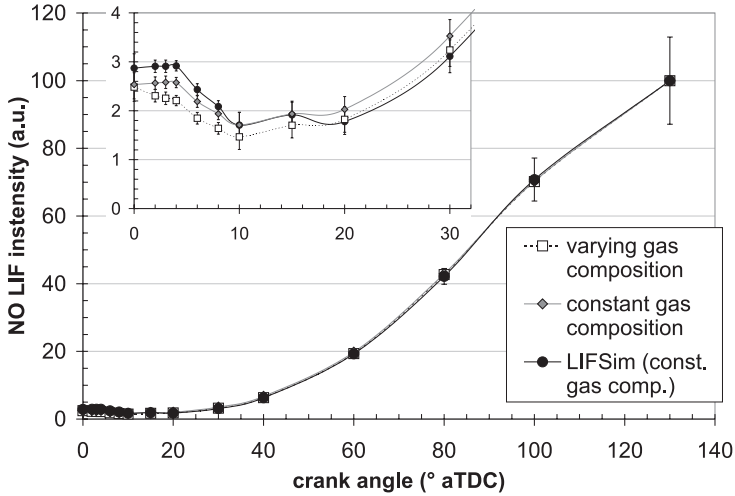


Figure 6.6: Variation of the NO LIF intensity (per molecule) during the combustion stroke due to temperature and pressure. All curves are scaled to 100 at 130° aTDC. Input pressure and temperature are shown in Figs. 6.2 and 6.5, respectively.

6.5 Results and discussion

Figure 6.7 shows unprocessed, single-shot NO LIF measurements during the combustion stroke. The uncertainty in each data point is caused by camera noise (5% for crank angles $\geq 15^\circ$ aTDC). The large variation in single-shot NO LIF intensity (standard deviation $\approx 35\%$) is attributed to fluctuations in laser pulse energy (5%), and cycle-to-cycle variations of the engine. The latter include variations in NO number density, local temperature, and attenuation effects. The 15-shot average is included in Fig. 6.7, magnified by a factor of ten to enhance the signal at early crank angles. At the “through spray” location NO molecules can be detected as early as 2° aTDC. The dip around 7° aTDC is due to attenuation effects: it resembles the combined transmission curve for this location (Fig. 6.4).

In the “between sprays” location, the earliest NO signal occurs at 8° aTDC, which is significantly later than in the fuel spray. Moreover, there is no pronounced attenuation-dip like in Fig. 6.7a, although the NO signal levels off between 10° and 20° aTDC. At 130° aTDC, both probe locations reach the same NO LIF intensity (“through spray”: $(184 \pm 17) \times 10^6$ counts; “between sprays”: $(189 \pm 9) \times 10^6$

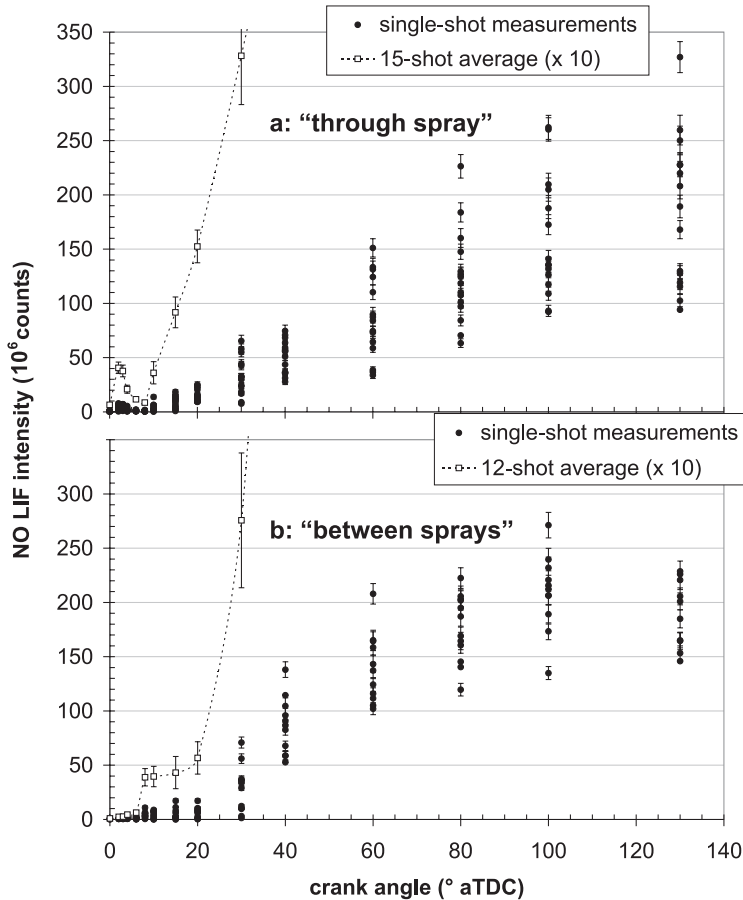


Figure 6.7: Spatially averaged NO LIF intensity versus crank angle, for both probe positions. These (raw) data have not been processed for any pressure and temperature dependence of the LIF intensity, nor for attenuation effects. The single shot error bars denote the experimental accuracy; the error bars for the 15-shot average show the standard error of the average.

counts), suggesting a uniform NO distribution at the end of the combustion stroke*. This is also reflected in (almost) uniform vertical NO LIF intensity profiles, see e.g. Fig. 6.3b. Uniform NO distributions late in the stroke have been reported before.^{4,54}

After processing the data in Fig. 6.7 for the pressure and temperature dependence of the NO fluorescence (Fig. 6.6) and for attenuation effects (Fig. 6.4), NO mole

*At 130° aTDC, temperature, pressure, and attenuation effects are equal for both locations.

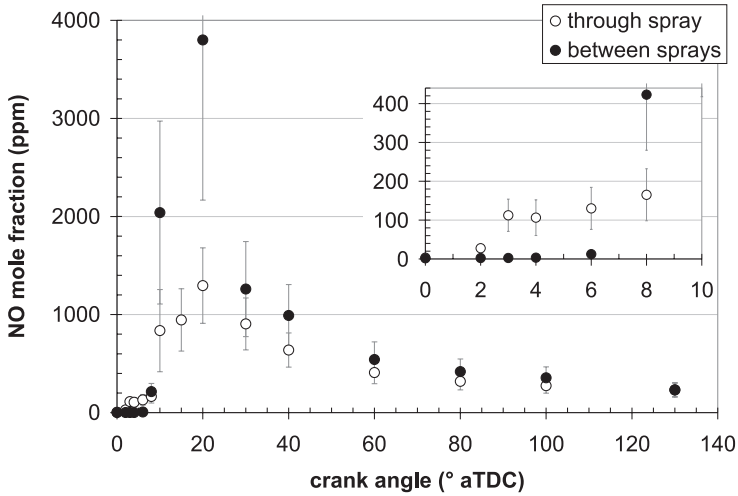


Figure 6.8: Local NO concentrations during the combustion stroke. The data points are averages of 15 laser shots; the error bars denote the standard error (due to cycle-to-cycle variations of the NO concentration, the effective transmission, and of the local temperature).

fractions are readily obtained. Window fouling effects (1% and 4% for “through spray” and “between spray”, respectively¹⁰⁸) are negligible compared to cycle-to-cycle variations. Subsequently, both curves are scaled at 130° aTDC to match the exhaust concentration (230 ± 50 ppm). The results are shown in Fig. 6.8. The error bars are primarily due to cycle-to-cycle variations and the attenuation correction; both yield relative standard errors around 10%, except early in the stroke when the latter has a 50% relative uncertainty (see Fig. 6.4). The large “between sprays” concentrations and their errors at 15° and 20° aTDC are due to the large attenuation uncertainty at these crank angles, and not to the raw NO LIF signal as can be seen in Fig. 6.7b.

Interestingly, significant amounts of NO are present in the “through spray” location *before* the heat release rise at 3° aTDC. Moreover, the local temperature reaches 1800 K only around 10° aTDC. This indicates that the thermal (Zeldovich) mechanism for NO creation, requiring temperatures ≥ 1800 K, does not contribute to the early NO formation observed here. This is in contrast to the “between sprays” location, where the first detectable NO (8° aTDC, $T = 2450$ K) can be attributed to the thermal mechanism. However, it should be noted that the temperature measurements from CO₂ and O₂ absorption spectra are unlikely to resolve small, local combustion sites where temperatures may be sufficiently high to enable thermal NO

formation. We have observed luminosity attributed to highly localised combustion spots already at 2–3° aTDC. Our findings of NO formation starting in, or even before, the premixed combustion phase (3° – 7° aTDC as estimated from Fig. 6.2) are in contrast to observations by Dec and Canaan,⁴ who concluded that NO is only created in the mixing-controlled combustion. This discrepancy might be related to attenuation effects, as Dec and Canaan used low-sooting fuels but did not mention corrections for additional attenuation by e.g. CO₂ absorption.

After 30° aTDC, both concentration curves are similar, and from 60° aTDC they decrease only very slowly to an asymptotic value of 230 ppm at 130° aTDC. The fact that the local NO concentration is virtually constant over the last 50° again indicates a homogeneous NO distribution in the measurement cylinder, as also found by Dec and Canaan,⁴ and by Corcione et al..⁵⁴ This justifies our choice of calibration by the exhaust gas concentration. Interestingly, the NO concentration decreases by a factor 5–10 during the later part of the combustion stroke. Although an initial “overshoot” around 20–30° aTDC has been observed^{54, 86} and predicted¹³⁶ for similar diesel engines, the maximum is generally twice the concentration at the end of the stroke, or less. It should be noted, though, that those values are either cylinder averaged concentrations^{54, 136} or gas sampling data,⁸⁶ whereas our probe volume is much more confined. This indicates the localised nature of the NO formation process: only 10–20% of the combustion chamber appears to be involved in the NO formation. Under the assumption that the *major* part of the total NO formed is due to the thermal mechanism, this conclusion is strengthened by the global temperature curve in Fig. 6.5 being much lower than the local ones.

6.6 Conclusions

Conversion of raw NO LIF signals into mole fractions requires knowledge of a number of conditions, such as cylinder pressure, the local temperature, and the attenuation of the light involved in the measurement. The latter can be measured using a combination of experimental techniques.¹⁰⁸ Despite the short path lengths involved in our setup, attenuation effects are considerable, and cannot simply be neglected.

The pressure and temperature dependence of the NO fluorescence leads to variations of over a factor of fifty during the combustion stroke. Optical transmission variations cover a similar range, so that the net post-processing factor for the LIF intensity varies over three orders of magnitude during an engine stroke. The error caused by the assumption of a constant gas composition is (much) less than the

inaccuracy due to uncertainties in the local temperature (and pressure).

Our data provide evidence of highly localised NO formation processes, with peak values around 1500 ppm around 20° aTDC (“through spray”). The first NO signals occur during the premixed burn phase, in contrast to earlier observations by Dec and Canaan.⁴ At this stage, the local temperature is still relatively low (<1800 K at 2–8° aTDC), indicating that the Zeldovich mechanism is not the only process responsible for NO formation. To verify this statement, the local temperature needs to be measured more accurately, and at better spatial resolution, e.g. by means of two-line vibrational thermometry.⁵¹

Acknowledgments

This research is supported by the Technology Foundation STW, applied science division of NWO and the technology programme of the Dutch Ministry of Economic Affairs.

Chapter 7

Diesel combustion: in-cylinder NO concentrations in relation to injection timing*

Abstract

This chapter presents experimental in-cylinder concentrations of nitric oxide, obtained by laser-induced fluorescence measurements in a heavy-duty diesel engine. Quantitative concentration histories during the entire combustion stroke are shown for a number of fuel injection timings. Using images from high-speed combustion visualisation experiments, the presence of the diffusion flame is related to the onset of the NO formation within the laser probe volume. Further attention is paid to the possible NO formation mechanisms. Off-line characterisation of the fuel sprays by means of Schlieren imaging reveals that the initial (premixed) combustion is too fuel-rich for thermal NO formation. Furthermore, the experimental NO concentrations are compared to numerical calculations of the thermal NO formation during the mixing-controlled combustion phase. The agreement between model and experiments suggests that the thermal mechanism is the major NO formation pathway. However, it cannot be excluded that transport of early NO, formed under conditions where the thermal mechanism is ineffective, might be of some importance as well.

*Adapted from: K. Verbiezen, A.J. Donkerbroek, R.J.H. Klein-Douwel, A.P. van Vliet, P.J.M. Frijters, X.L.J. Seijkens, R.S.G. Baert, W.L. Meerts, N.J. Dam, and J.J. ter Meulen, *Combustion and Flame*, submitted (2006)

7.1 Introduction

Despite their superior efficiency and resulting low fuel consumption and CO₂ emissions, diesel engines are notorious for their relatively high emission levels of particulate matter (PM) and NO_x. Optimising the combustion process (i.e. reducing NO_x and PM emissions without serious compromises in fuel consumption and emissions of CO and unburnt hydrocarbons) requires profound knowledge of all formation processes involved. Diesel combustion models need the support from numerical and/or experimental data. Whereas three-dimensional numerical simulations are computationally expensive, if not impossible for extremely complex processes such as diesel combustion, the challenge on the experimental side is to develop reliable measurement techniques.

Here, we focus on the formation of nitric oxide (NO), presenting quantitative, local in-cylinder NO concentration histories as measured by laser-induced fluorescence (LIF) in a DI diesel engine. Although the LIF technique has often been applied for NO measurements in diesel engines,^{2–8} the severe attenuation of the laser beam and the induced fluorescence is not always properly addressed. Exceptions are Stoffels et al.,⁵ who measured spatially resolved laser beam transmission (although no correction was made for the attenuation of the NO fluorescence) and Hildenbrand et al.,⁸ who corrected for the absorption of NO fluorescence by CO₂ (but neglecting additional LIF attenuation caused by e.g. soot, and lacking a correction for laser beam attenuation). Recently we investigated a number of attenuation correction methods, the combination of which yields a complete picture of all major attenuation processes involved in NO LIF measurements in a diesel engine.¹⁰⁸ This detailed correction strategy has allowed for the first time a fully quantitative measurement of the NO concentration in a heavy-duty diesel engine.¹⁰⁹

In this chapter, we present in-cylinder NO concentration histories for a number of fuel injection timings. Although the effect of injection timing on the exhaust NO concentration is well known, quantitative in-cylinder measurements are scarce. In order to interpret our data within the framework of the current ideas on diesel spray combustion,^{18,27,30} a further characterisation of the combustion process is indispensable. In a joint effort of research groups in Nijmegen and Eindhoven, the NO LIF data are complemented by additional experiments including high-speed combustion visualisation (in the same research engine) and Schlieren imaging of the fuel injection (in a high-pressure cell), and by NO chemistry modelling.

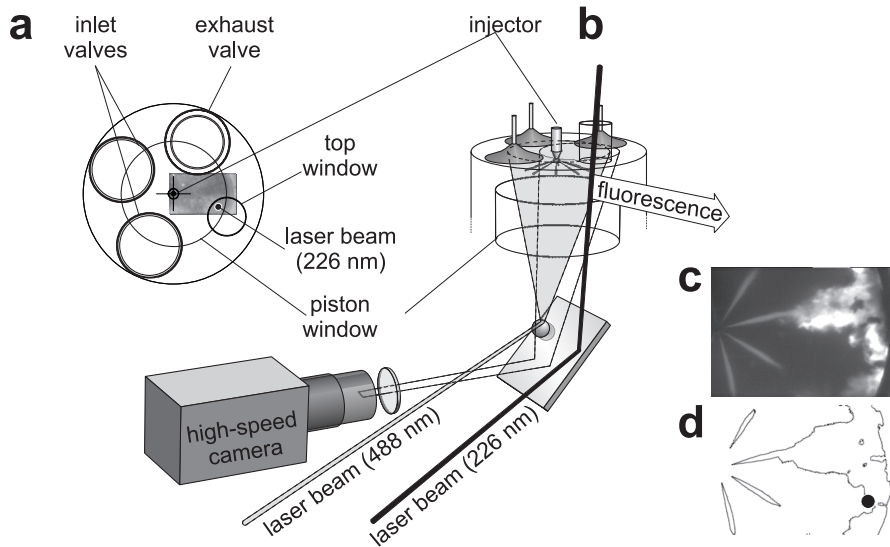


Figure 7.1: Schematic representation of the engine setup: (a) top view, indicating the field of view of the high-speed camera and the NO LIF probe position; (b) three-dimensional view of the measurement cylinder; (c) $23 \mu\text{s}$ snapshot of the combusting fuel sprays, as recorded by the high-speed camera at 6.3° aTDC (start of injection = 8° bTDC); (d) contour plot of the same image, indicating the laser probe location (black dot). The 226-nm laser beam traverses the cylinder almost parallel to its axis. NO fluorescence is detected by an imaging grating spectrograph (not shown) through the nearest side window.

7.2 Experiment

7.2.1 The engine

The research engine is a six-cylinder, heavy-duty diesel truck engine. One of its cylinders (hereafter referred to as “measurement cylinder”) is optically accessible via fused silica windows in the piston (“piston window”), in the cylinder wall (“side windows”), and in the cylinder head (“top window”). A slot machined into the piston crown prevents blocking of the detection side window around Top Dead Centre (TDC). The measurement cylinder is depicted schematically in Fig. 7.1, and its most relevant specifications are compiled in Table 7.1. For measurements of the cylinder pressure, the top window can be replaced by a pressure transducer (AVL QHC32). An eight-hole fuel injector is mounted centrally, and can be rotated for easy alignment of the fuel spray with respect to the laser probe volume. Fuel injection

Table 7.1: Specifications and global operating conditions of the measurement cylinder.

engine type	six-cylinder four-stroke DI diesel engine
bore, stroke	130 mm, 146 mm
displacement	1.939 ℓ (per cylinder)
compression ratio	15 (unmodified: 16)
piston bowl shape	“bath tub” (flat piston window)
∅ piston bowl	84 mm
swirl number	1.8
∅ injector; # holes	0.128 mm; 8
fuel injected; inj. pressure	60 mg of low-sulphur diesel; 1200 bar
boost pressure	1.4 bar (abs.; no EGR)
engine speed	1430 rpm

into the measurement cylinder is provided by a home-built common-rail system. The start and end of the injection can be set independently via the electronically actuated injector, each injection yielding 60 mg at 1200 bar. Figure 7.2 shows the rail pressure during an injection event. During the injection, the pressure varies by $\sim 12\%$. The electronics also allow for a double (split) fuel injection (see Appendix I). The oil-free measurement cylinder is skip-fired (1:35) to avoid overheating; three unmodified cylinders are continuously fuelled (by the original line-pump) to maintain engine speed.

Measurements were conducted with a rail pressure of 1200 bar and at four different fuel injection timings, actuating the fuel injector at 18° , 13° , 8° , and 3° bTDC (bTDC = before TDC). The *effective* start of injection (Sol_{eff}) was determined from high-speed imaging (see Section 7.2.2) and occurs about 3° later; see Table 7.2 for details. Unless explicitly stated otherwise, Sol means the *nominal* start of injection (i.e. actuation of the injection system). The start of combustion was retrieved from the cylinder pressure trace and the derived rate of heat release,²⁹ shown in Fig. 7.3.

7.2.2 High-speed combustion visualisation

The combustion process was recorded through the piston window by a high-speed camera (Phantom V7.1, 160 kHz maximum frame rate), see Fig. 7.1. In order to visualise the fuel sprays prior to combustion, a continuous-wave Argon ion laser

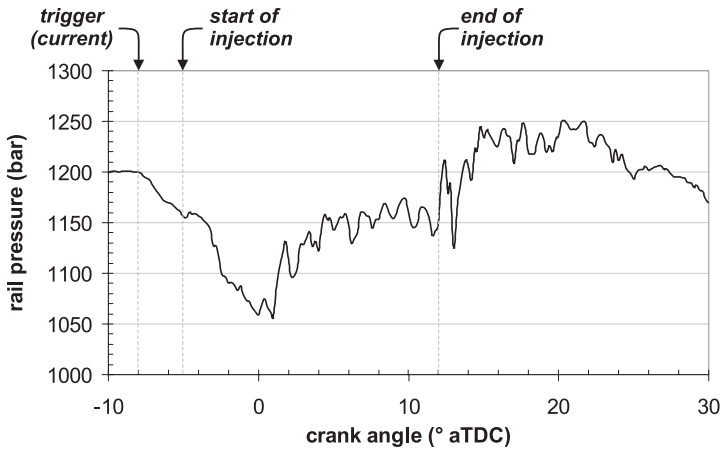


Figure 7.2: Typical injection pressure trace for the engine experiments. For the data shown here, the injector is actuated at 8° bTDC, as is indicated by the arrow. The actual start and the end of injection are indicated as well.

beam (Spectra Physics, Stabilite 2016) of circa 5 W (operating primarily at 488 and 517 nm) was directed towards a 16-mm diameter metal sphere located below the piston window, resulting in a highly divergent reflection illuminating almost the entire combustion chamber. In order to avoid overexposure of the camera and to suppress the combustion light, a filter combination (BG 18 and GG 475 Schott filters) was used, transmitting roughly between 460 and 640 nm. The camera was synchronised to the crank shaft of the engine and recorded one image every 0.3° CA ($\sim 35 \mu\text{s}$), with an exposure time of $23 \mu\text{s}$, and a resolution of $275 \mu\text{m}$ per pixel.

7.2.3 Fuel spray imaging

The laser elastic scattering measurements merely visualise the liquid phase of the spray (including droplets). Additional off-line experiments involving Schlieren imaging were carried out to image the fuel vapour as well. The Schlieren technique is particularly sensitive to variations in the index of refraction, and hence, to density gradients, which allows a better characterisation of the spray geometry. These measurements were performed in the Eindhoven high-pressure, high-temperature cell (EHPC) using the same injector type and rail pressure as in the engine experiments. A schematic representation of the Schlieren setup is shown in Fig. 7.4.

Vaporising conditions (30.9 bar and 770 K) were realised by igniting a com-

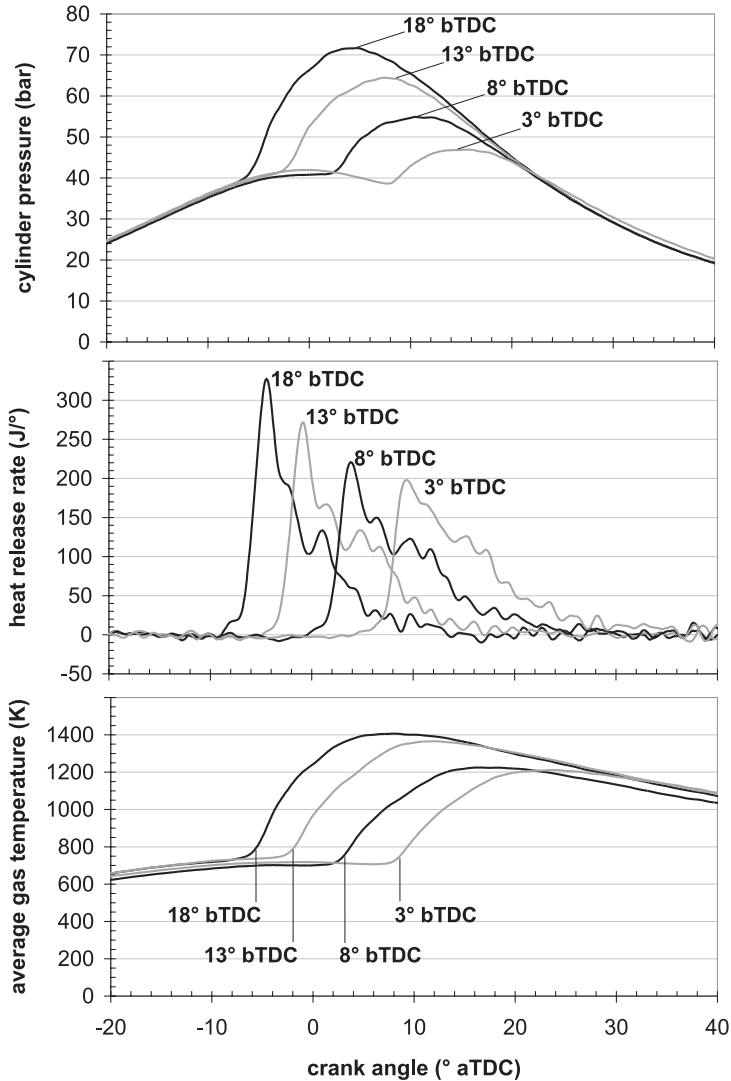


Figure 7.3: Cylinder pressure (top), rate of heat release (middle), and average gas temperature (bottom) for the four injection timings. The nominal start of injection is indicated for each curve.

bustable mixture 2500 ms prior to the fuel injection. After this precombustion, an inert, hot gas mixture (N_2 , CO_2 , and H_2O) with a density of 14 kg/m^3 remains. In addition, multiple series of injection events were visualised in a colder (473 K) inert

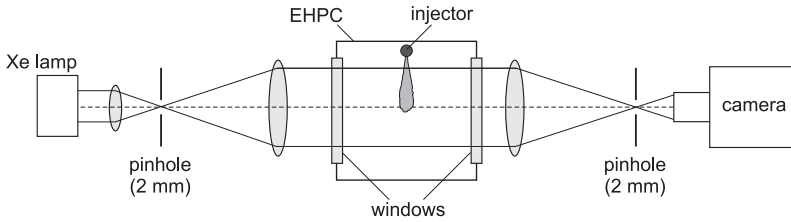


Figure 7.4: The Schlieren imaging setup including the Eindhoven high-pressure, high-temperature cell (EHPC).

ambient gas. Various ambient densities ($15\text{--}25\text{ kg/m}^3$) were studied, covering the range found in the engine tests. These tests furthermore showed that the sprays from different nozzle holes were very similar, as was also confirmed by the high-speed visualisation experiments on the test engine. Further details of the EHPC can be found in Refs. 137 and 138.

For these measurements the same Phantom camera was used, operating at 60.7 kHz , with an exposure time of $2\ \mu\text{s}$, and a resolution of $430\ \mu\text{m}$ per pixel.

7.2.4 NO LIF measurements

The laser beam for NO excitation traverses the combustion chamber (almost) vertically, 30 mm away from the injector, and rotated over 26° in the swirl direction with respect to a fuel spray. The trajectory of the laser beam is shown in Fig. 7.1. The height of the probe volume is limited to the uppermost 23 mm of the combustion chamber by the size of the detection window.

NO LIF is induced by laser radiation at 226.03 nm , resonant with the coinciding $A^2\Sigma(v' = 0) \leftarrow X^2\Pi(v'' = 0)$ $P_1(23.5)$, $Q_1 + P_{21}(14.5)$, and $Q_2 + R_{12}(20.5)$ transitions. This excitation wavelength was suggested by DiRosa et al. for high sensitivity and minimal O_2 LIF interference even at elevated pressures.⁶² Laser radiation (pulses of $5\text{--}8\text{ mJ}$) is produced by a frequency-mixed dye laser (Radiant Narrowscan D) pumped by a Nd:YAG laser (Continuum Powerlite Precision II 8010). Four vibronic fluorescence bands (at 237 , 248 , 259 , and 270 nm , corresponding to the $A \rightarrow X(0,1) - (0,4)$ transitions, respectively) are detected through the nearest side window by an intensified CCD camera (Roper Scientific, ICCD 512T, 512^2 pixels, 16 bits) mounted behind a spectrograph (ARC SpectraPro 500i, 600 lines/mm grating). The entrance slit of the spectrograph is parallel to the laser beam direction, and opened to encompass the entire laser beam width for maximum intensity. Two typical raw NO LIF images are shown in Fig. 7.5.

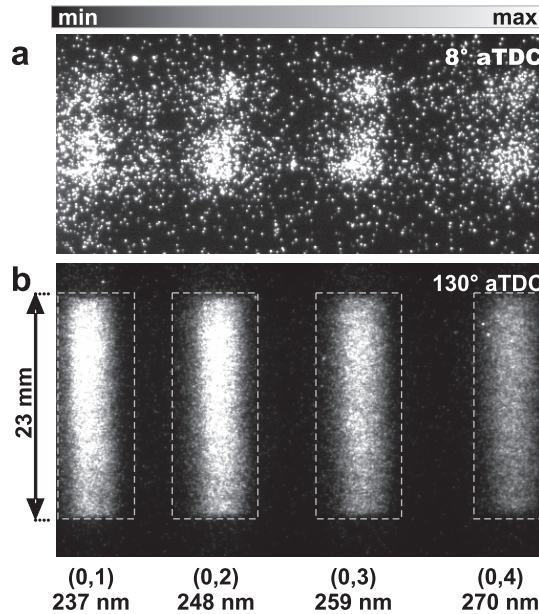


Figure 7.5: Two single-shot NO LIF images recorded through the side window by the spectrograph-camera system, at 8° aTDC (a) and 130° aTDC (b). The intensity scales are adjusted individually to show maximum contrast in each image. Start of injection: 8° bTDC.

Attenuation effects are minimised (but not negligible, see Appendix II) by keeping the in-cylinder path lengths of laser beam and fluorescence as short as possible (0–23 and 37 mm, respectively).

7.2.5 NO LIF data processing

In the current analysis, the total NO LIF intensity per vibronic emission band is determined by summing all relevant pixel intensities (areas indicated by dashed lines in Fig. 7.5b). Consequently, the data represent the average NO density within the probe volume ($\varnothing 4$ mm, height: 23 mm).

Attenuation corrections

We have measured in-cylinder attenuation coefficients by means of (1) bidirectional LIF, and (2) absorption spectroscopy of CO₂ and O₂. With bidirectional LIF, vertical NO LIF intensity profiles are measured for two opposite directions of the excitation

laser beam; the spatially resolved laser beam transmission is calculated from the ratio of these profiles.^{90,114,122,123} For a single-shot approach, the two counter-propagating laser pulses should be fired quasi-simultaneously. Here, all pulses are fired during different cycles, and thus we obtain averaged transmission data.

The attenuation of the NO fluorescence caused by absorption by CO₂ and O₂ can be obtained by comparing each measured NO LIF spectrum to a reference NO LIF spectrum (i.e. without absorption). The ratio of these spectra yields a relative transmission spectrum of the NO fluorescence on its way to the detector. Absolute transmission values are obtained by fitting this transmission spectrum, using parameterised CO₂¹⁰⁰ and O₂¹²¹ absorption cross sections. Due to the strong temperature dependence of the CO₂ and O₂ absorption cross sections, each fit also yields an estimate of the local temperature*.¹³⁵ The additional attenuation of the NO fluorescence by e.g. soot is estimated by comparing the calculated CO₂ and O₂ absorption (at 226 nm) to the (total) laser beam extinction as measured with bidirectional LIF.

We refer to Refs. 108 and 109 for a more complete description of these techniques and methodology. Both of the above-mentioned techniques have the advantage that they are performed simultaneously with the actual NO LIF measurements. Consequently, all measurements were carried out under identical conditions. Transmission curves for the laser beam and the fluorescence are presented in Appendix II.

Pressure and temperature dependence

We have used LIFSim⁶⁴ to calculate the pressure and temperature dependence of the NO LIF intensity. Although the gas composition may have a large influence on the quenching rates and thus on the *absolute* LIF intensity, here we are only interested in the *relative* changes of the LIF signal (absolute values are obtained by calibration, see next paragraph). We have demonstrated previously that the exact gas composition is of minor importance,¹⁰⁹ and all LIFSim calculations were performed for constant ([O₂]:[N₂] = 1:4) composition of the in-cylinder gases. Further input parameters were the cylinder pressure and the local temperature. The latter was estimated from the observed CO₂ and O₂ absorption spectra (previous paragraph).

*In fact, the fitted temperature is a weighted average of the temperature profile along the trajectory of the NO fluorescence. This effective temperature is expected to be strongly biased to the probe volume temperature.¹³⁵

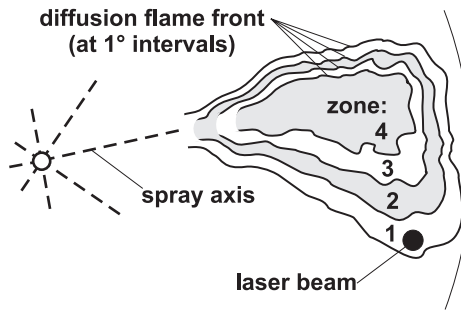


Figure 7.6: Schematic representation of the combustion zones (numbered 1–4). The flame front is represented by solid lines; dashed lines indicate the spray axes; the position of the NO excitation laser beam is indicated by the black dot.

Calibration

After correcting the NO LIF data for attenuation effects and for the pressure and temperature dependence of the fluorescence yield, the processed data are multiplied by a calibration factor that scales the in-cylinder concentration at the end of the stroke (the exhaust valve opens at 130° aTDC) to the exhaust NO concentration. The latter is determined by a commercial exhaust gas analyser (SIGNAL Instruments, NOX analyser series 4000), sampling the exhaust of only the measurement cylinder. Its reading is scaled by the skip-fire ratio and an additional factor accounting for the fact that the sampling occurs non-isokinetically (see Chapter 2.5). We assume homogeneous NO distributions at 130° aTDC.

7.2.6 NO formation calculations

The thermal NO formation has been calculated using the extended Zeldovich mechanism. For the calculations, the combustion event is divided into steps of 1° CA, during which a certain amount of fuel is burnt. This divides the flame spatially into zones. Each zone starts in the volume traversed by the flame front during the corresponding step of 1° . Subsequently, the zone moves outward as new zones are formed at the flame front during the following crank angle steps. This is shown schematically in Fig. 7.6. The calculations are based on the assumption that no mixing occurs between different zones; entrainment of fresh air into a zone, however, is modelled based on the spray model by Naber and Siebers.¹⁸ A chemical equilibrium solver¹³⁹ is used to calculate the composition of the combustion products and the corresponding adiabatic flame temperature. The latter is then used to calculate the

thermally formed NO per zone. These calculations are detailed below.

The amount of fuel burnt in each zone (i.e. during 1°) is determined from the rate of heat release (Fig. 7.3). Only the mixing-controlled part of the combustion is considered (the premixed combustion is too fuel-rich for significant thermal NO formation, as will be discussed in Section 7.3.2). It is assumed that the combustion in each zone starts under stoichiometric conditions, which is a reasonable assumption for the diffusion flame. For each zone, the initial composition is now known. Its temperature is taken equal to the unburnt mixture temperature, and is used as an input to a chemical equilibrium solver to determine the composition of the combustion products and the corresponding adiabatic flame temperature. Species considered are: O_2 , N_2 , CO_2 , H_2O , CO , H_2 , OH , O , and H . In all zones, the pressure is equal to the measured in-cylinder pressure (Fig. 7.3).

With the adiabatic flame temperature and the O , O_2 , N , OH and H concentrations the NO formation rate is calculated by means of the extended Zeldovich mechanism. The main equations are:

$$\frac{d[N]}{dt} \approx 0; \quad (7.1)$$

$$\frac{d[NO]}{dt} = 2k_{1,r}[O][N_2] - 2k_{1,l}[NO][N]; \quad (7.2)$$

$$[N] = \frac{k_{1,r}[O][N_2] + k_{2,l}[NO][O] + k_{3,l}[NO][H]}{k_{1,l}[NO] + k_{2,r}[O_2] + k_{3,r}[OH]}. \quad (7.3)$$

The reaction rate constants k are taken from GRI 3.0.¹⁴⁰ The zone temperature is initially equal to the adiabatic flame temperature, but it quickly decreases due to mixing with colder unburnt air, and due to expansion of the cylinder volume. The resulting shift in the chemical equilibrium, influencing the NO formation rate, is included in the calculations. The computation of NO formation is stopped when the temperature of the zone drops below 1700 K, which is often used as a cut-off temperature for thermal NO formation.

7.3 Results and discussion

7.3.1 Engine characteristics

Table 7.2 summarises the operating points that were used in this study. The effective start and end of injection were determined from the combustion movies measured in the engine. The start of combustion has been derived from the heat release curves in Fig. 7.3. The exhaust NO concentration levels are indicated as well.

Table 7.2: Operating points of the measurement cylinder. All crank angles in ° aTDC (aTDC = after TDC; Sol = start of injection; Eol = end of injection; SoC = start of combustion).

Sol (nominal)	-18.0°	-13.0°	-8.0°	-3.0°
Sol _{eff} (effective)	-14.8°	-9.3°	-4.5°	0.3°
Eol	0.6°	6.0°	11.1°	15.8°
SoC	-8.9°	-5.5°	0.4°	4.2°
inj. duration	15.3°	15.3°	15.6°	15.5°
ignition delay	5.9°	3.8°	4.1°	3.9°
gIMEP (kPa)	502 ± 6	509 ± 4	496 ± 11	498 ± 1
[NO] _{exhaust} (ppm)	560 ± 112	402 ± 80	272 ± 55	190 ± 38

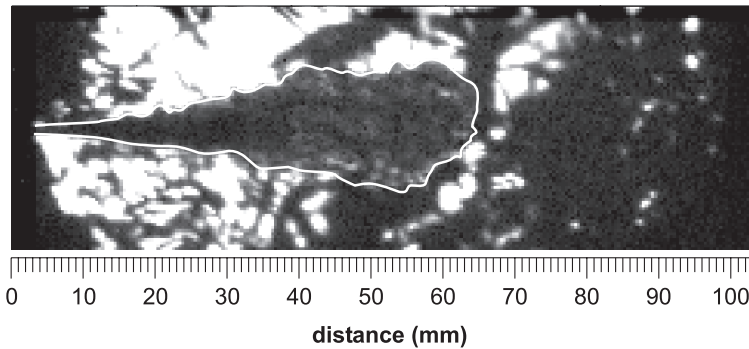


Figure 7.7: Single frame from a high-speed Schlieren movie of a single fuel injection into the EHPC, at 770 K and 30.9 bar. The white contour guides the eye.

7.3.2 Fuel spray characterisation

Time-resolved (vapour) spray penetration was measured in the EHPC by means of high-speed Schlieren imaging. A typical frame taken from the high-speed movie is shown in Fig. 7.7. The strong background density fluctuations are a consequence of the precombustion. They move much slower than the fuel jet, and in the analysis they are dealt with by interpolating the spray edge across each “dark spot”, in order to obtain a reliable measure for the spray angle and penetration depth. Based on these results, the average spray full angle was evaluated as $\theta_{\text{spray}} = 18^\circ$. Following the approach by Naber and Siebers, for a given spray angle, the penetration length

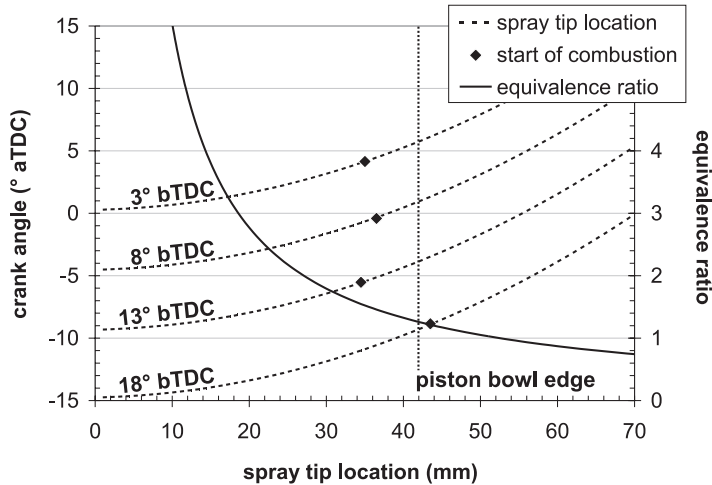


Figure 7.8: Relation between spray penetration and crank angle, and equivalence ratio as a function spray tip location. The start of injection is indicated in each penetration curve, as well as the piston bowl diameter.

can be correlated to the average equivalence ratio (mass averaged value across the spray cross sectional area) at the spray tip.¹⁸ For a quasi-steady spray this penetration curve also corresponds to the variation of this average equivalence ratio with the distance from the injector. Both the spray penetration and the corresponding equivalence ratio are shown in Fig. 7.8 for the four injection timings we investigated. For each curve the start of combustion is indicated as well, revealing that on average the jet is rather fuel-rich when the mixture ignites: $\Phi \approx 1.5$ for all curves except the one for 18° bTDC when $\Phi \approx 1.2$.

The relatively high equivalence ratios at the start of combustion suggest that the initial, premixed combustion is too fuel-rich for significant thermal NO formation to take place, as the latter requires near stoichiometric equivalence ratios ($0.8 \leq \Phi \leq 1.0$)³¹. Prompt NO formation, however, may occur in rich zones with equivalence ratios up to $\Phi \approx 1.8$, and may play some role in the observed NO concentrations.

Figure 7.8 also indicates that the combustion starts with the spray tip close to the piston bowl rim. For the injection at 18° bTDC, the jet has just reached the bowl when ignition occurs, whereas for the other injection timings the spray tip is still 6–7 mm away. This is in agreement with the high-speed combustion movies showing the first combustion luminosity (i.e. soot incandescence) at the edges of the piston window.

7.3.3 NO LIF measurements

The *in-cylinder* NO concentrations are shown in Fig. 7.9 as a function of crank angle and injection timing. Similar to the exhaust concentration, the in-cylinder NO concentration increases almost linearly when advancing the fuel injection. All NO curves have very similar shapes, varying only in the moment of first NO, and in amplitude. The peak concentrations range from 1500 ppm (Sol = 3° bTDC) to values just over 5000 ppm (Sol = 18° bTDC). Typically, the peak concentration is approximately nine times higher than the asymptotic value reached by 130° aTDC.

Generally, the first significant NO LIF appears $\sim 5^\circ$ after the start of combustion. Given the fact that (1) the initial, premixed combustion takes place within the fuel spray boundaries²⁷ and that (2) the laser beam is 14 mm away from the spray axis, the probe location may be too far away to detect any (prompt) NO formed during the initial premixed combustion, unless this prompt NO is convected towards the probe location. Such transport cannot be excluded; with a swirl ratio of 1.8 this would require 5–7°, which is only slightly longer than the observed delay of 5°. Nevertheless, in the latter case a considerable dilution of the transported NO would be expected.

On the other hand, the high-speed combustion movies show that the moment when the first NO is detected coincides within 0.5° CA with the moment when luminous soot* is first observed at the probe location. This is shown in Fig. 7.10. The first appearance of the diffusion flame in the probe volume is also indicated in Fig. 7.9. This implies that the observed NO is (primarily) due to the thermal NO formation mechanism; the arrival of the diffusion flame at the probe location quickly raises the local temperature above the threshold for thermal NO formation (1700–1800 K), leading to a sudden increase of the NO concentration, in agreement with the NO LIF results. The sudden temperature increase is confirmed by experimental temperature values derived from CO₂ absorption spectra, shown in Fig. 7.11.

From 40° aTDC onwards, all NO concentration curves decay at the same rate. This is illustrated in Fig. 7.12, where all curves are normalised at 130° aTDC. By 40° aTDC the combustion has ceased for all four injection timings. Moreover, the local temperature has dropped below 1800 K, and no significant NO formation is to be expected. As a consequence, the concentration decay is attributed to mixing of the combustion products with unburnt gases, until a stable value is reached. This process is identical for all four experimental conditions.

*According to Dec's conceptual model, the luminous soot is representative for the diffusion flame.²⁷

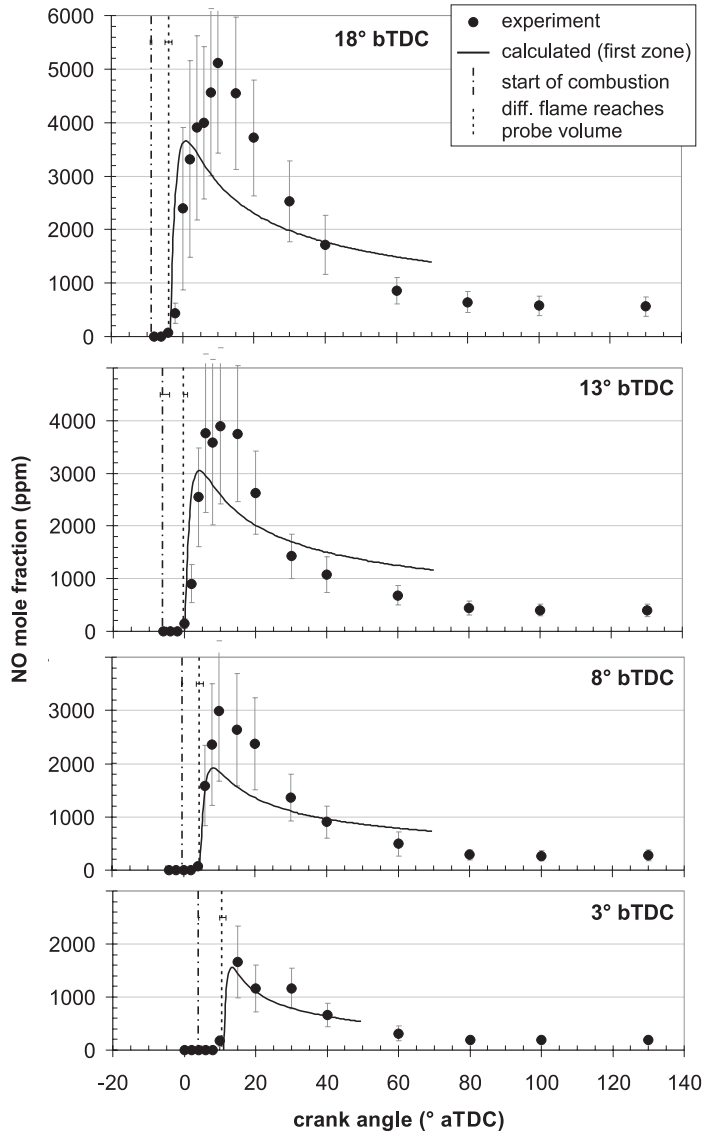


Figure 7.9: Local NO mole fractions as a function crank angle and injection timing. The error bars contain cyclic variations as well as the uncertainties in all processing steps (attenuation correction and p,T dependence). The solid curves are explained in Section 7.3.4.

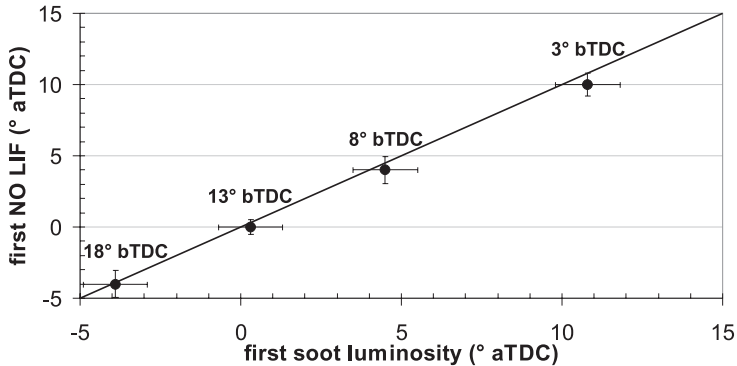


Figure 7.10: The moment of first detected NO *versus* the moment of first soot luminosity in the probe volume. The straight line assumes equal moments of first NO LIF and first soot luminosity.

7.3.4 Calculated NO formation

Figure 7.13 demonstrates that the NO formation calculations are in reasonable agreement with the exhaust concentration measurements. Figure 7.14 shows the calculated NO molar fraction in all product zones as a function of crank angle. The first zone is formed when the premixed burn spike of the heat release rate has its maximum, which is a crude estimate of the onset of the diffusion flame (according to the combustion movies, the luminous diffusion flame appears even 1–2° CA earlier). Every following 1.0°, a new product zone is formed. The observed decrease in the NO concentration per zone is caused by (1) a shifting of the H-C-O equilibrium as a result of the varying temperature and leading to destruction of some of the earlier formed NO, and (2) by diluting the zone with newly entrained fresh air.

For all four data sets, the start of the first zone is very close to the moment the diffusion flame appears in the laser probe volume. For instance, for the Sol = 18° bTDC measurements, the first zone starts at 3.5° bTDC, as compared to 3.9° bTDC for the appearance of the flame; for the Sol = 8° bTDC series these values are both 4.5° aTDC. Therefore, in line with the earlier observations (Section 7.3.3), the first zones are considered representative for the initial part of the experimental concentration curve. In reality, of course, the probe volume will see a mixture of such zones.

For Sol = 18° bTDC, a peak concentration around 3600 ppm is calculated, in reasonable agreement with the experimental 5100 ± 1700 ppm. The agreement

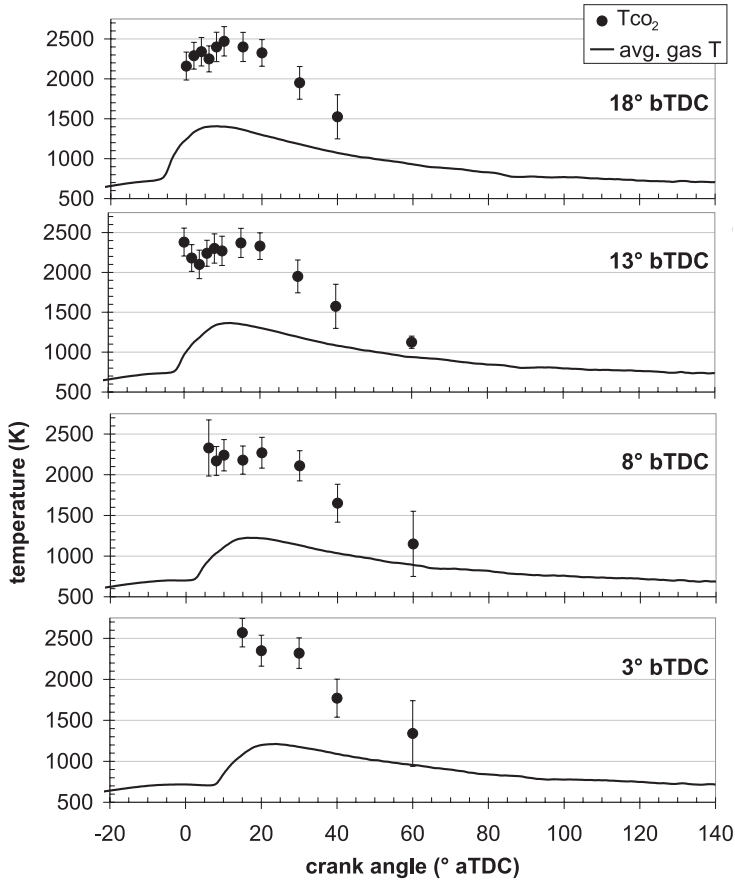


Figure 7.11: Local temperatures, based on CO_2 and O_2 absorption spectra. The average gas temperature is shown for comparison.

between experiment and calculation is of similar quality for the other injection timings. The calculated NO concentration of the first zone is also shown in Fig. 7.9 for easy comparison of the peak values. The difference in the decay rate between experimental and numerical concentration histories might be related to the fact that the zones move past the probe volume, so that the first zone is only representative for the initial part of the measured concentration history. Another explanation might be the air entrainment model: the model by Naber and Siebers is only applicable to a quasi-steady spray, and will only be an approximation of the mixing processes in the diffusion flame.

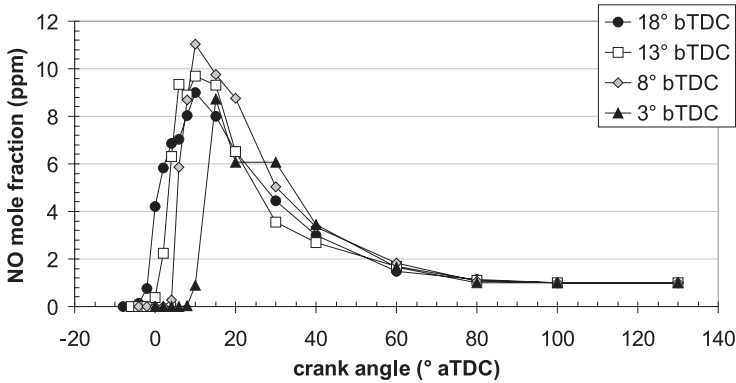


Figure 7.12: Normalised NO mole fractions during the combustion stroke, based on the data in Fig. 7.9.

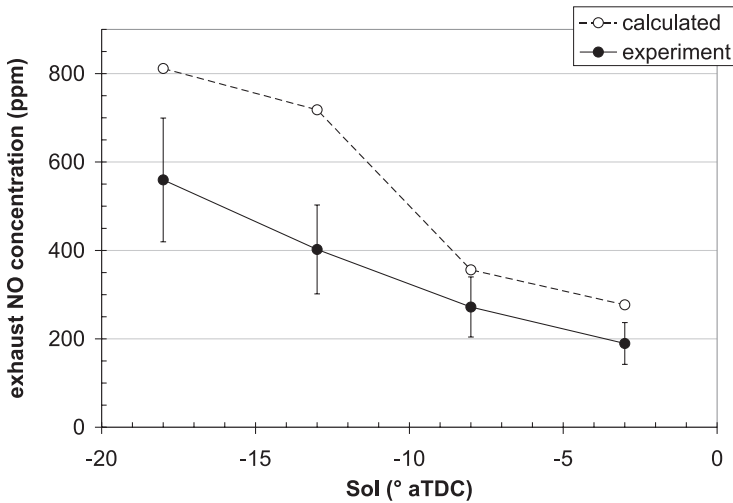


Figure 7.13: Calculated and experimental exhaust NO concentration versus Sol.

The calculations show that once the diffusion flame has arrived at the probe volume, *local* thermal NO formation is fast enough to account for a significant fraction of the observed NO. Since the observed NO concentrations are nevertheless systematically higher than the calculated ones, it cannot be excluded that transport of earlier formed NO (not modelled) might play a role as well.

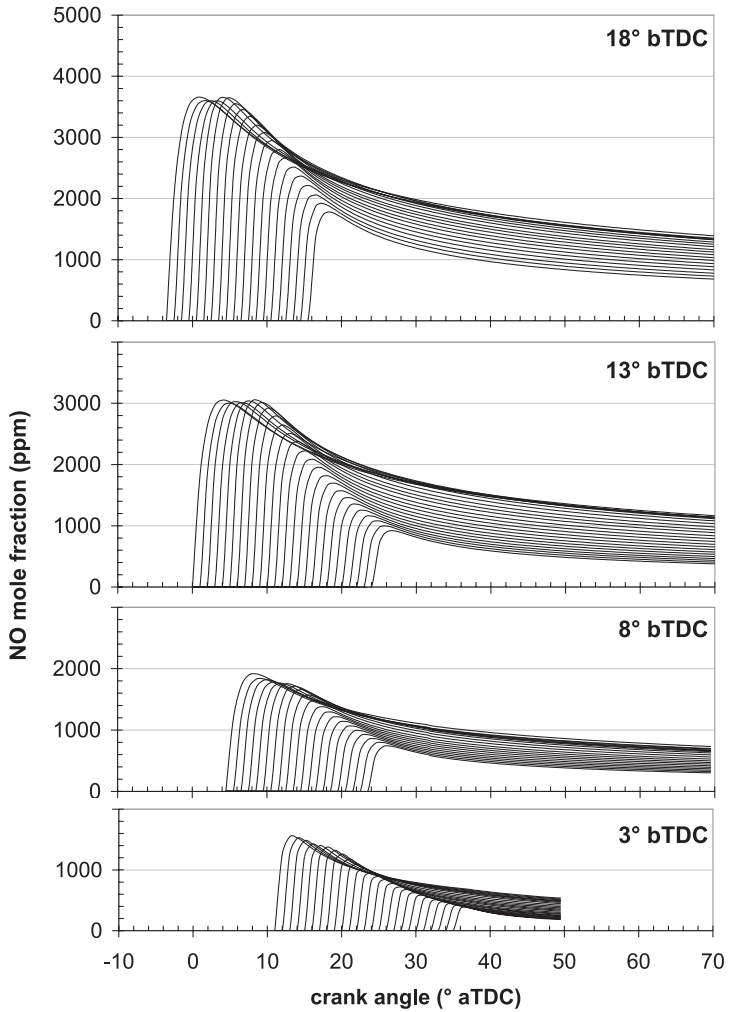


Figure 7.14: NO concentration in each product zone *versus* crank angle.

7.4 Summary and conclusions

We have presented local in-cylinder NO concentration histories, both measured and calculated, for various injection timings in a diesel engine. Based on a combination of these data with additional experiments, such as high-speed visualisation of the combustion and Schlieren imaging of the fuel spray, we feel it justified to draw the following conclusions.

The well-known trend of increasing exhaust NO emissions with advancing injection timing is also reflected in the in-cylinder concentration histories. In fact, all concentration histories are quite similar, varying only in onset and peak amplitude. In each case, the maximum concentration in the probe volume is around nine times the concentration reached by the end of the stroke. Apparently, only a small part of the combustion chamber is responsible for the bulk of the NO that is produced. This is of course in line with the engine operating at low load during the experiments, resulting in a low (overall) equivalence ratio.

The same NO vs. Sol trend is observed in our numerical data. The agreement between experiment and calculation is qualitatively good, but the experimental values are systematically somewhat higher. This suggests that the observed NO is largely caused by *local* thermal NO formation rather than transport. However, it cannot be excluded that NO formed during the premixed combustion is transported towards the probe location. The time needed for this transport is very close to the observed delay between the start of combustion and the first NO LIF appearance, suggesting that the prompt and/or N₂O mechanisms may indeed contribute to the observed local NO concentrations.

Our present data do not allow an accurate investigation of the prompt NO mechanism. The data in Fig. 7.8 show that the initial combustion is too fuel rich for significant thermal NO formation. Therefore, further in-cylinder NO LIF experiments, moving the probe volume towards the premixed burn region and combined with more accurate local temperature measurements (e.g. by vibrational thermometry⁵¹), would be elucidating. Thus far, measurements with the laser beam directed through a fuel spray suffered from severe window fouling, and the current probe location was preferred for further experiments. Previous “through spray” NO LIF measurements in the same research engine,¹⁰⁹ but with the original cam-driven fuel injection, showed significant NO fluorescence during the premixed burn phase, at temperatures too low for thermal NO formation.

All concentration curves decay at the same rate from 40° aTDC onwards. This is attributed to transport/mixing, since by that time the combustion has finished

and local temperatures are too low for significant thermal NO formation. This is also confirmed by the calculations, that show a constant NO mass after 40° aTDC. Considering the large impact of transport on the local NO concentration, a more detailed comparison of experimental and numerical data will only be possible either by (1) by extending the fluid dynamics of the numerical simulations, or (2) by two-dimensional LIF imaging of a larger fraction of the combustion chamber, measuring the total NO density.⁴ The latter would require two-dimensional attenuation corrections as well as a local temperature map, two issues that will bring new experimental challenges.

Acknowledgements

This research is supported by the Technology Foundation STW, applied science division of NWO and the technology programme of the Dutch Ministry of Economic Affairs.

Appendix I: split fuel injection

In addition to the four injection strategies, the effect of a split fuel injection was investigated as well. For the latter, 30 mg of fuel was injected twice, at 18° bTDC and at 8° bTDC, leaving ~5° between the two injections.

Figure 7.15 shows that the maximum rate of heat release is significantly reduced by the split injection. Due to the increased entrainment of fresh air, and due to cooling by the late, second injection, the combustion temperatures are lower, and as a result the thermal NO formation is reduced. This was also observed experimentally, the exhaust NO concentration being reduced from 560 ppm (single injection at 18° bTDC) to 412±80 ppm. The in-cylinder concentrations are shown in Fig. 7.16. The concentration history for the single injection at 18° bTDC is shown for comparison.

Interestingly, the peak concentration is only ~5 times higher than the final concentration, as opposed to the factor nine for the single injections. This is most likely a consequence of the improved air entrainment (during combustion), lowering the peak temperatures and diluting the combustion products. After 40° aTDC, when the combustion has ended, the concentration history follows the same decay as the histories for the single injections.

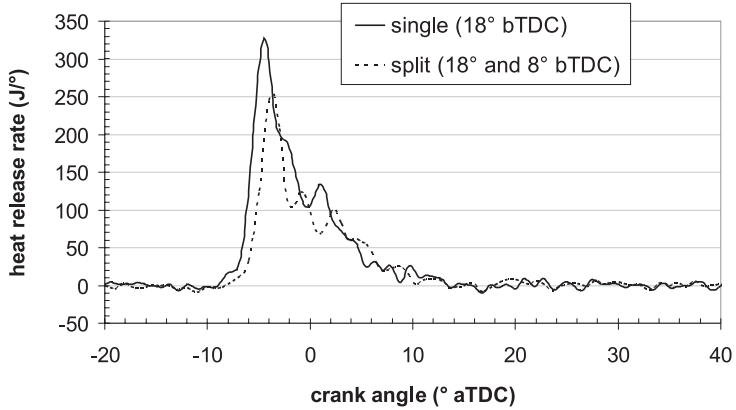


Figure 7.15: Rate of heat release for a single (Sol = 18° bTDC) and a split fuel injection (Sol₁ = 18° bTDC, Sol₂ = 8° bTDC).

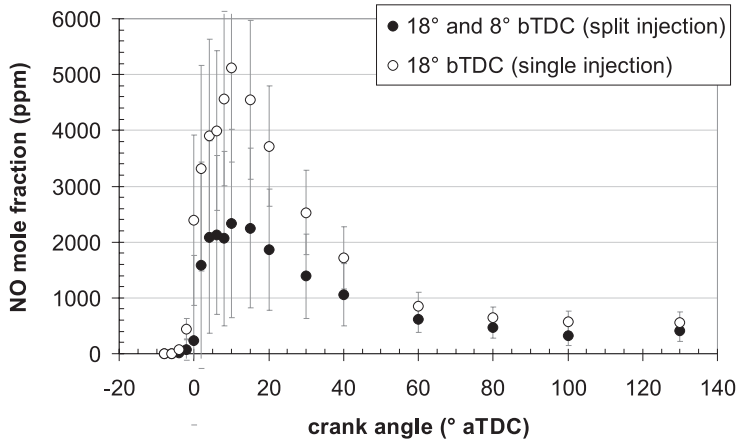


Figure 7.16: Local NO mole fractions during the combustion stroke, for single and split injections. The start of each injection is indicated in the upper right corner.

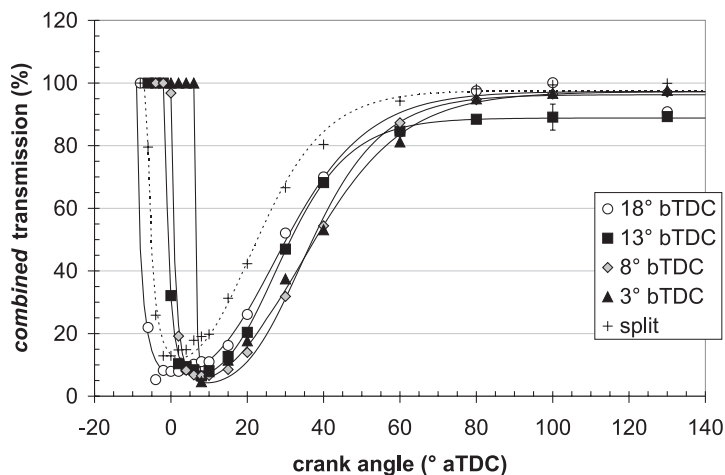


Figure 7.17: Combined transmission curves for all injection settings. Lines guide the eye.

Appendix II: laser beam and fluorescence transmission

Figure 7.17 shows the product of the laser beam transmission and the NO LIF transmission (“combined transmission”) for all five injection strategies. Comparing the single injections, there is only a slight decrease in the transmission minimum when retarding the fuel injection, with the possible exception of the Sol = 3° bTDC data series. (Note that the relatively low signal-to-noise levels of the Sol = 3° bTDC measurements lead to a larger error in the derived attenuation coefficients for that data series.)

As is shown in Fig. 7.18, the attenuation caused by UV absorption by hot CO₂ and O₂ clearly decreases for later injection timings, as would be expected because of the lower combustion temperatures. However, the attenuation attributed to soot was observed to increase with retarding injection timing, in agreement with the expected increase in soot formation. These two trends largely cancel, and cause a slightly increasing overall attenuation with increasing injection timing.

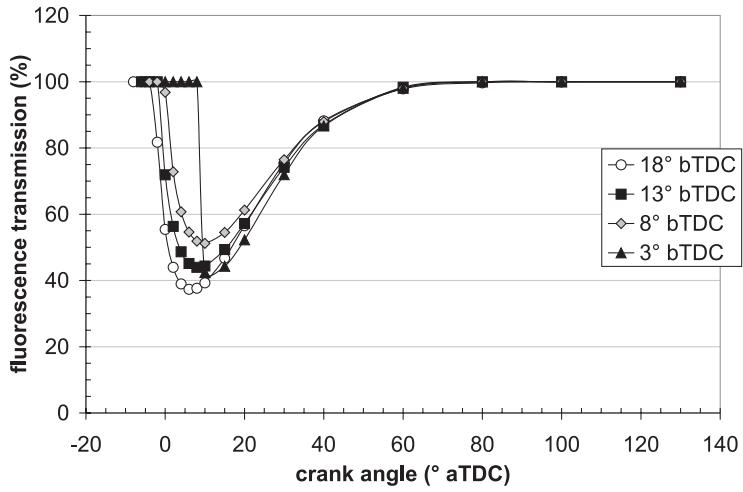


Figure 7.18: Transmission of the NO fluorescence through hot CO₂ and O₂, for all single injections. Lines guide the eye.

Chapter 8

Summary and outlook

8.1 Summary

Despite the diesel engine's popularity, its emission of high levels of nitric oxide (NO) is problematic. Reacting into NO_2 in the atmosphere, NO indirectly causes acid rain and — in high concentrations — it contributes to smog formation. In order to cope with the increasingly stringent legislation on pollutant emissions from engines, a profound understanding of the combustion process is required. The formation mechanisms of NO are not entirely understood, and accurate, quantitative experiments are necessary to provide new insights and to validate existing models. Unfortunately, reliable techniques for in-cylinder NO concentration measurements are scarce.

The research presented in this thesis is dedicated to the development of the laser-induced fluorescence technique to a level at which quantitative, in-cylinder NO concentration measurements can be realised in a heavy-duty diesel engine. As is discussed in Chapters 3 and 6, the NO LIF intensity is in principle linearly proportional to both the *local* laser intensity and the local NO number density. However, the severe (but unknown) attenuation of both the laser beam and the induced fluorescence in the combustion chamber affects the detected fluorescence intensity. Besides, the fluorescence yield per NO molecule strongly depends on the cylinder pressure and temperature — two parameters that are far from constant during engine operation.

After a quick introduction to diesel engines (Chapter 1) and especially the research engine (Chapter 2), the laser-induced fluorescence technique is discussed in some detail in Chapter 3. Chapter 3 furthermore gives an overview of common

and less common excitation-detection schemes applied in engine research. Various spectroscopic aspects that contribute to the pressure and temperature dependence of the fluorescence yield are discussed and modelled; by combining these models a full spectroscopic model is obtained.

As already mentioned, attenuation effects can be rather severe for *in situ* spectroscopic measurements, and they have been the main research focus of this thesis. In-cylinder attenuation is primarily caused by absorption and scattering by soot particles and fuel droplets, and by absorption by poly-aromatic hydrocarbons (PAHs), hot O₂, and hot combustion products like CO₂ and H₂O. Chapter 4 discusses the possibility of UV absorption by hot O₂. Its effect on the attenuation of the NO fluorescence bands is similar to, and easily confused with, that of hot CO₂, although the O₂ absorption cross section exhibits a more pronounced dependence on wavelength and temperature. Especially for shorter wavelengths ($\lambda \leq 237$ nm), absorption by O₂ was found to be comparable to that by CO₂.

In Chapter 5 a number of (laser) techniques are presented that each assess a part of the total attenuation experienced by the laser beam and the fluorescence. It is concluded that the total attenuation can only be retrieved by combining multiple techniques. An important observation is that the strong temperature dependence of the CO₂ and O₂ absorption spectra can be used to derive the local temperature. This dependence is well known, so that measured absorption spectra yield both a correction for the attenuation and an estimate of the temperature. The latter is an important input parameter for calculating the fluorescence yield, as is mentioned above, and it has been used as an input parameter for the spectroscopic model (Chapter 3).

The attenuation measurements demonstrate that, during the combustion stroke, the combined transmission of the laser beam and the NO fluorescence decreases from initially 100% (i.e. before fuel injection) to ~2%, recovering later to 85% at the end of the stroke. Furthermore, three popular excitation-detection schemes for NO LIF are compared in terms of attenuation, using the experimental transmission spectra from the research engine, and in terms of absolute signal strength. Although the “best” scheme varies with experimental geometry, the excitation strategy used in the present work was found to yield the highest signal strength during the entire stroke, in agreement with the literature review in Chapter 3.

Chapter 6 presents all data processing steps that are required for the conversion of NO LIF intensities into local concentration values, including the corrections for the in-cylinder attenuation and for the pressure and temperature dependence of the fluorescence yield. The total correction factor is found to vary by almost three orders

of magnitude during the combustion stroke. Absolute concentrations are obtained by a final calibration, scaling the NO concentration curve such that its value at the end of the combustion stroke matches the exhaust NO concentration. The latter is determined by an independent measurement. The results clearly show that the NO formation has already started before the most important formation mechanism, the Zeldovich mechanism, can come into play: the first NO LIF signal appears before the local temperature exceeds the temperature threshold (~ 1800 K) to activate the Zeldovich mechanism. This implies that another, yet unidentified mechanism is responsible for the initial NO formation during diesel combustion.

Chapter 7, too, reports quantitative, in-cylinder NO measurements. This time, the measurement cylinder is equipped with a common-rail fuel injection system, which allows to vary the injection timing. The resulting variation of the combustion temperature strongly influences the NO formation rate of the Zeldovich mechanism. Varying the moment of injection thus causes a variation of the amount of Zeldovich NO. These measurements are supplemented by a.o. calculated NO concentrations for identical engine conditions. The reasonable agreement between experiment and numerical simulation confirms the common belief that the Zeldovich mechanism is the major NO formation mechanism in (diesel) engines. However, transport of NO formed during the initial combustion towards the laser probe location is likely to be involved as well. Further research will be required to study the contribution of this early NO.

8.2 Outlook

8.2.1 Feasibility of two-dimensional NO LIF measurements

All NO LIF measurements in this thesis have been performed on only a very small fraction of the combustion chamber, probing either on the fuel spray axis (“through spray”) or between two such axes (“between sprays”). Although the current detection setup is able to obtain one-dimensional information (i.e. concentration profiles along the laser beam), up to now all data have been interpreted as (zero-dimensional) point measurements. Many laser techniques, and especially the LIF technique, are highly suitable for two-dimensional imaging experiments using a laser “sheet”. Such measurements would of course provide much more information on where the NO is formed and where it is transported. In fact, many previous NO LIF experiments in diesel engines have made use of a laser sheet configuration (e.g. Refs. 3–5, 8), but all of them lack a full attenuation correction, and the results can only be

interpreted qualitatively. In a popular configuration the laser sheet traverses the cylinder perpendicular to its axis, and the induced fluorescence is observed through the piston window.

Two-dimensional attenuation corrections Although a full correction of the attenuation of zero- or one-dimensional NO LIF measurements has been proven feasible in this thesis, it will be considerably more complicated for two-dimensional measurements. First of all, a large fraction of the fluorescence attenuation correction is based on the measurement of (broadband) absorption spectra by CO_2 and O_2 , which requires that at least four NO fluorescence bands are imaged. Analysing these absorption spectra on a per pixel basis (or clusters of pixels) would then yield a two-dimensional attenuation map. Such measurements could in principle be realised with a spectrograph-camera system like the one used in this thesis. However, in one direction the size of the imaged area is limited in order to prevent overlap of the imaged fluorescence bands. For instance, the width of the LIF subimages in e.g. Fig. 5.4 may not exceed the spectral dispersion. Moreover, each of the four subimages in Fig. 5.4 needs to be deconvolved with the rotational structure within the NO fluorescence spectrum. This is not straightforward, as the temperature and thus the (rotational) spectrum itself is position dependent.

An alternative would be to separate the fluorescence bands by means of a set of at least four band-pass filters (or dichroic mirrors), each filter transmitting only one vibronic fluorescence band. A filter set should be devised that images each LIF band onto a different region of the camera chip. Interference of Raman scattering by N_2 near 239 nm will limit the imaging of the (0,1) NO LIF band around 237 nm, especially around TDC where the N_2 density is still high and the NO fluorescence weak. Another drawback is that all other spectral information is lost, which makes it difficult to correct for broadband background luminosity and / or O_2 LIF interference. Perhaps a fifth filter could be used for assessment of the background intensity. Fortunately, in all engine experiments presented here, O_2 LIF interference was found to be minimal when exciting the $A-X(0,0)$ transition.

The bidirectional LIF method, making use of two counterpropagating laser pulses, can be, and has been, successfully applied using laser sheets. Two-dimensional maps of the laser beam attenuation coefficient have been obtained in a two-stroke diesel engine by Stoffels et al.⁹⁰

Two-dimensional temperature measurements Fitting the absorption by CO_2 and O_2 to the NO fluorescence band intensity ratios on a pixel (cluster) basis yields

two maps of both an attenuation correction factor and an *effective* temperature. As is argued in Chapter 6, for the current experimental geometry this effective temperature is close to that in the probe volume. However, this is not true in general. Especially with a “horizontal” laser sheet and LIF detection through the piston window, there may be considerable attenuation by CO_2 and O_2 between the laser plane and the piston window. Since the inferred temperature is biased towards regions with strong attenuation, it need no longer be related to the temperature in the volume occupied by the laser sheet.

As an alternative, accurate temperature measurements can be realised with vibrational thermometry of NO. Bessler et al. presented two-dimensional temperature fields obtained in both sooting and lean ethylene-air flames,⁵¹ using laser sheets at 226 nm and 248 nm. The results showed very good agreement with CARS measurements, a technique that is regarded as one of the most accurate temperature measurement techniques in combustion research. A disadvantage is that only relative temperature fields are obtained, and an overall calibration by e.g. CARS measurements is required.

Even on a zero-dimensional basis, it will be interesting and useful to evaluate the accuracy of the “ CO_2 ” temperature measurements in a diesel engine against other temperature measurement techniques, such as rotational⁵² and vibrational thermometry,⁵¹ soot pyrometry,¹⁴¹ and perhaps even CARS.⁶⁰

Conclusion As a conclusion, many practical issues currently limit the quantitative, two-dimensional imaging of in-cylinder NO concentrations. Although more equipment and additional, elaborate laser techniques would be required, such measurements are in principle feasible.

8.2.2 Low-sooting fuels: reducing the in-cylinder attenuation

Although corrections for in-cylinder attenuation effects are in principle possible, the accuracy is relatively low at very high attenuation levels. This is especially the case for measurements with the original line pump injection system. For the “through spray” measurements the observed transmission minimum is a mere 2%, leading to a relative accuracy of 50–60%; at the “between sprays” position these figures are even worse. These errors are directly reflected in the uncertainty of the derived NO concentration. For the common-rail system, the in-cylinder attenuation is somewhat lower (compare Figs. 6.4 and 7.17), already leading to an improved accuracy of the NO concentrations (compare Figs. 6.8 and 7.9).

Clearly, the accuracy of the current attenuation correction techniques is limited by the degree of attenuation. All experiments presented here were conducted at a relatively low engine load ($\sim 25\%$), in order to keep the attenuation at an acceptable level. For measurements at higher engine loads, or for an increased correction accuracy, it becomes necessary to reduce the in-cylinder UV attenuation by other means. One option is the use of special, low-sooting fuels. Since approximately one third of the total attenuation is due to soot (see Fig. 5.9), their effect may be substantial. As is pointed out in Section 1.2.3, oxygen-enriched fuels tend to reduce the engine-out soot levels. Although the exact mechanisms underlying this reduction are not fully understood, it is generally believed that the built-in oxygen atoms enhance the soot oxidation rate (rather than lowering the formation rate). Soot formation might be reduced as well, since many low-sooting fuels consist of linear hydrocarbon chains, lacking the aromatic rings needed to initialise soot formation. Of course, aromatic rings may still be formed after the longer chains are broken into smaller fragments.

In a preliminary investigation, laser beam transmission experiments were performed for different fuels and fuel blends, including regular diesel fuel, butylal ($\text{C}_4\text{H}_9\text{-O-CH}_2\text{-O-C}_4\text{H}_9$),⁴⁵ and a 50-50 blend of diesel and methylal ($\text{CH}_3\text{-O-CH}_2\text{-O-CH}_3$, also known as dimethoxymethane, DMM).^{43,44} The setup was identical to that in Chapter 5.3.3. The results are shown in Fig. 8.1. All experiments were carried with the original line pump fuel injection system, at 25% and 50% engine load. Although for each load the injection control was kept the same for all fuels, due to their different viscosities the injection duration was $\sim 1^\circ$ crank angle shorter for the low-sooting fuels. Thus, it is estimated that the injection yield was 10% lower for the low-sooting fuels (6% for the 50% load measurements). The low-sooting fuels clearly show an improved transmission, especially at higher engine loads (indicating that the transmission increase is not only due to the slightly reduced injection yield). This creates new possibilities for quantitative NO LIF measurements under high-load, heavy-duty diesel combustion.

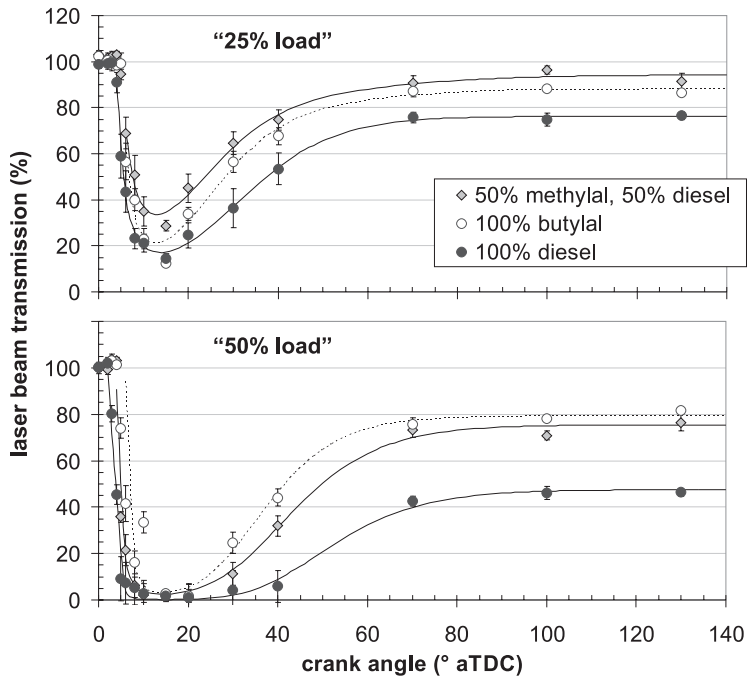


Figure 8.1: Laser beam transmission during the combustion stroke for different fuels and fuel blends, and at low and middle engine load. Lines guide the eye.

References

- [1] S. Beirle. *Estimating source strengths and lifetime of Nitrogen Oxides from satellite data*. PhD thesis, University of Heidelberg, 2004.
- [2] Th.M. Brugman, R. Klein-Douwel, G. Huigen, E. van Walwijk, and J.J. ter Meulen. Laser-induced-fluorescence imaging of NO in an n-heptane- and diesel-fuel-driven diesel engine. *Applied Physics B*, 57:405 – 410, 1993.
- [3] Th.M. Brugman, G.G.M. Stoffels, N.J. Dam, W.L. Meerts, and J.J. ter Meulen. Imaging and post-processing of laser-induced fluorescence from NO in a diesel engine. *Applied Physics B*, 64:717 – 724, 1997.
- [4] J.E. Dec and R.E. Canaan. PLIF imaging of NO formation in a DI diesel engine. *SAE Paper No. 980147*, 1998.
- [5] G.G.M. Stoffels, E.J. van den Boom, C.M.I. Spaanjaars, N. Dam, W.L. Meerts, J.J. ter Meulen, J.C.L. Duff, and D.J. Rickeard. In-cylinder measurements of NO formation in a diesel engine. *SAE Paper No. 1999-01-1487*, 1999.
- [6] F. Hildenbrand, C. Schulz, J. Wolfrum, F. Keller, and E. Wagner. Laser diagnostic analysis of NO formation in a direct injection diesel engine with pump-line-nozzle and common rail injection systems. *Proceedings of the Combustion Institute*, 28:1137 – 1143, 2000.
- [7] E.J. van den Boom, P.B. Monkhouse, C.M.I. Spaanjaars, W.L. Meerts, N.J. Dam, and J.J. ter Meulen. Laser diagnostics in a diesel engine. In V. I. Vlad, editor, *ROMOPTO 2000: Sixth Conference on Optics, Proc. SPIE 4430*, pages 593 – 606. SPIE, 2001.

REFERENCES

- [8] F. Hildenbrand, C. Schulz, F. Keller, G. König, and E. Wagner. Quantitative laser diagnostic studies of the NO distribution in a DI diesel engine with PLN and CR injection systems. *SAE Paper No. 2001-01-3500*, 2001.
- [9] P. Andresen, G. Meijer, H. Schlüter, H. Voges, A. Koch, W. Hentschel, W. Oppermann, and E. Rothe. Fluorescence imaging inside an internal combustion engine using tunable excimer lasers. *Applied Optics*, 29:2392 – 2404, 1990.
- [10] M. Knapp, A. Luczak, H. Schlüter, V. Beushausen, W. Hentschel, and P. Andresen. Crank-angle-resolved laser-induced fluorescence imaging of NO in a spark-ignition engine at 248 nm and correlations to flame front propagation and pressure release. *Applied Optics*, 35:4009 – 4017, 1996.
- [11] F. Hildenbrand, C. Schulz, V. Sick, G. Josefsson, I. Magnusson, and M. Aldén. Laser spectroscopic investigation of flow fields and NO formation in a realistic SI engine. *SAE Paper No. 980148*, 1998.
- [12] K. Akihama, T. Fujikawa, and Y. Hattori. Laser-induced fluorescence imaging of NO in a port-fuel-injected stratified-charge SI engine- correlations between NO formation region and stratified fuel distribution. *SAE Paper No. 981430*, 1998.
- [13] F. Hildenbrand, C. Schulz, M. Hartmann, F. Puchner, and G. Wawrschin. In-cylinder NO-LIF imaging in a realistic GDI engine using KrF excimer laser excitation. *SAE Paper No. 1999-01-3545*, 1999.
- [14] P. Jamette, V. Ricordeau, B. Deschamps, and P. Desgroux. Laser induced fluorescence detection of NO in the combustion chamber of an optical GDI engine with A-X(0,1) excitation. *SAE Paper No. 2001-01-1926*, 2001.
- [15] W.G. Bessler, M. Hoffmann, F. Zimmermann, G. Stuck, J. Jakobs, S. Nicklitzsch, T. Lee, J. Wolfrum, and C. Schulz. Quantitative in-cylinder NO-LIF imaging in a realistic gasoline engine with spray-guided direct injection. *Proceedings of the Combustion Institute*, 30:2667 – 2674, 2005.
- [16] H. Hiroyasu and M. Arai. Structures of fuel sprays in diesel engines. *SAE Paper No. 900475*, 1990.
- [17] T.A. Baritaud, T.A. Heinze, and J.F. Le Coz. Spray and self-ignition visualization in a DI diesel engine. *SAE Paper No. 940681*, 1994.

-
- [18] J.D. Naber and D.L. Siebers. Effect of gas density and vaporization on penetration and dispersion of diesel sprays. *SAE Paper No. 960034*, 1996.
- [19] R.J.H. Klein-Douwel, P.J.M. Frijters, L.M.T. Somers, W.A. de Boer, and R.S.G. Baert. High speed shadowgraphic, macroscopic characterization of diesel fuel sprays in a high pressure cell. *Fuel, submitted*, 2006.
- [20] J.E. Dec. Soot distribution in a D.I. diesel engine using 2-D imaging of laser-induced incandescence, elastic scattering, and flame luminescence. *SAE Paper No. 920115*, 1992.
- [21] C. Espey and J.E. Dec. Diesel engine combustion studies in a newly designed optical-access engine using high-speed visualization and 2-D laser imaging. *SAE Paper No. 930971*, 1993.
- [22] J.E. Dec and C. Espey. Ignition and early soot formation in a D.I. diesel engine using multiple 2-D imaging diagnostics. *SAE Paper No. 950456*, 1995.
- [23] J.E. Dec and C. Espey. Chemiluminescence imaging of autoignition in a DI diesel engine. *SAE Paper No. 982685*, 1998.
- [24] J.E. Dec, A.O. zur Loye, and D.L. Siebers. Soot distribution in a D.I. diesel engine using 2-D laser-induced incandescence imaging. *SAE Paper No. 910224*, 1991.
- [25] J.E. Dec and C. Espey. Soot and fuel distributions in a D.I. diesel engine via 2-D imaging. *SAE Paper No. 922307*, 1992.
- [26] J.E. Dec and E.B. Coy. OH radical imaging in a DI diesel engine and the structure of the early diffusion flame. *SAE Paper No. 960831*, 1996.
- [27] J.E. Dec. A conceptual model of DI diesel combustion based on laser-sheet imaging. *SAE Paper No. 970873*, 1997.
- [28] G.M. Faeth. Current status of droplet and liquid combustion. *Progress in Energy and Combustion Science*, 3:191 – 224, 1977.
- [29] J.B. Heywood. *Internal Combustion Engine Fundamentals*. McGraw-Hill, Singapore, 1988.
- [30] P.F. Flynn, R.P. Durrett, G.L. Hunter, A.O. zur Loye, O.C. Akinyemi, J.E. Dec, and C.K. Westbrook. Diesel combustion: An integrated view combining

REFERENCES

- laser diagnostics, chemical kinetics, and empirical validation. *SAE Paper No. 1999-01-0509*, 1999.
- [31] J.A. Miller and C.T. Bowman. Mechanism and modelling of nitrogen chemistry in combustion. *Progress in Energy and Combustion Science*, 15:287 – 338, 1989.
- [32] Y.B. Zeldovich. The oxidation of nitrogen in combustion and explosions. *Acta Physiochimica USSR*, 21:577 – 628, 1946.
- [33] G.A. Lavoie, J.B. Heywood, and J.C. Keck. Experimental and theoretical investigation of nitric oxide formation in internal combustion engines. *Combustion Science and Technology*, 1:313 – 326, 1970.
- [34] C.P. Fennimore. Formation of nitric oxide from fuel nitrogen in ethylene flames. *Combustion and Flame*, 19:289 – 296, 1972.
- [35] L.V. Moskaleva and M.C. Lin. The spin-conserved reaction $\text{CH} + \text{N}_2 \rightarrow \text{H} + \text{NCN}$: a major pathway to prompt no studied by quantum/statistical theory calculations and kinetic modelling of rate constant. *Proceedings of the Combustion Institute*, 28:2393 – 2401, 2000.
- [36] J. Wolfrum. Bildung von stickstoffoxiden bei der verbrennung. *Chemie-Ingenieur-Technik*, 44:656 – 659, 1972.
- [37] H. Tsukahara, T. Ishida, and M. Mayumi. Gas-phase oxidation of nitric oxide: Chemical kinetics and rate constant. *Nitric Oxide: Biology and Chemistry*, 3:191 – 198, 1999.
- [38] C. Arcoumanis, C. Bae, A. Nagwaney, and J.H. Whitelaw. Effect of EGR on combustion development in a 1.9l DI diesel optical engine. *SAE Paper No. 950850*, 1995.
- [39] R.S.G. Baert, D.E. Beckman, and R.P. Verbeek. New EGR technology retains HD diesel economy with 21st century emissions. *SAE Paper No. 960848*, 1996.
- [40] T.C. Tow, D.A. Pierpont, and R.D. Reitz. Reducing particulate and NO_x emissions by using multiple injections in a heavy duty D.I. diesel engine. *SAE Paper No. 940897*, 1994.

-
- [41] D.T. Montgomery and R.D. Reitz. Six-mode cycle evaluation of the effect of EGR and multiple injections on particulate and NO_x emissions from a D.I. diesel engine. *SAE Paper No. 960316*, 1996.
- [42] Z. Han, A. Uludogan, G.J. Hampson, and R.D. Reitz. Mechanism of soot and NO_x emission reduction using multiple-injection in a diesel engine. *SAE Paper No. 960316*, 1996.
- [43] B.L. Edgar, R.W. Dibble, and D.W. Naegeli. Autoignition of dimethyl ether and dimethoxy methane sprays at high pressures. *SAE Paper No. 971677*, 1997.
- [44] K.D. Vertin, J.M. Ohi, D.W. Naegeli, K.H. Childress, G.P. Hagen, C.I. McCarthy, A.S. Cheng, and R.W. Dibble. Methylal and methylal-diesel blended fuels for use in compression-ignition engines. *SAE Paper No. 1999-01-1508*, 1999.
- [45] A. Bertola and K. Boulouchos. Oxygenated fuels for particulate emissions reduction in heavy-duty DI-diesel engines with common-rail fuel injection. *SAE Paper No. 2000-01-2885*, 2000.
- [46] C. Havenith, R.P. Verbeek, D.M. Heaton, and P. van Sloten. Development of a urea DeNO_x catalyst concept for european ultra-low emission heavy-duty diesel engines. *SAE Paper No. 952652*, 1995.
- [47] A. Palmqvist, E. Jobson, L. Andersson, R. Granbro, M. Wendin, L. Megas, P. Nisius, A. Wiartalla, G. Lepperhoff, P. Blakeman, T. Ilkenhans, D. Webster, G. Haeffler, P. van de Voorde, P. Schmidt-Zhang, U. Guth, and M. Wallin. LOTUS: A co-operation for low temperature urea-based selective catalytic reduction of NO_x. *SAE Paper No. 2004-01-1294*, 2004.
- [48] B. Scarnegie, W.R. Miller, B. Ballmert, W. Doelling, and S. Fischer. Recent DPF/SCR results targeting US 2007 and Euro4/5 HD emissions. *SAE Paper No. 2003-01-0774*, 2003.
- [49] A.C. Eckbreth. *Laser Diagnostics for Combustion Temperature and Species*. Abacus Press, Cambridge, 1988.
- [50] W. Demtröder. *Laser spectroscopy: basic concepts and instrumentation*. Springer-Verlag, Berlin Heidelberg, 1981, 1996.

REFERENCES

- [51] W.G. Bessler, F. Hildenbrand, and C. Schulz. Two-line laser-induced fluorescence imaging of vibrational temperatures in a NO-seeded flame. *Applied Optics*, 40:748 – 756, 2001.
- [52] W.G. Bessler and C. Schulz. Quantitative multi-line NO-LIF temperature imaging. *Applied Physics B*, 78:519 – 533, 2004.
- [53] R. Evertsen, A. Staicu, N. Dam, A. van Vliet, and J.J. ter Meulen. Pulsed cavity ring-down spectroscopy of NO and NO₂ in the exhaust of a diesel engine. *Applied Physics B*, 74:465, 2002.
- [54] B.M. Vaglieco, S.S. Merola, and F.E. Corcione. Absolute NO and OH concentrations during diesel combustion process by multiwavelength absorption spectroscopy. *SAE Paper No. 2002-01-0892*, 2002.
- [55] M. Knapp, A. Luczak, V. Beushausen, W. Hentschel, P. Manz, and P. Andresen. Polarization separated spatially resolved single laser shot multispecies analysis in the combustion chamber of a realistic SI engine with a tunable KrF excimer laser. *Proceedings of the Combustion Institute*, 26:2589 – 2596, 1996.
- [56] P.C. Miles. Quantitative analysis of the near-wall mixture formation process in a passenger car direct-injection diesel engine by using linear Raman spectroscopy. *Applied Optics*, 38:1714 – 1732, 1999.
- [57] M. Taschek, J. Egermann, S. Schwarz, and A. Leipertz. Quantitative analysis of the near-wall mixture formation process in a passenger car direct-injection diesel engine by using linear Raman spectroscopy. *Applied Optics*, 44:6606 – 6615, 2005.
- [58] K. Kajiyama, K. Sajiki, H. Kataoka, S. Maeda, and C. Hirose. N₂ CARS Thermometry in Diesel Engines. *SAE Paper No. 821036*, 1982.
- [59] G.C. Alessandretti and P. Violino. Thermometry by CARS in an automobile engine. *Journal of Physics D*, 16:1583 – 1594, 1983.
- [60] C. Brackmann, J. Bood, M. Afzelius, and P.-E. Bengtsson. Thermometry in internal combustion engines via dual-broadband rotational coherent anti-Stokes Raman spectroscopy. *Measurement Science and Technology*, 15:R13 – R25, 2004.

-
- [61] J. Nygren, J. Engström, J. Walewski, C.F. Kaminski, and M. Aldén. Applications and evaluation of two-line atomic LIF thermometry in sooting combustion environments. *Measurement Science and Technology*, 12:1294 – 1303, 2001.
- [62] M.D. DiRosa, K.G. Klavuhn, and R.K. Hanson. LIF spectroscopy of NO and O₂ in high-pressure flames. *Combustion Science and Technology*, 118:257 – 283, 1996.
- [63] J. Luque and D.R. Crosley. LIFBASE: database and spectral simulation program (version 1.6). Report MP 99-009, SRI International, 1999. <http://www.sri.com/cem/lifbase>.
- [64] W.G. Bessler, C. Schulz, V. Sick, and J. W. Daily. A versatile modeling tool for nitric oxide LIF spectra. *3rd Joint Meeting of the US Sections of the Combustion Institute*, Chicago, 2003. <http://www.lifsim.com>.
- [65] H.L.G.J. van den Boom. *Laser diagnostics in diesel engines*. PhD thesis, University of Nijmegen, 2000. ISBN 90-9014077-8.
- [66] F. Hildenbrand. *Quantitative Bestimmung von NO-Konzentrations-verteilungen in einem DI-Dieselmotor*. PhD thesis, Ruprecht–Karls–Universität Heidelberg, 2000.
- [67] F.W. Bowditch. A new tool for combustion research – a quartz piston engine. *SAE Transactions*, 69:17 – 23, 1961.
- [68] Sigraflex[®], SGL Technologies, Meitingen, Germany.
- [69] D.L. Siebers. Liquid-phase fuel penetration in diesel sprays. *SAE Paper No. 980809*, 1998.
- [70] D.L. Siebers. Scaling liquid-phase fuel penetration in diesel sprays based on mixing-limited vaporization. *SAE Paper No. 1999-01-0528*, 1999.
- [71] B. Bougie. Delft University, personal communication, 2006.
- [72] B. Higgins and D. Siebers. Measurement of the flame lift-off location on DI diesel sprays using OH chemiluminescence. *SAE Paper No. 2001-01-0918*, 2001.

REFERENCES

- [73] M.P. Musculus, J.E. Dec, and D.R. Tree. Effects of fuel parameters and diffusion flame lift-off on soot formation in a heavy-duty DI diesel engine. *SAE Paper No. 2002-01-0889*, 2002.
- [74] D. Siebers and B. Higgins. Flame lift-off on direct-injection diesel sprays under quiescent conditions. *SAE Paper No. 2001-01-0530*, 2001.
- [75] G.J. Schoonderbeek. Emissiemeting aan de uitlaat van een dieselmotor. Graduation report, University of Nijmegen, 2002.
- [76] K.P. Huber and G. Herzberg. Constants of diatomic molecules. *NIST Standard Reference Database Number 69*, 2005.
- [77] A.Y. Chang, M.D. di Rosa, and R.K. Hanson. Temperature dependence of collision broadening and shift in the NO A-X (0,0) band in the presence of argon and nitrogen. *Journal of Quantitative Spectroscopy and Radiative Transfer*, 47:375, 1992.
- [78] M.D. di Rosa and R.K. Hanson. Collision broadening and shift of NO γ (0,0) absorption lines by O₂ and H₂O at high temperatures. *Journal of Quantitative Spectroscopy and Radiative Transfer*, 52:515, 1994.
- [79] A.O. Vydrov, J. Heinze, and U.E. Meier. Collision broadening of spectral lines in the A-X (0,0) system of NO by N₂, Ar and He at elevated pressures measured by laser-induced fluorescence. *Journal of Quantitative Spectroscopy and Radiative Transfer*, 53:277, 1995.
- [80] G.G.M. Stoffels. *Nitric oxide in a diesel engine: laser-based detection and interpretation*. PhD thesis, University of Nijmegen, 1999. ISBN 90-9012846-8.
- [81] R.J. Cattolica, T.G. Mataga, and J.A. Cavolowski. Electronic quenching and vibrational relaxation of NO A² Σ (v' = 1) and (v' = 0) by collisions with H₂O. *Journal of Quantitative Spectroscopy and Radiative Transfer*, 42:499–508, 1989.
- [82] J.W. Thoman, J.A. Gray, J.L. Durant, and P.H. Paul. Collisional electronic quenching of NO A² Σ^+ by N₂ from 300 to 4500 K. *Journal of Chemical Physics*, 97:8156 – 8163, 1992.

- [83] P.H. Paul, J.A. Gray, J.L. Durant, and J.W. Thoman. A model for temperature-dependent collisional quenching of NO $A^2\Sigma^+$. *Chemical Physics Letters*, 57:249 – 259, 1993.
- [84] M.R. Furlanetto, J.W. Thoman, J.A. Gray, P.H. Paul, and J.L. Durant. Near-resonant electronic energy transfer in the electronic quenching of NO $A^2\Sigma^+$ by hydrocarbons and ammonia. *Journal of Chemical Physics*, 101:10452 – 10457, 1994.
- [85] P.H. Paul, J.A. Gray, J.L. Durant, and J.W. Thoman. Collisional electronic quenching rates for NO $A^2\Sigma^+(v' = 0)$. *Chemical Physics Letters*, 259:508 – 514, 1996.
- [86] Y. Aoyagi, T. Kamimoto, Y. Matsui, and S. Matsuoka. A gas sampling study on the formation processes of soot and NO in a DI diesel engine. *SAE Paper No. 800254*, 1980.
- [87] P. Jamette. *Imagerie de NO par fluorescence induite par laser dans un moteur à allumage commandé*. PhD thesis, Université des sciences et technologies de Lille, 2001.
- [88] F.R. Gilmore. Potential energy curves for N_2 , NO, O_2 and corresponding ions. *Journal of Quantitative Spectroscopy and Radiative Transfer*, 5:369 – 390, 1965.
- [89] A. Arnold, F. Dinkelacker, T. Heitzmann, P. Monkhouse, M. Schäfer, V. Sick, J. Wolfrum, W. Hentschel, and K.-P. Schindler. DI diesel engine combustion visualised by combined laser techniques. *Proceedings of the Combustion Institute*, 24:1605 – 1612, 1992.
- [90] G.G.M. Stoffels, S. Stoks, N. Dam, and J.J. ter Meulen. Methods to correct planar LIF distributions for local non-uniform laser attenuation. *Applied Optics*, 39:5547 – 5559, 2000.
- [91] B. Alataş, J.A. Pinson, T.A. Litzinger, and D.A. Santavicca. A study of NO and soot evolution in a DI diesel engine via planar imaging. *SAE Paper No. 930973*, 1993.
- [92] H. Nakagawa, H. Endo, Y. Deguchi, M. Noda, H. Oikawa, and T. Shimada. NO measurements in diesel spray flame using laser induced fluorescence. *SAE Paper No. 970874*, 1997.

REFERENCES

- [93] A. Bräumer, V. Sick, J. Wolfrum, V. Drewes, M. Zahn, and R. Maly. Quantitative two-dimensional measurements of nitric oxide and temperature distributions in a transparent square piston SI engine. *SAE Paper No. 952462*, 1995.
- [94] G.G.M. Stoffels, P. Schmidt, N. Dam, and J.J. ter Meulen. Generation of 224-nm radiation by stimulated Raman scattering of ArF excimer laser radiation in a mixture of H₂ and D₂. *Applied Optics*, 36:6797 – 6801, 1997.
- [95] W.G. Bessler, C. Schulz, T. Lee, J.B. Jeffries, and R.K. Hanson. Strategies for laser-induced fluorescence detection of nitric oxide in high-pressure flames. II. A-X(0,1) excitation. *Applied Optics*, 42:2031 – 2042, 2003.
- [96] C. Schulz, V. Sick, J. Wolfrum, V. Drewes, M. Zahn, and R. Maly. Quantitative 2D single-shot imaging of NO concentrations and temperatures in a transparent SI engine. *Proceedings of the Combustion Institute*, 26:2597 – 2604, 1996.
- [97] G. Josefsson, I. Magnusson, F. Hildenbrand, C. Schulz, and V. Sick. Multidimensional laser diagnostic and numerical analysis of NO formation in a gasoline engine. *Proceedings of the Combustion Institute*, 27:2085 – 2092, 1998.
- [98] F. Hildenbrand, C. Schulz, E. Wagner, and V. Sick. Investigation of spatially resolved light absorption in a spark-ignition engine fueled with propane/air. *Applied Optics*, 38:1452 – 1458, 1999.
- [99] F. Hildenbrand and C. Schulz. Measurements and simulation of in-cylinder UV-absorption in spark ignition and diesel engines. *Applied Physics B*, 73:173 – 180, 2001.
- [100] C. Schulz, J.B. Jeffries, D.F. Davidson, J.D. Koch, and R.K. Hanson. Impact of UV absorption by CO₂ and H₂O on NO LIF in high-pressure combustion applications. *Proceedings of the Combustion Institute*, 29:2735 – 2742, 2002.
- [101] W.G. Bessler, C. Schulz, T. Lee, J.B. Jeffries, and R.K. Hanson. Strategies for laser-induced fluorescence detection of nitric oxide in high-pressure flames. I. A-X(0,0) excitation. *Applied Optics*, 41:3547 – 3557, 2002.
- [102] W.G. Bessler, C. Schulz, T. Lee, J.B. Jeffries, and R.K. Hanson. Strategies for laser-induced fluorescence detection of nitric oxide in high-pressure flames.

- III. Comparison of A-X excitation schemes. *Applied Optics*, 42:4922 – 4936, 2003.
- [103] C. Schulz, V. Sick, J. Heinze, and W. Stricker. Laser-induced-fluorescence detection of nitric oxide in high-pressure flames with A-X(0,2) excitation. *Applied Optics*, 36:3227 – 3232, 1997.
- [104] C. Schulz, V. Sick, U. Meier, J. Heinze, and W. Stricker. Quantification of NO A-X(0,2) LIF: Investigation of calibration and collisional influences in high-pressure flames. *Applied Optics*, 38:1434 – 1443, 1999.
- [105] W.G. Bessler, C. Schulz, T. Lee, D.-I. Shin, M. Hofmann, J.B. Jeffries, J. Wolfrum, and R.K. Hanson. Quantitative NO-LIF imaging in high-pressure flames. *Applied Physics B*, 75:97 – 102, 2002.
- [106] B. Atakan and A.T. Hartlieb. Laser diagnostics of NO reburning in fuel-rich propene flames. *Applied Physics B*, 71:697 – 702, 2000.
- [107] P.H. Krupenie. The spectrum of molecular oxygen. *Journal of Physical and Chemical Reference Data*, 1:423–534, 1972.
- [108] K. Verbiezen, R.J.H. Klein-Douwel, A.J. Donkerbroek, A.P. van Vliet, W.L. Meerts, N.J. Dam, and J.J. ter Meulen. Attenuation corrections for in-cylinder NO LIF measurements in a heavy-duty diesel engine. *Applied Physics B*, 83:155 – 166, 2006.
- [109] K. Verbiezen, R.J.H. Klein-Douwel, A.P. van Vliet, W.L. Meerts, N.J. Dam, and J.J. ter Meulen. Quantitative laser-induced fluorescence measurements of nitric oxide in a heavy-duty diesel engine. *Proceedings of the Combustion Institute*, 31, 2006.
- [110] K. Verbiezen, A.J. Donkerbroek, A.P. van Vliet, W.L. Meerts, R.J.H. Klein-Douwel, N.J. Dam, and J.J. ter Meulen. Dealing with laser beam attenuation during nitric oxide fluorescence measurements in a diesel engine. In *Proceedings of the European Combustion Meeting 2003*, Orléans, France, 2003.
- [111] C.S. Cooper and N.M. Laurendeau. Quantitative measurements of nitric oxide in high-pressure (2 – 5 atm), swirl-stabilized spray flames via laser-induced fluorescence. *Combustion and Flame*, 123:175 – 188, 2000.

REFERENCES

- [112] A.V. Mokhov, H.B. Levinsky, and C.E. van der Meij. Temperature dependence of laser-induced fluorescence of nitric oxide in laminar premixed atmospheric-pressure flames. *Applied Optics*, 36:3233 – 3243, 1997.
- [113] R. Abu-Gharbieh, J. Persson, M. Försth, A. Rosén, A. Karlström, and T. Gustavsson. Compensation method for attenuated planar laser images of optically dense sprays. *Applied Optics*, 39:1260 – 1267, 2000.
- [114] V. Sick and B.D. Stojkovic. Attenuation effects on imaging diagnostics of hollow-cone sprays. *Applied Optics*, 40:2435 – 2442, 2001.
- [115] J.V. Pastor, J.J. López, J.E. Juliá, and J.V. Benajes. Planar laser-induced fluorescence fuel concentration measurements in isothermal diesel sprays. *Optics Express*, 10:309 – 323, 2002.
- [116] F.E. Corcione, S.S. Merola, B.M. Vaglieco, and G. Formisano. Spectral analysis of combustion process of common-rail diesel engine. *SAE Paper No. 2002-01-1634*, 2002.
- [117] S.S. Merola, B.M. Vaglieco, and J. Zarinchang. Simultaneous detection of NO_x and particulate in exhaust of a CR diesel engine by UV-visible spectroscopy. *SAE Paper No. 2003-01-0786*, 2003.
- [118] B. Trost, J. Stutz, and U. Platt. UV-absorption cross sections of a series of monocyclic aromatic compounds. *Atmospheric Environment*, 31:3999 – 4008, 1997.
- [119] T. Etkorn, B. Klotz, S. Sørensen, I.V. Patroescu, I. Barnes, K.H. Becker, and U. Platt. Gas-phase absorption cross sections of 24 monocyclic aromatic hydrocarbons in the UV and IR spectral ranges. *Atmospheric Environment*, 33:525 – 540, 1999.
- [120] C. Schulz, J.D. Koch, D.F. Davidson, J.B. Jeffries, and R.K. Hanson. Ultra-violet absorption spectra of shock-heated carbon dioxide and water between 900 and 3050 K. *Chemical Physics Letters*, 355:82 – 88, 2002.
- [121] K. Verbiezen, A.P. van Vliet, W.L. Meerts, N.J. Dam, and J.J. ter Meulen. Absorption of NO laser-induced fluorescence by hot O₂ and CO₂. *Combustion and Flame*, 144:638–641, 2006.

-
- [122] D. Stepowski. Auto calibration of OH laser induced fluorescence signals by local absorption measurement in a flame. *Proceedings of the Combustion Institute*, 23:1839 – 1846, 1990.
- [123] M. Versluis, N. Georgiev, L. Martinsson, M. Aldén, and S. Kröll. 2-D absolute OH concentration profiles in atmospheric flames using planar LIF in a bi-directional laser beam configuration. *Applied Physics B*, 65:411 – 417, 1997.
- [124] A. Ciajolo, R. Ragucci, B. Apicella, R. Barbella, M. de Joannon, and A. Tregrossi. Fluorescence spectroscopy of aromatic species produced in rich pre-mixed ethylene flames. *Chemosphere*, 42:835–841, 2001.
- [125] J. Egermann, T. Seeger, and A. Leipertz. Application of 266-nm and 355-nm Nd:YAG laser radiation for the investigation of fuel-rich sooting hydrocarbon flames by Raman scattering. *Applied Optics*, 43:5564–5574, 2004.
- [126] R.L. Vander Wal and K.A. Jensen. Laser-induced incandescence: excitation intensity. *Applied Optics*, 37:1607 – 1616, 1998.
- [127] N.P. Tait and D.A. Greenhalg. PLIF imaging of fuel fraction in practical devices and LII imaging of soot. *Berichte der Bunsen-Gesellschaft für Physikalische Chemie*, 97:1619–1625, 1993.
- [128] F.E. Corcione. Optical diagnostics in engines. In *Proceedings of COMODIA 2001*, pages 22 – 36. COMODIA, 2001.
- [129] M. Schnaiter, H. Horvath, O. Möhler, K.-H. Naumann, H. Saathoff, and O. W. Schöck. UV-VIS-NIR spectral optical properties of soot and soot-containing aerosols. *Journal of Aerosol Science*, 34:1421 – 1444, 2003.
- [130] B. Bougie, L.C. Ganippa, A.P. van Vliet, N.J. Dam, W.L. Meerts, and J.J. ter Meulen. Soot characterization with laser induced incandescence in a heavy duty diesel engine. In *Proceedings of the European Combustion Meeting 2005*, Louvain-la-Neuve, Belgium, 2005.
- [131] Keep the noise down! — low noise: an integral part of high-performance CCD (HCCD) camera systems. Technical Report 4, Roper Scientific, 1999.
- [132] N.M. Sijtsema, R.A.L. Tolboom, N.J. Dam, and J.J. ter Meulen. Two-dimensional multispecies imaging of a supersonic flow. *Optics Letters*, 24:664–666, 1999.

REFERENCES

- [133] R.A.L. Tolboom, N.J. Dam, J.J. ter Meulen, J.M. Mooij, and J.D.M. Maassen. Quantitative imaging through a spectrograph. 1. Principles and theory. *Applied Optics*, 43:5669–5681, 2004.
- [134] K. Verbiezen, A.P. van Vliet, R.J.H. Klein-Douwel, L.C. Ganippa, B. Bougie, W.L. Meerts, N.J. Dam, and J.J. ter Meulen. Quantitative nitric oxide measurements by means of laser-induced fluorescence in a heavy-duty diesel engine. In *Proceedings of the European Combustion Meeting 2005*, Louvain-la-Neuve, Belgium, 2005.
- [135] J.B. Jeffries, C. Schulz, D.W. Mattison, M.A. Oehlschlaeger, W.G. Bessler, T. Lee, D.F. Davidson, and R.K. Hanson. UV absorption of CO₂ for temperature diagnostics of hydrocarbon combustion applications. *Proceedings of the Combustion Institute*, 30:1591 – 1599, 2005.
- [136] H. Barths, C. Antoni, and N. Peters. Three-dimensional simulation of pollutant formation in a DI diesel engine using multiple interactive flamelets. *SAE Paper No. 982459*, 1998.
- [137] R.J.H. Klein-Douwel, M. Douch, L.M.T. Somers, W.A. de Boer, and R.S.G. Baert. Visualisation of diesel fuel spays in a high pressure, high temperature cell under engine-like conditions. In *Proceedings of the European Combustion Meeting 2003*, Orléans, France, 2003.
- [138] P.J.M. Frijters, R.J.H. Klein-Douwel, S.S. Manski, L.M.T. Somers, and R.S.G. Baert. High speed analysis of high pressure combustion in a constant volume cell. In *Proceedings of the European Combustion Meeting 2005*, Louvain-la-Neuve, Belgium, 2005.
- [139] S. Gordon and B.J. McBride. Computer program for the calculation of complex chemical equilibrium compositions with applications; I. analysis. NASA Reference Publication 1311, 1994.
- [140] G.P. Smith, D.M. Golden, M. Frenklach, N.W. Moriarty, B. Eiteneer, M. Goldenberg, C.T. Bowman, R.K. Hanson, S. Song, W.C. Gardiner, V.V. Lissianski, and Z. Qin. GRI Mech 3.0. Technical report, 2000. http://www.me.berkeley.edu/gri_mech.
- [141] H.C. Hottel and F.P. Broughton. Determination of true temperature and total radiation from luminous gas flames. *Industrial and Engineering Chemistry (Analytical Edition)*, 4:166 – 175, 1932.

Samenvatting

Kwantitatieve NO metingen in een dieselmotor

Ondanks de populariteit van de dieselmotor is de uitstoot van onder andere stikstofdioxide (NO) problematisch. NO reageert in de buitenlucht tot stikstofdioxide (NO₂), wat één van de veroorzakers is van zure regen. Daarnaast kunnen hoge concentraties NO₂ leiden tot smogvorming.

In veel landen moeten vooral nieuwere motoren voldoen aan steeds strengere emissie-eisen. Om op systematische wijze schonere motoren te kunnen ontwikkelen is het belangrijk om het verbrandingsproces goed te begrijpen. De precieze vormingsmechanismen van NO zijn echter niet goed genoeg bekend. Met behulp van nauwkeurige, kwantitatieve experimenten kunnen wellicht nieuwe inzichten hierin worden verkregen. Het probleem is dat een betrouwbare meettechniek om de NO-vorming in dieselmotoren te meten tot op heden ontbrak; met hedendaagse apparatuur kan men slechts in de uitlaat (dus nadat het verbrandingsproces is afgelopen) de NO concentratie bepalen.

In dit proefschrift wordt een techniek geïntroduceerd waarmee de lokale NO-concentratie in één van de cilinders van een dieselmotor *tijdens* de verbranding gemeten kan worden. Met behulp van laserspectroscopie kunnen NO-moleculen zichtbaar worden gemaakt, zonder dat het verbrandingsproces verstoord wordt (er wordt alleen wat licht op geschoten). Door absorptie van smalbandig laserlicht kan een molecuul in een hogere energietoestand komen (excitatie). Het molecuul kan een deel van zijn energie weer kwijt raken via energie-overdracht bij botsingen met andere moleculen (quenching), of door uitzending van licht (fluorescentie). Vandaar dat deze meettechniek ook wel bekend staat als *laser geïnduceerde fluorescentie (LIF)*: onder invloed van laserlicht straalt een molecuul zijn "eigen" licht uit.

Ieder type molecuul kan slechts enkele, molecuul-specifieke golflengtes licht absorberen. Door de lasergolflengte te verstemmen is het dus mogelijk het molecuul

te selecteren dat men wil meten. Eén van die zogenaamde excitatiegolflengtes voor NO ligt rond 226 nm, en deze is gebruikt voor de metingen in dit onderzoek. Ook het fluorescentiespectrum is karakteristiek voor ieder molecuul. Dit geeft een extra mogelijkheid om verschillende typen moleculen van elkaar te onderscheiden, en dat is erg handig als meerdere moleculen dezelfde excitatiegolflengte hebben. Zo blijkt het erg moeilijk om te voorkomen dat naast NO ook zuurstof (O_2) wordt geëxciteerd. Dit is te ondervangen door de moleculen op basis van hun emissiespectrum te identificeren, al is er deels ook sprake van overlap (interferentie).

In principe is de intensiteit van de uitgezonden NO-fluorescentie evenredig met zowel de laserintensiteit als de NO-molecuuldichtheid. Dit betekent dat de geïnduceerde fluorescentie een maat is voor de NO-concentratie. In de praktijk is het lastig om de lokale laserintensiteit te bepalen, omdat het laserlicht sterk wordt geabsorbeerd in de cilinder en de mate van absorptie onbekend is. Datzelfde geldt trouwens ook voor de fluorescentie. Daarnaast zijn er een aantal spectroscopische aspecten. De kans dat een molecuul laserlicht absorbeert hangt onder meer af van de energietoestand waarin het molecuul zich bevindt, wat weer temperatuurafhankelijk is. Daarnaast is van invloed hoe goed de lasergolflengte is afgestemd op de excitatiegolflengte van het molecuul. Deze zogenaamde lijnoverlap hangt sterk af van de omgevingsdruk. Ook de balans tussen energieverlies door fluorescentie en energieverlies door botsingen met andere moleculen is drukafhankelijk (hoe hoger de druk, des te meer quenching, en dus een lagere fluorescentieopbrengst). Deze aspecten worden beschreven in hoofdstuk 3 en later toegepast in hoofdstuk 6. Door ze te modelleren is het mogelijk om de fluorescentieopbrengst per NO molecuul als functie van omgevingsdruk en -temperatuur te voorspellen. Deze varieert tijdens de metingen over een factor 40, doordat zowel druk als temperatuur sterk veranderen tijdens de verbrandingsslag. In hoofdstuk 3 wordt tevens een vergelijking gemaakt tussen een aantal mogelijke excitatie-golflengtes voor NO. Er kan worden geconcludeerd dat, volgens de literatuur, excitatie bij 226 nm doorgaans het sterkste en zuiverste signaal geeft (d.w.z. weinig interferentie door O_2).

Het is niet eenvoudig om de LIF-techniek toe te passen in een verbrandingsmotor. Ten eerste dient de verbrandingskamer optisch toegankelijk gemaakt te worden. De modificaties aan de zes-cilinder DAF-motor die gebruikt is voor de metingen worden beschreven in hoofdstuk 2. Hierin wordt ook ingegaan op de twee brandstofinjectiesystemen die gebruikt zijn tijdens dit onderzoek.

Een ander probleem is de sterke verzwakking van zowel het laserlicht als de NO-fluorescentie in de verbrandingskamer. Deze verzwakking wordt voornamelijk veroorzaakt door absorptie en verstrooiing van het licht door roetdeeltjes en brand-

stofdruppeltjes, en door absorptie door polycyclische aromatische koolwaterstoffen (PAK's)*, heet O_2 en hete (verbrandings-) gassen zoals CO_2 , H_2O .

In de hoofdstukken 4 en 5 wordt een aantal (laser-) technieken gepresenteerd waarmee de verschillende bijdragen aan de totale verzwakking kunnen worden gemeten. Door technieken te combineren kan uiteindelijk de totale verzwakking worden gereconstrueerd. Het is noemenswaardig dat de vorm van de absorptiespectra van heet O_2 en CO_2 sterk temperatuurafhankelijk is. Aangezien deze temperatuurafhankelijkheid bekend is, levert een meting van deze absorptiespectra niet alleen een verzwakkingscorrectie op, maar ook een meting van de lokale temperatuur. Dit is onder andere een belangrijke parameter bij het berekenen van de fluorescentieopbrengst (zie boven). Uit metingen is gebleken dat de verzwakking van laserlicht en fluorescentie sterk varieert tijdens de motorcyclus. Op sommige momenten wordt het licht maar liefst een factor 50 verzwakt.

Na correctie voor verzwakkingseffecten en de druk- en temperatuurafhankelijkheid van de fluorescentie-opbrengst kunnen de LIF-signalen worden omgerekend naar NO concentraties. Deze stappen worden beschreven in hoofdstuk 6. De resultaten tonen aan dat de vorming van NO al begonnen is voordat het meest bekende reactiemechanisme (het Zeldovich mechanisme) een belangrijke rol kan spelen. Dit wijst erop dat een ander, nader te bepalen reactiemechanisme verantwoordelijk is voor de initiële NO-vorming tijdens dieselverbranding.

Ook in hoofdstuk 7 worden kwantitatieve NO metingen beschreven. Door de meetcilinder uit te rusten met een common-rail brandstofinjector is het mogelijk om het moment van inspuiting te variëren. Dit beïnvloedt de verbrandingstemperatuur en daarmee ook de hoeveelheid NO die gevormd wordt via het Zeldovich mechanisme. Door het inspuitmoment te variëren wordt dus de hoeveelheid Zeldovich-NO gevarieerd. De metingen worden onder andere vergeleken met berekende NO-concentraties voor dezelfde motorcondities. De redelijke overeenstemming tussen experiment en berekening suggereert dat het Zeldovich mechanisme de grootste bijdrage levert aan de totale NO-vorming in (diesel-) motoren, alhoewel transport van eerder gevormd NO naar het meetvolume zeer waarschijnlijk ook een rol speelt. Verder onderzoek zal dit moeten uitwijzen.

*PAK's zijn ringvormige koolwaterstoffen die worden gevormd nadat de brandstof is "gekraakt" tot kleinere bouwstenen tijdens het eerste deel van de verbranding. Ze zijn de voorlopers van roet.

Dankwoord

En toen was het boekje afgelopen uit! Nou ja, bijna dan, want dit is zo'n beetje het laatste stukje dat ik nog schrijf. Eerlijk gezegd heb ik gemengde gevoelens nu het eind echt nadert. En het had toch ook wel iets: 's avonds schrijven, met Pablo trouw aan mijn voeten liggend... Gelukkig mogen we nog heel even, want mijn proefschrift is pas echt af als ik een aantal mensen bedankt heb.

Allereerst natuurlijk Hans ter Meulen, niet alleen omdat je me een positie als junior onderzoeker aanbood op het uitdagende dieselproject, maar zeker ook voor je heldere kijk en (opbouwend) kritische houding tegenover alles wat ik op papier zette. Het is een cliché, maar ik meen het als ik zeg dat dankzij jou dit proefschrift is geworden wat het nu is.

Nico Dam, mijn directe begeleider, dankzij jouw creativiteit vonden we overal een oplossing voor. Ik heb veel van je geleerd tijdens onze talloze discussies ("Als we het eens zijn heb jij gelijk, als we het niet eens zijn heb ik gelijk."), in het lab en daarbuiten. Ik heb zelfs jouw bijzondere gevoel voor humor — tegen wil en dank — leren waarderen. Een beetje dan.

Leo Meerts, een waardig lid van het "dieselteam", van harte bedankt voor je enthousiaste bijdrage aan ons onderzoek, en voor de nauwkeurige correcties op het manuscript.

En dan nu de beide Arjans. Arjan van Vliet, jij was er bij iedere meting bij om de motor te starten en in toom te houden ("We gaan beginnen..!") en het is dankzij jouw technische ondersteuning en expertise dat we zoveel mooie metingen hebben gedaan. Ook jij stond altijd klaar met een flinke dosis humor en praktische vindingrijkheid. Ik zal het moment nooit vergeten dat we met een zelfgemaakte sleutel van drie meter lang, op "veilige" afstand, een vat licht ontvlambare brandstof voor het eerst open maakten. En dat we voor diezelfde metingen de brandstofleiding met ijswater moesten koelen omdat het buiten 35° C was... Je was terecht beledigd toen ik de resultaten in eerste instantie niet in mijn boekje wilde opnemen. Arjan

Donkerbroek, het was erg leerzaam en gezellig om jou tijdens je afstudeerstage te mogen begeleiden. Nog beter was het om je de laatste maanden van mijn onderzoek in te werken op het dieselpoject, en dat zeg ik niet alleen uit eigenbelang (ook al zijn de mooie resultaten in Hoofdstuk 7 voor een groot deel aan jouw inzet te danken!). Ik vind het geweldig dat jij nu het dieselonderzoek voortzet en ik wil je daarbij veel succes wensen. Ook was je een fijne kamergenoot in Graalburcht G003b. Alle Graalburchtbewoners genoten regelmatig van jouw kwaliteiten als experimentator, als je weer eens een zelfgebakken appeltaart meenam. Ik weet niet hoe je het deed, maar zelfs als ze “een beetje zwart” waren smaakten ze overheerlijk. Overigens werd dat zwarte gaandeweg steeds minder en is jouw geheime recept nu vervolmaakt.

Robert Klein-Douwel, als postdoc was jij was degene die mij heeft ingewerkt en ik heb veel van jouw ervaring geleerd, waarvoor mijn dank. Het was altijd leuk om jouw correcties op mijn schrijfsels door te lezen; als mijn Engels haperde was jij degene die met voorbeelden toelichtte waarom het niet klopte. Dat was leerzaam en vaak ook grappig. Ik wil hierbij wel vermelden dat eventuele overgebleven fouten in dit boekje geheel voor mijn rekening zijn.

Lionel Ganippa, the second postdoc on the diesel project, and my other roommate in G003b, thank you very much for sharing your vast knowledge on internal combustion engines. It was great working with you, and to get to know you better during conferences (Chicago). However short the time you stayed in Nijmegen, it was enough to become friends, and I will remember the great times when you invited Wendy and me to your home (and the delicious dinners we enjoyed!).

Ook de andere afdelingstechnici zorgden voor de nodige ondersteuning: Peter Claus, dank je voor de talloze uitbreidingen en verbeteringen aan de meet- en regel-electronica van de motor. Leander Gerritsen, bedankt voor je hulp toen Arjan op (halve) wereldreis was. Het moet enorm frustrerend geweest zijn om telkens weer naar de Graalburcht te lopen omdat ik in mijn onervarenheid weer een zuigerveer had laten “springen” bij het openen van de meetcilinder. Verder wil ik Cor Sikkens, André van Roij en Danny Ramsamoedj bedanken voor hun technische bijdrage en voor de gezelligheid. De techneuten op de instrumentmakerij, Harrie van Brakel en de zijnen, en Peter van Dijk en Peter Walraven op de glasblazerij: bedankt dat we op jullie konden rekenen.

Onze projectpartners op de TU/e, bedankt voor de prettige samenwerking: Rik Baert, Bart Soomers, Peter Frijters, Xander Seijkens, Alexei Evlampiev en Vincent Huijnen. Rik, ook bedankt voor je kritische beoordeling van het manuscript.

Gerne möchte ich mir bedanken bei Christof Schulz für die ausführliche Überprüfung des Manuskriptes, und für die die Gelegenheit, als Gastforscher in seiner Gruppe

an der Universität Duisburg-Essen teilzunehmen. Ich danke Ralf Starke, Boris Kock, André Wagner und den anderen Mitarbeitern für die freundliche Atmosphäre und die lehrreiche Zusammenarbeit.

Frans Harren, voorzitter van de manuscriptcommissie, ook jij hartelijk bedankt voor het doornemen van mijn boekje in wording.

Natuurlijk wil ik graag alle andere (voormalige) Graalburchtbewoners bedanken voor de gezelligheid en de fijne samenwerking: collega dieselonderzoeker Bas Bougie, filmexperts Thijs Elenbaas en Jeroen Bominaar, Iris Bominaar-Silkens, Mira Pashtrapanska, Coralie Schoemaeker-Moreau, Willem van de Water, René Tolboom, Marianna Sijtsma, Margriet Verkuilen, de troubadour Willem Pieter van der Laan en Gert Jan Schoonderbeek. Ine Meijer, ook jij bedankt voor de secretariële ondersteuning en de gezelligheid. Alle andere, nog niet genoemde medewerkers van de afdelingen Molecuul- en Laserfysica en Toegepaste Fysica: bedankt voor de altijd goede sfeer.

Graag wil ik mijn (schoon-) familie en vrienden bedanken voor hun steun en interesse, en "mijn" ASML carpoolers die een half jaar mijn klachten over het schrijven van een proefschrift moesten aanhoren.

Tenslotte mijn kersverse echtgenote: Wendy, gelukkig begrijp je me zo ook wel, want het valt niet in woorden te beschrijven hoeveel jij voor me betekent.

Kasper

Curriculum vitae

Kasper Verbiezen

- geboren:* 13 maart 1978 te Nijmegen.
- 1991–1996:* gymnasium op het Dominicus College te Nijmegen.
- 1996–2001:* experimentele natuurkunde aan de Katholieke Universiteit Nijmegen. Afstudeerstage: “Microwave-infrared double resonance of NH_3 molecules in helium droplets” op de afdeling Moleculen en Laserfysica van Prof. Dr. D.H. Parker.
- 2001–2006:* promotieonderzoek aan de Radboud Universiteit Nijmegen, op de afdeling Toegepaste Fysica van Prof. Dr. J.J. ter Meulen: “Quantitative NO measurements in a diesel engine” (dit proefschrift).
- 2006–heden:* werkzaam bij ASML Nederland, Illumination Systems Development.

Publications

- *Laser diagnostics in a diesel engine*, K. Verbiezen, A.P. van Vliet, N.J. Dam, and J.J. ter Meulen, Proceedings of the joint meeting of the Belgian and Dutch sections of the Combustion Institute, Brussels, Belgium (2002).
- *Laser beam attenuation in LIF measurements on NO in a diesel engine*, K. Verbiezen, A.J. Donkerbroek, A.P. van Vliet, R.J.H. Klein-Douwel, N.J. Dam, and J.J. ter Meulen, Proceedings of the European Combustion Meeting 2003, Orléans, France (2003).
- *Quantitative nitric oxide measurements by means of laser-induced fluorescence in a heavy-duty diesel engine*, K. Verbiezen, A.P. van Vliet, R.J.H. Klein-Douwel, L.C. Ganippa, H.J.T. Bougie, W.L. Meerts, N.J. Dam, and J.J. ter Meulen, Proceedings of the European Combustion Meeting 2005, Louvain-la-Neuve, Belgium (2005).
- *Absorption of NO laser-induced fluorescence by hot O₂ and CO₂*, K. Verbiezen, A.P. van Vliet, W.L. Meerts, N.J. Dam, and J.J. ter Meulen, Combustion and Flame 144, 638–641 (2006).
- *Correction for attenuation effects on laser-induced fluorescence measurements of nitric oxide in a heavy-duty diesel engine*, K. Verbiezen, R.J.H. Klein-Douwel, A.J. Donkerbroek, A.P. van Vliet, W.L. Meerts, N.J. Dam, and J.J. ter Meulen, Applied Physics B 83, 155–166 (2006).
- *Quantitative laser-induced fluorescence measurements of nitric oxide in a heavy-duty diesel engine*, K. Verbiezen, R.J.H. Klein-Douwel, A.P. van Vliet, W.L. Meerts, N.J. Dam, and J.J. ter Meulen, Proceedings of the Combustion Institute 31 (2006).

- *Diesel combustion: in-cylinder NO concentrations in relation to injection timing*, K. Verbiezen, A.J. Donkerbroek, R.J.H. Klein-Douwel, A.P. van Vliet, P.J.M. Frijters, X.L.J. Seijkens, R.S.G. Baert, W.L. Meerts, N.J. Dam, and J.J. ter Meulen, submitted to Combustion and Flame (2006).